

**Pulsed Laser Deposition of ZnO Thin Films for Electronic and Optical Device
Applications**

by

Fatema Rezwana Chowdhury

A thesis submitted in partial fulfillment of the requirements for the degree of

Master of Science

in

Photonics and Plasma

Department of Electrical and Computer Engineering

University of Alberta

© Fatema Rezwana Chowdhury, 2017

Abstract

Zinc Oxide (ZnO) is a promising wide band gap semiconductor with exceptional electrical and optical properties. Thin film ZnO can be used for a wide variety of electronic and optoelectronic device applications. The first step on the way to achieving good quality devices is to grow optimum quality thin films on desired substrates. Pulsed laser deposition (PLD) is a popular technique to deposit complex structures and oxide semiconductors. The growth parameters of PLD have significant effects on thin film properties and qualities. The first part of this work presents the optimization of Zinc oxide (ZnO) film properties for thin film transistor (TFT) application. Thin films of ZnO were deposited by PLD under a variety of growth conditions. The oxygen pressure, laser fluence, substrate temperature, and annealing conditions were varied to optimize the growth conditions for a higher mobility and lower defect density thin films according to the device demand. Room temperature ZnO growths followed by air and oxygen annealing showed improvement in the (002) phase formation with a carrier concentration in the order of 10^{17} - 10^{18} cm^{-3} along with low mobility in the range of $0.01 - 0.1 \text{ cm}^2\text{V}^{-1}\text{s}^{-1}$, while relatively low temperature growth ($250 \text{ }^\circ\text{C}$) of ZnO achieved a Hall mobility of $8 \text{ cm}^2\text{V}^{-1}\text{s}^{-1}$ and a carrier concentration of $5 \times 10^{14} \text{ cm}^{-3}$. The low carrier concentration indicates that the number of defects have been reduced nearly by three orders of magnitude as compared to the room temperature annealed growths. Also, it was observed clearly that higher mobility had a strong correlation with the (002) crystal orientation. Higher mobility ($18 \text{ cm}^2\text{V}^{-1}\text{s}^{-1}$) was achieved with a $250 \text{ }^\circ\text{C}$ growth followed by in-situ oxygen annealing for an hour, however, the defect concentrations also went up to the order of 10^{19} cm^{-3} . Higher temperature studies on different substrates like sapphire and SiO_2/Si were also done with other optimized parameters. Temperatures higher than $250 \text{ }^\circ\text{C}$ increased other phase formations like (103). At $700 \text{ }^\circ\text{C}$ films were highly (103) oriented with hexagonal ZnO grain structures.

The optical properties of ZnO have been studied for more than 60 years now but there are still unsolved puzzles about the origins and decay natures of different defect emissions which contribute to the wide visible band of the PL spectrum of ZnO. This visible emission and near band edge UV emission are also an indicator about the films radiative efficiency and crystal

quality. In the second part of this project time integrated and time resolved photo luminescence measurements were done on a single crystal ZnO wafer and PLD thin film ZnO samples to understand the radiative nature of the thin films with respect to excitation parameters.

The time resolved measurements were instrumentation limited for the thin film samples but for the single crystal the fast and slow components were 140 ± 10 ps and 340 ± 20 ps which is in agreement with literature. The fast decay time for thin film samples may be due to more non radiative traps present near the surface.

The radiative efficiency in the visible range decreased with increased excitation density for continuous wave, ns and fs excitation. On the other hand, the UV emission efficiency increased with higher excitation density. For all the samples it was observed that excitation density close to their electrically measured defect density saturates the visible defect emission and enhances the near band edge UV emission. This may be due to the change in exciton formation rate and capture rate by the defect sites which are saturated with increased excitation density.

Dedicated to
Ahsan

Acknowledgements

First, I wish to thank my advisor, Prof. Ying Yin Tsui for giving me the opportunity to work in this project. Moreover, his diverse research projects in optical materials and laser application helped me gather extensive knowledge in this area. His standards of excellence and his love of science are truly inspiring. In the span of these few years, he has helped me grow as a self-sufficient, confident, and detail-oriented professional.

I would like to convey my sincere thanks to my co-supervisor Prof. Manisha Gupta. Her guidance and advice helped me from the very beginning to the extreme end of this journey. She has not only been a remarkable supervisor to me but also a wonderful role model. Her extensive knowledge in experimental design and instrumentation has always been impressive.

Excellent technical support from Blair Harwood and Herbert has made the path smoother.

Support and thoughtful discussions from Yogesh, Zhijian, Shyama, Archana, Hal, Debby, Raj, Tim, Mei and Mianzhen are gratefully acknowledged.

I would like to acknowledge funding from the Natural Science and Engineering Research Council of Canada, Faculty of Graduate Teaching and Research, University of Alberta and Canadian Institute for Photonic Innovations.

Finally, I would like to thank my amazing family for their best support. My loving and caring husband Ahsan Alam, my support system, his patience and endless support encouraged me to reach my destination successfully. I would never been able to do this without the endless blessings and mental strength from my loving mother Dilruba Hussain Chowdhury. Thanks to Arshad and Areeba for providing non-stop entertainments outside the lab during this time.

Table of Contents

1. Introduction ...	1
1.1 Motivation	1
1.2 Overview of ZnO	2
1.2.1 Crystal structure and lattice parameters	3
1.2.2 Electrical properties of ZnO	3
1.2.3 Optical properties of ZnO	4
1.3 Applications	5
1.3.1 Thin film transistor (TFT) application	5
1.3.2 UV source application	6
1.4 Overview of Pulsed Laser Deposition(PLD)	6
1.5 Overview of Thesis	8
2. Theoretical Background	10
2.1 Introduction	10
2.2 Pulsed Laser Deposition	10
2.2.1 Laser solid interaction	11
2.2.2 Crystal growth modes in PLD	13
2.3 Photo Luminescence	14
2.3.1 Luminescence from Solids after light absorption	15
2.3.2 Free Carrier generation	16
3. Experimental set up	18
3.1 Pulsed Laser Deposition system	18
3.1.1 Vacuum System	18
3.1.2 Deposition system	20
3.1.3 Laser and Optics	22

3.2	Calibrated Photodiode for Laser Energy Monitoring	24
3.3	Plasma Plume Monitoring with Langmuir Probe	25
3.4	Growth characterization techniques	27
3.4.1	X-Ray Diffraction	27
3.4.2	Scanning Electron Microscopy	28
3.4.3	Atomic Force microscopy	29
3.4.4	Film Thickness Measurement	29
3.4.5	Photo Luminescence Measurement Setup	30
4.	Growth Parameter Optimization For ZnO thin Films	34
4.1	Calculating ion velocity, energy and the effect of laser fluence on them using Langmuir Probe.....	34
4.2	Substrate Heater calibration for PLD growths	38
4.3	Growth Parameters Optimization for TFT Application	39
4.3.1	Structural and morphological study	41
4.3.2	Electrical Measurements	46
4.4	Temperature Dependency	47
4.5	In situ cooling in oxygen atmosphere	52
4.6	Summary	52
5.	Photoluminescence of ZnO	54
5.1	Time Integrated Photoluminescence (PL)	55
5.1.1	Photoluminescence from CW He-Cd Laser Excitation	55
5.1.2	Photoluminescence from ns Pulsed Laser Excitation	62
5.1.3	Photoluminescence from fs Pulsed Laser Excitation	67
5.2	Time-resolved Photoluminescence (TRPL) Measurement of ZnO Samples	69
5.3	Influence of Photoexcitation Density on PL spectrum of ZnO	72
5.4	Summary	76

List of Tables

Table 4.1. Fluence growth rate, ion density, ion velocity, and crystal orientation of PLD grown samples	37
Table 4.2. PLD growth conditions of the different ZnO 50 ± 10 nm thick samples along with the post-growth annealing conditions [48]	40
Table 4.3. Summary table for temperature dependence study	48
Table 4.4. Comparison of grain sizes from SEM and XRD	51
Table 5.1. Comparison of possible transition and FWHM of the major peaks	57
Table 5.2. TRPL measurement Data from ZnO single crystal and PLD deposited thin film	70
Table 5.3. Approximated photo carrier concentration and measured intrinsic carrier concentrations [9, 46] of different samples	74
Table 6.1. The crystal grain size and surface roughness measurements of GaAs thin films from AFM for different growth temperatures	83
Table 5.1.2. Calculated photo carrier concentration and measured intrinsic carrier concentrations of different samples	62
Table B1. Error calculation for PL measurements of ZnO	98

List of Figures

Fig 1.2.1. (a) The hexagonal wurtzite structure, (b) The zinc blend structure and (c) The rock salt structure of ZnO. [7]	3
Fig. 1.2.2. Schematic band diagram of some defect level emission (DLE) in ZnO [12].....	4
Fig. 2.2.1. Schematic Diagram of a typical PLD system.....	11
Fig. 2.2.2. Crystal growth modes (θ is the time of monolayer coverage) [35].....	13
Fig.2.3.1. Schematic of PL excitation	16
Fig. 3.1.1. Vacuum system for PLD.....	19
Fig. 3.1.2. Experimental set up for PLD.....	20
Fig. 3.1.3. PLD heater manufactured by Neocera Inc. [43].....	21
Fig. 3.1.4. Schematic diagram of the Clamp for substrate mounting on the heater.....	22
Fig. 3.1.5. (a) CCD measurement set up for the beam spot measurement and (b) a representative contour plot of the intensity profile.....	23
Fig. 3.2.1. Photodiode calibration and laser energy measurement set up.....	24
Fig 3.3.1 A simple Langmuir probe.....	25
Fig 3.3.2. (a) Experimental set up and (b) Bias box CKT diagram for the Langmuir probe experiment.....	26
Fig. 3.4.1. A schematic diagram of XRD measurement set up.....	28
Fig. 3.4.2 PL measurement set up for Time integrated fs measurement.....	31
Fig 3.4.3. Schematic diagram of TRPL setup with fiducial monitor. M2 and M2 are dielectric mirrors coated with high reflectivity coating at 266nm. BS is beam splitter with 10% reflection	

and 90% transmission. F1, F2 and F3 are lenses of 2.5cm diameter, whose focal distances are 10cm, 5cm and 10cm respectively.....	32
Fig.4.1.1. The ion probe signal detected by the Langmuir probe for ZnO target.....	35
Fig. 4.1.2. The ion probe signals at different lens positions.....	36
Fig 4.2.1. A bar graph to compare the Eurotherm temperature controller with the actual substrate temperature.....	38
Fig. 4.3.1. Glancing angle X-ray diffraction (XRD) plots for different PLD samples, sample 3-A was grown at room temperature, sample 3-B was grown at room temperature and post growth oxygen annealed and sample 8-A was grown at 250° C substrate temperature.....	41
Fig 4.3.2. X-ray diffraction (XRD) plot for hydrothermally grown ZnO single crystal wafer by MTI.....	43
Fig. 4.3.3. SEM images at 50,000x magnification with the scale bar of 100 nm. (a) SEM of unannealed 100 mtorr, 2.75 J/cm ² , room temperature growth of ZnO, indicating small grain size of 3-4 nm. (b) and (c) SEM after annealing the sample in O ₂ and air, it can be observed that the grains have grown, but there are spaces between the grains. (d) Unannealed grown at 100 mtorr, 2.75 J/cm ² , 250 °C indicating larger grains and very dense film with no cracks.....	44
Fig. 4.3.4. AFM image of the un annealed film grown at 250°C on SiO ₂ /Si.....	45
Fig. 4.3.5. Calculated doping concentration of 250 °C ZnO samples using C-V measurements..	46
Fig. 4.4.1. XRD plot for different temperature growths on Sapphire substrate.....	47
Fig. 4.4.2. XRD plot for different temperature growths on Sapphire and SiO ₂ /Si.....	49
Fig. 4.4.3. SEM images of ZnO thin film on (a) SiO ₂ /Si at 250 °C, (b) Sapphire at 250 °C (c) SiO ₂ /Si at 700 °C and (d) sapphire at 700 °C.....	50
Fig. 5.1.1. CW laser excited PL spectrum of ZnO single crystal and PLD thin films.....	55
Fig. 5.1.2. CW laser excited PL spectrum of (a) ZnO single crystal, (b) PLD 250 °C thin film and (c) Room temperature PLD thin film with Gaussian fit for the PL peaks.....	56

Fig. 5.1.3. Energy level diagram for all possible transitions for CW measurements of the three samples.....	59
Fig. 5.1.4. Nano-second pulse laser excited PL spectrum of ZnO single crystal and PLD thin film.....	63
Fig. 5.1.5. Nano-second pulse laser excited PL spectrum of (a) ZnO single crystal, (b) PLD room temperature thin film, and (c) PLD 250 °C substrate temperature thin film.....	64
Fig. 5.1.6. Energy level diagram for all possible transitions for ns measurements of the three samples.....	65
Fig. 5.1.7. Nano-second pulse laser excited PL spectrum of ZnO PLD target.....	66
Fig. 5.1.8 Time integrated PL spectra of single crystal ZnO wafer and PLD thin film sample with femtosecond pulsed laser excitation.....	67
Fig. 5.1.9. Time integrated PL spectra of single crystal ZnO wafer and PLD thin film sample with femtosecond pulsed laser excitation with Gaussian fitted peaks.....	68
Fig. 5.2.1. Temporal response for the PL spectrums of ZnO single crystal and PLD deposited thin film on SiO ₂ substrate.....	70
Fig. 5.2.2. Temporal response for the PL spectrums of ZnO single crystal and PLD deposited thin film on SiO ₂ substrate with fiducial monitor.....	71
Figure 6.3.1. XRD spectra of GaAs thin films grown at (a) room temperature, (b) 285 °C, (c) 500 °C, and (d) 600 °C.....	81
Figure 6.3.2. XRD spectrum shows that at higher temperature ($TS \geq 500$ °C), the relative intensity of (111) peak increased significantly compared to other peaks.....	82
Figure 6.3.3. AFM images of GaAs thin films.....	82

Figure 6.3.4. (a) SEM and (b) AFM images of GaAs thin films on Si at TS = 500 °C.....	84
Figure 6.3.5. Change in Grain size with growth temperature.....	84
Fig. 7.2.1. Raman spectra of ZnO single crystal wafer.....	92
Fig. A1. Photoluminescence spectrum of ZnO thin film on SiO ₂ /Si substrate before background subtraction.....	94
Fig. A2. Back ground light contribution for 10 second integration time.....	95
Fig. A3. Time integrated PL emission from ZnO thin film deposited by PLD after background subtraction.....	96
Fig. B1. UV Photoluminescence from ZnO single crystal wafer with ns excitation.....	97
Fig. C1. Time resolved PL measurement of ZnO for carrier life time estimation.....	99
Fig. D1. AFM image of 2x2 μm area of the DLC film deposited on (a) Si substrate with an rms roughness of 0.6 nm (b) DLC film grown on soap film (rms roughness 8-12 nm) and lifted-off on to a metal plate demonstrating an rms roughness of 9 nm [98].....	101
Fig. D2. Plot for ion current versus time for the (a) fs Ti:Sapphire laser and (b) ns KrF laser, to determine the ablation threshold for poly-Si target, measured at several different laser energies [99].....	102
Fig. D3. SEM of Si nano dots on GaAs substrate using the ns KrF laser at 5000x showing a large size distribution from 100 nm to 3μm droplets and 100000x magnification showing two 100 nm nano dots grown by PLD at 32 J.cm ⁻² fluence [100].....	103
Fig. D4. SEM image of Si Nano dots grown on GaAs substrate using the fs Ti:Sapphire for PLD at 1.5 J.cm ⁻² fluence. Fast growth rate with lots of cluster formations were observed [100]....	104
Fig. D5. SEM of patterned Si nano dots at 10,000x and 50,000x magnification on GaAs substrate using EBL mask using ns KrF laser at 5 J.cm ⁻² [100].....	104

Chapter 1

Introduction

1.1. Motivation

Zinc Oxide (ZnO) is a promising wide band gap semiconductor with exceptional electrical and optical properties. Thin film ZnO can be used for a wide variety of electronic and optoelectronic device applications. The first step on the way to achieving good quality devices is to grow optimum quality thin films on desired substrates. There are many different techniques for thin film fabrication. Among them, Pulsed Laser Deposition (PLD) is one of the most popular methods for the deposition of oxide semiconductors like ZnO for many advantages. High mobility c-axis oriented epitaxial ZnO thin films are reported using multistep PLD on sapphire substrate [1]. Thin film ZnO on SiO₂/Si substrate is the key for many electronic applications. In order to achieve successful device quality thin films of ZnO on SiO₂/Si substrate with higher mobility and lower carrier concentration (in the order of 10¹⁵ /cm³) the growth parameters of PLD need to be optimized. Oxygen partial pressure, laser fluence, substrate temperature all these important parameters have their effects on the deposited films properties. Using various characterization techniques, the variation of these properties can be measured to establish the optimized growth parameters. In this thesis, PLD growth parameters were varied to optimize the properties of ZnO thin films important for electronic and optical device applications on SiO₂/Si substrate. The popular substrate choice for ZnO thin films in literature is C-axis oriented Sapphire. Effect of substrate (SiO₂/Si and sapphire) with same growth parameters will provide important information for different substrate choice.

Photoluminescence (PL) of ZnO has been investigated for last two decades. A typical ZnO thin film PL spectrum consists of a near band edge UV emission accompanied by a visible emission which is contributed from various defect states present in between the conduction and valence

bands [2]. These UV and visible emission efficiencies and life times can contribute to monitoring thin film quality. As PL measurements are non-destructive and does not need any sample preparation, time integrated and time resolved PL measurements can be used to obtain important information about different defect states, carrier lifetime etc.

Besides focusing on the optimization of the PLD growth parameters, this thesis also includes a detailed discussion on the effects of different excitation parameters of PL measurements on the PL emission of ZnO thin films.

1.2. Overview of Zinc Oxide

Zinc oxide has a variety of applications in our everyday life. It is used as a white pigment in paint, a food additive for its zinc content, and as an additive in cosmetics, sunscreens, and diaper rash ointment. The wide range of applications reflects the fact that ZnO is cost effective and safe for both environment and humans. All of these applications typically use polycrystalline powdered ZnO.

Early investigations on the optical and electrical properties of ZnO were performed on ZnO whiskers and platelets [3, 4]. These samples were precursors of modern day thin films and nanowire samples [2, 5, 6]. Additionally, bulk single crystal ZnO wafers were fabricated using hydrothermal method [7]. Several groups of researchers have investigated the optical, electrical and structural properties of thin film ZnO grown on different substrate materials with different growth techniques. The most widely adopted techniques are molecular beam epitaxy (MBE), RF sputtering, pulsed laser deposition (PLD), and solution based deposition techniques like sol-gel [8 - 11]. Recently, atomic layer deposition (ALD) is also becoming popular for depositing ZnO on different substrates for various applications [12]. The capability of thin film depositions under a highly reactive gas ambient over a wide range of pressure makes PLD an attractive method for fabricating complex oxides like ZnO. Thin films of ZnO deposited using all of these aforementioned methods can be used to fabricate optoelectronic and electronic devices. The wide direct band gap (~ 3.4 eV) and large exciton binding energy (60 meV) [13, 14] of ZnO makes it a very promising candidate for room temperature UV source applications. Also, the high electron mobility and compatibility with the various processing steps make it an attractive material for the active channel layer of thin film transistors (TFTs) [10].

1.2.1. Crystal Structure and Lattice Parameters

ZnO crystallizes preferentially in the stable hexagonal wurtzite structure at room temperature under normal atmospheric pressure as shown in Fig. 1.2.1. It has lattice parameters, $a = 0.3296$ nm and $c = 0.520$ nm [11]. In this structure each oxygen ion is surrounded tetrahedrally by four zinc ions, and vice versa, stacked alternatively along the c-axis.

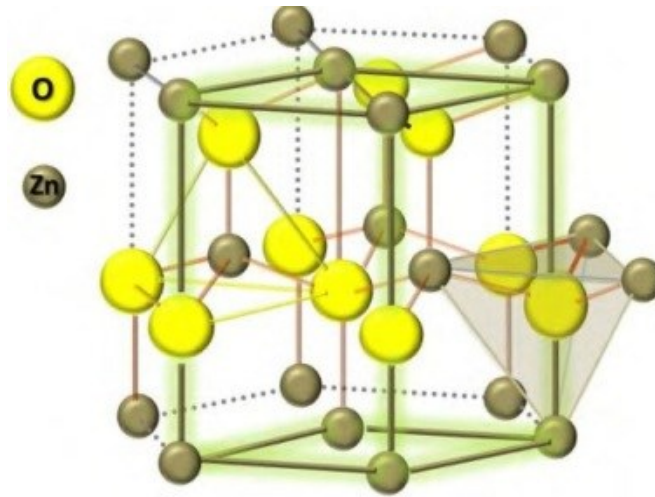


Fig 1.2.1. The hexagonal wurtzite structure of ZnO [7].

1.2.2. Electrical Properties of ZnO

Unintentionally doped or as grown ZnO is a transparent (for visible wavelengths) conducting semiconductor with n-type conductivity at room temperature. Unavoidable presence of electrically active native defects and impurities are the main contributors for this n-type conductivity [13]. Thus the background carrier concentration depends on the quality of the ZnO material. This value is typically in the range of $\sim 10^{15}$ - 10^{16} cm^{-3} [14]. Although n-type ZnO can be achieved with a carrier concentration as high as 10^{21} cm^{-3} , p-type doping is still the biggest technological challenge for this material.

1.2.3. Optical Properties of ZnO

The optical properties of a semiconductor can be greatly influenced by the extrinsic and intrinsic defects in the crystal structure. Investigation of the optical properties of ZnO has a long history that started in the 1960s [15]. The efficient radiative recombinations are the most interesting optical properties of ZnO. The optical properties of ZnO, bulk and nanostructures, have been investigated extensively by photo luminescence (PL) techniques at low and room temperatures.

Typically PL emissions from ZnO thin films have a near band edge UV emission and also some visible emissions (for example green and orange band) [5]. According to existing literature [10, 15, 16], the visible bands are emitted from different defects due to vacancies and interstitials in ZnO. Controlling the quantity and nature of these defects is a prerequisite to achieving a good control over the electrical and optical properties of ZnO.

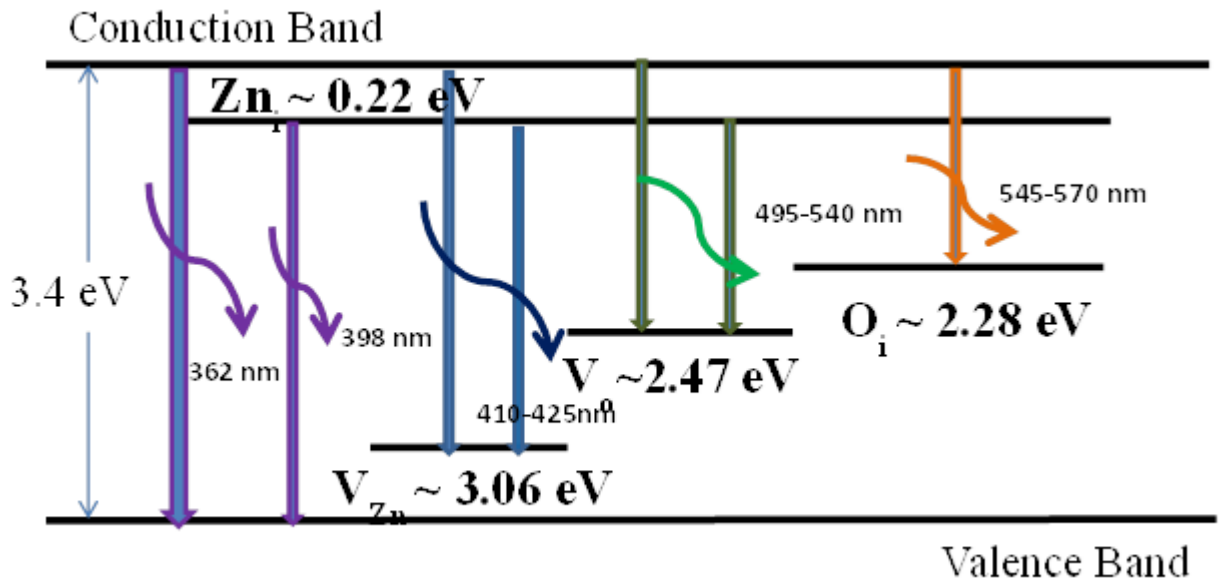


Fig. 1.2.2. Schematic band diagram of some defect level emissions (DLE) in ZnO [12].

These various defects can be introduced during the growth process or by post-growth treatments such as annealing. Thus growth and post-growth processing parameters have a great impact on the material properties. It is very important to understand the origin and behavior of these defects in ZnO. However, the origins of these defects are still under investigation. Researchers have suggested different origins for these defects [14]. According to the calculation using linear

muffin tin orbital theory, Fig. 1.2.2 shows the radiative transitions of the charge carriers from different defect related states [15].

1.3. Applications

1.3.1. Thin Film Transistor (TFT) Application

A thin film transistor (TFT) is a field effect transistor (FET) where a semiconductor thin film (deposited on a suitable substrate) is used as a channel material. High current on/off ratio and good electron mobility are the two key electrical parameters required for reasonable TFT performance. Also it has a high breakdown voltage which makes it more promising for the TFT application. In existing literature, ZnO TFTs with field effect mobilities in the range of 0.5 to 20 $\text{cm}^2\text{V}^{-1}\text{s}^{-1}$ and current on/off ratio ($I_{\text{on}}/I_{\text{off}}$) greater than 10^5 have been reported [9]. In addition to this, ZnO is transparent in the visible region of the electromagnetic spectrum. All these features make ZnO based devices suitable for extremely low cost power inverters and transparent electronics applications.

Electrical properties of the TFTs are strongly dependent on the quality of the semiconductor thin film. Optimum quality thin film is required for higher mobility and limited carrier concentrations. The efficiency with which charge carriers move from source to drain through the TFT channel is known as mobility. When an electric field E is applied across a material, the electron drift velocity v_d due to that electric field is given by,

$$v_d = \mu E \quad (1.1)$$

Where, μ is the mobility. The relationship between mobility and electrical conductivity can be given as follows

$$\sigma = ne\mu \quad (1.2)$$

Where n is the carrier concentration, e is the single electron charge and σ is the electrical conductivity. Thin films with poor crystal quality and large defect density have reduced mobility as the defects act as scattering sources for the electrons. Hall mobility measurements can provide information about the mobility of the charge carriers and also the carrier concentrations which is responsible for the background doping.

Also other electrical measurements like C-V measurements can be performed by fabricating Schottky contacts on the samples to obtain the carrier concentration of the sample. This method needs an additional step for sample processing but it can be used to compare the Hall measurements.

1.3.2. UV Source Application

The direct and wide band gap of ZnO makes it a suitable candidate for the UV based optical device application. Nominally undoped ZnO is inherently n-type but stable p-type ZnO is the main obstacle for the p-n homojunction ZnO based light emitting diodes (LEDs). Although there are some research groups who have reported ZnO based homojunction LEDs, the reported electroluminescence values were extremely small [17-20]. This problem encouraged the research community to develop heterojunction LEDs. ZnO heterojunctions with other p-type materials such as Si, SiC, GaN, AlGaN, Cu₂O, GaAs, diamond, ZnTe, CdTe, and NiO or p-type organic materials [21, 22] can be used to get the full advantage of the exceptional optical properties of ZnO.

Stimulated emission from ZnO thin films at room temperature was first reported by Bagnall *et al.* [23]. These ZnO thin films were fabricated by molecular beam epitaxy (MBE). Lasing in ZnO nanowires thin films were first observed by Hung *et al.* [24]. These nanowires grown by vapour transport and condensation process had diameters in the range of 20-150 nm and had lengths of several mm. Room temperature UV emission was observed under optical excitation from these nanowires films [25].

1.4. Pulsed Laser deposition: An Overview

In the spring of 1987, the American Physical Society of New York had a special session on high temperature superconductor (HTS) materials. Catching the breath of the scientific community, these meetings introduced a completely new horizon in the field of thin film fabrication. Soon after these meetings, a scientific group (Venkatesan *et al.*) used laser to evaporate a sample of stoichiometric YBa₂Cu₃O_{7-x} (YBCO) and deposit it as a film [26]. It turned out that the process was able to evaporate the target and create a new film but the composition of the new film was different from the target since different elements evaporated at different rates. The solution was to use an excimer laser to create non-equilibrium evaporation since it penetrates only a thin

surface of the material preserving the composition. Thus emerged a new technique that uses flashes of laser to produce an atomic spray and eventually deposits an HTS thin film. Continued research on deposition techniques has enabled the fabrication of films as thin as 1.2 nm over a period of just ten years [26]. Today PLD is one of the most sophisticated and widely accepted thin film fabrication processes.

PLD has become a widely used technique for the deposition a variety of thin films. It is used to fabricate numerous materials [27] such as HT superconductors, ferroelectrics, nitrides, metals, oxides [28], and even porous thin films [29, 30]. The major reason for the wide acceptance of PLD over other deposition methods is the array of advantages it offers. The key advantages are simplicity and flexibility in design, instantaneous growth rate, enhanced crystallinity and congruent transfer. Among the disadvantages of PLD are (a) inhomogeneity of deposited thin film, (b) droplets and particulates deposited on the thin film, and (c) roughness of the target. Considerable amount of work has been done in overcoming these problems. The inhomogeneity problem can be solved by rotating the substrate [31]. Controlling the laser fluence can lower the droplet formation and target roughness problems [27].

In pulsed laser deposition of thin films, maximum deposition rate is much higher than other techniques like thermal evaporation or sputtering. The ionic content in the laser deposition plume is very high and it rises if the incident laser fluence is increased. This higher ionic content helps the crystalline growths and also helps to keep the substrate temperature low for epitaxial growth. For example, epitaxial Germanium films can be grown on silicon substrate using PLD at a substrate temperature 300 °C. Vacuum evaporated thin films at this temperature are polycrystalline. It is believed that the high energy ions increase the crystal nucleation sites on the Silicon substrates [32].

Unlike other thermal evaporation methods PLD is more flexible in terms of targets. A small target of the desired compound is enough for deposition where other methods need each element of the compound separately as target. The source of heat in the vacuum is very small in PLD because power is efficiently focused on the target and heating is localized. This makes the out gassing minimum and thus the load on the vacuum pump is low. It is also suitable for growing at background gas pressures and lower vacuum compared to Molecular Beam Epitaxy (MBE). Also

in PLD, material is taken out from the target with a $\cos^n\theta$ distribution where θ is the angle to the target normal and n is a power higher than one which makes it a more directional process.

Until now, researchers are trying to overcome the main disadvantages of PLD like inhomogeneity, surface roughness and debris and formations. The inhomogeneity problem can be overcome by scanning of substrate [31] or by scanning of laser beam [33]. In order to produce a film with uniform properties over large areas, the laser can be incident on the target after being reflected by an anti-reflection coated mirror where the mirror is moved back and forth using a programmable linear actuator [33].

Lower fluence can lower the droplets or debris [33] for PLD deposited thin films. Guiding the plasma created by laser matter interaction during PLD process using a magnet (MGPLD) can reduce the debris even more [34]. This technique was developed previously by Y. Y. Tsui *et. al.* in our lab. A curved magnetic field is used to guide the plasma but not the neutral species to the substrate to deposit the films. In a typical PLD, growth film is grown from neutrals, ions and droplets.

Er doped chalcogenide glass thin films were deposited [35] for integrated optics application in our lab by PLD. Y.Y. Tsui *et. al.* deposited films very close to the target composition which was a challenge for this material. These films also had a nice luminescence at 1542 nm.

1.5. Overview of Thesis

ZnO is a wide band gap semiconductor which is attractive for optical, optoelectronic and electronic device applications. Successful development of devices based on this material needs knowledge about the dependence of thin film ZnO's structural, optical and electrical properties on the growth parameters. To monitor the quality of the thin films, optical techniques like photoluminescence measurement can be a non-destructive and simple method. Correlation of the excitation parameters of the PL with the emission spectrum can contribute to evaluating the quality of the thin film for different applications. The goal of this dissertation is to optimize and understand the factors that influence the radiative emissions (both UV and visible) and carrier mobility in PLD deposited ZnO thin films so that the material growth techniques can be tuned to control these properties on demand. The contents of this thesis are organized as follows:

Chapter one outlines the description about the material and its properties used throughout the thesis and summarizes a brief history about the fabrication process used in this work.

Chapter two briefly discusses the theory of PLD and photoluminescence.

Chapter three presents the experimental details about the growth and characterization techniques of the prepared samples.

Chapter four describes the optimization of ZnO thin film growth parameters using PLD. The substrate choices were SiO₂/Si and Sapphire.

Chapter five describes the time integrated and time resolved photoluminescence of ZnO thin films and a bulk ZnO wafer. This chapter also outlines the excitation parameter dependence behaviour of PL spectrum.

Chapter six presents the substrate temperature study on GaAs thin films deposited by PLD, the substrate choice was Silicon.

Chapter seven concludes the works and results from this work. Additionally future experiments and extension of this work are also discussed in this chapter.

Chapter 2

Theoretical Background

2.1. Introduction

One of the important goals of this thesis was using lasers for both fabrication and optical characterization for quality control of ZnO thin film samples. In order to achieve this, pulsed laser deposition (PLD) was used to fabricate the thin film samples on different substrates and photoluminescence (PL) measurements were used to characterize the samples using their optical properties. The background theories for PLD and PL are discussed in this chapter.

2.2. Pulsed Laser Deposition

The PLD technique is an attractive method for depositing many materials including compound structures [26, 28]. In PLD, high energy ions are produced by laser-target interaction which leads to many advantages commonly found in ion assisted deposition [26]. The presence of high energy ions in PLD is reported to help achieving epitaxial growth at relatively lower substrate temperature [33]. The relatively low substrate temperature is particularly required for deposition on substrate materials which have a different thermal expansion from the target material.

In PLD (Fig. 2.2.1), a target material is ablated using a short pulsed laser which creates plasma of the target material and the plasma travels towards the substrate to be deposited as thin films. The whole process takes place under vacuum or in presence of a background gas. Generally a pulsed (UV, visible, or NIR) laser fires a short burst (~10 ns) of energy at a repetition rate (10 Hz or more). When the laser pulse interacts with the target material some portion of the energy is absorbed by the material and causes the materials to be ablated in a conical shape of plasma cloud propagates outward from the target surface toward the substrate. The plasma cloud typically consists of ions, electrons, neutral atoms/molecules and clusters.

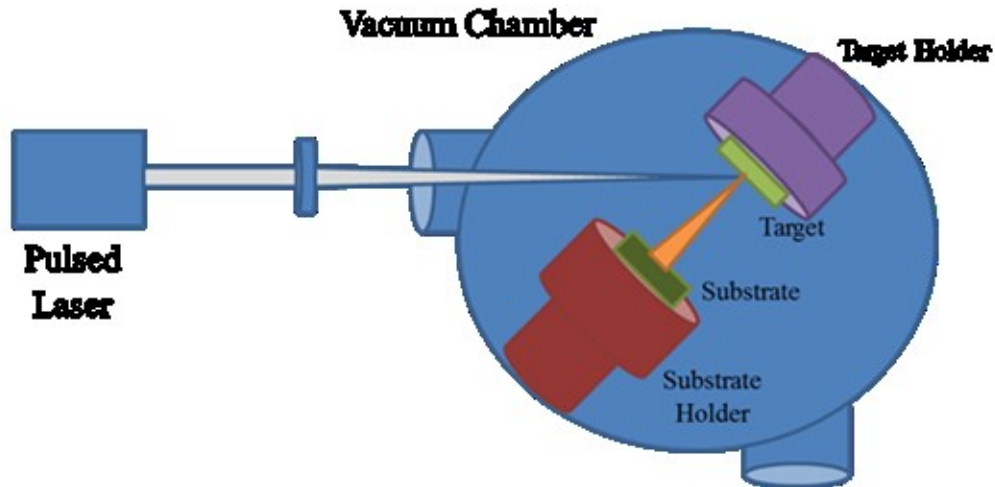


Fig. 2.2.1. Schematic Diagram of a typical PLD system.

2.2.1. Laser Solid Interaction

When a laser pulse is incident on a target material some of the laser energy is reflected and some is absorbed. The ablation of the target materials depends heavily on the reflectivity of the material at the laser wavelength. Ultra-violet (UV) lights have the lowest reflectivity for the widest range of the materials which is the reason why UV lasers are the popular choices for PLD.

The ablation process takes place in three steps. In Step 1, the laser interacts with the target and transfers energy into atoms and electrons. In metals the free electrons absorb photons and gain higher energy, in semiconductors the valence band electrons absorb energy and jump to the empty conduction band if the laser energy is higher than the band gap energy, and in dielectrics where the band gaps are very high (larger than the laser energy) multiple photons are needed to be absorbed to transfer an electron from the valence band to the conduction band.

When a laser pulse hits the solid surface of a target, the energy of the pulsed laser which is absorbed by the material penetrates a distance called the skin depth given by [33],

$$\sigma = \sqrt{\frac{2}{\omega\mu\sigma}} \quad (2.1)$$

where, ω is the angular frequency, μ is the magnetic permeability and σ is the conductivity. When these electrons go back to equilibrium after a few ps, heat is produced. The heat penetration depth is the region of the target material which is below the skin depth, this region is also heated subsequently and this distance can be given by [36],

$$L_{th} = \sqrt{\frac{2k\tau_p}{\rho c}} \quad (2.2)$$

where, k is the thermal conductivity, τ_p is the pulse length of the laser, ρ is the material's mass density and c is the speed of light.

Vaporization of a material requires much more energy than to melt it. Evaporation starts to take place when the energy absorbed into the vaporized layer is more than the latent heat of evaporation. This ablation depth is given by [36],

$$\Delta z_v \approx \frac{A(F_L - F_{th})}{\rho L_v} \quad (2.3)$$

where, A is the surface absorbance of the target, F_L is the laser fluence, L_v is the latent heat per unit mass, and F_{th} is the laser fluence threshold which represents the minimum energy above which the appreciable vaporization occurs [36].

Step two is when the materials from the heated surface start to eject and they will continue to absorb energy from the incident laser. The ejections of particles from the target surface create the plasma plume.

Step three is the adiabatic expansion of the plume at a constant speed (in vacuum) or interaction with background gases will reduce the speed. After a few microseconds the plume will reach the substrate.

2.2.2. Crystal Growth Modes in PLD

There are five different modes of crystal growth in PLD as illustrated in Fig. 2.2.2 [36]. The first method is the layer by layer or the Frank-Van der Merwe growth mode [36]. In this mode a stable monolayer forms on the surface of the substrate before another layer starts to begin. The result of this kind of growth is a very smooth film.

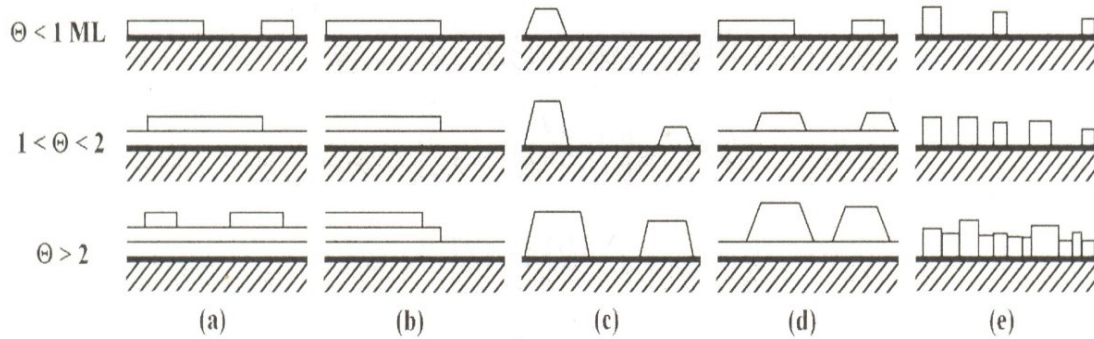


Fig. 2.2.2. Crystal growth modes (θ is the time of monolayer coverage) [35].

The second growth type is called the step flow growth mode. This growth mode is quite similar with the layer by layer growth mode the only difference here is the layers here grows as a series of steps. That is why the film has a terraced effect.

The third mode is called the island mode or the Volmer-Weber growth mode. This growth mode is the result of the higher attraction of the adatoms to the nucleated growth sites than the surface. This produces the island like structure to form on the substrate.

The fourth mode is the combination of the first and third growth pattern. In this case on top of the layer by layer growth islands are also formed. This mode is commonly known as the Stranski-Krastanov (S-K) mode. This mode of film formation was present in a variety of systems [7]. For example Ag deposited on W, Ag deposited on Si [33] and also Ge deposited on Si. Here the first few layers (typically 1-5 monolayers) deposited as monolayers and then three dimensional clusters nucleate on top of these mono layers. Due to increased mismatched lattice

spacing with increase in layer thickness causes the increment of stress, three dimensional cluster nuclei form over the monolayers [33].

In the fifth growth mode the films have a columnar growth mode.

2.3. Photo Luminescence

When a light of sufficient energy is incident on a semiconductor, absorption of photons causes electronic excitations. In time, these excitations relax and the charge carriers return to the ground state. If this relaxation process is radiative, the emitted light is called PL. Electronic levels can be determined by the transition energies of a PL spectrum [37]. Moreover, pulsed excitation with a very short pulse laser can be used to obtain information about different decay behaviour of different PL components. The PL method is simple and non-destructive. As the measurement does not need any electrical excitation, sample preparation is minimal. Also, PL measurements do not require to be performed under high vacuum conditions unlike many other surface characterization techniques. Hence, it can also be implemented in-situ to study surface properties of semiconductors grown in relatively high pressure like ZnO.

In this thesis we performed PL measurements of different ZnO samples. Typically PL emissions from ZnO thin films have a near band edge UV emission and also some visible emissions (for example green and orange band) [5]. According to existing literature [5, 37, 38], the visible bands are emitted from different defects due to vacancies and interstitials in ZnO.

2.3.1. Luminescence from Solids after Light Absorption

Spontaneous emission of photons occurs when electrons in excited states drop down to lower levels. This photon emission or luminescence can occur by a number of mechanisms, but in this work only photoluminescence is going to be discussed.

Among the solid group, semiconductors have inter band luminescence due to electron hole recombination. This electron hole recombination can be radiative or non-radiative. In a radiative process photons are emitted and in a non-radiative process phonons are generated. During Photo luminescence process, light with sufficient energy incident on the material and some electrons are excited to the conduction band. Some of these electrons will go through radiative transitions

and some through non-radiative transitions. Radiative transition can be conduction band to valence band and also conduction band to a defect state. These defect states are in between the valence and conduction band.

The spontaneous emission rate for radiative transitions between two levels is determined by Einstein's A coefficient [38]. If the upper level has a population N at time t then the radiative emission rate is given by,

$$\left(\frac{dN}{dt}\right)_{radiative} = -AN \quad (2.4)$$

The above equation can be solved to give,

$$N(t) = N(0) \exp(-At) \quad (2.5)$$

$$N = N(0) \exp\left(-\frac{t}{\tau^R}\right) \quad (2.6)$$

During this process, radiative recombination has to compete with non-radiative recombination which has a life time τ^{NR} . Therefore total rate for electron hole recombination can be written as,

$$\left(\frac{dN}{dt}\right)_{total} = \left(\frac{dN}{dt}\right)_R + \left(\frac{dN}{dt}\right)_{NR} = -\frac{N}{\tau^R} - \frac{N}{\tau^{NR}} = -N\left(\frac{1}{\tau^R} + \frac{1}{\tau^{NR}}\right) \quad (2.7)$$

where $\left(\frac{dN}{dt}\right)_{total}$ is the total rate of electron hole recombination, $\left(\frac{dN}{dt}\right)_R$ is the radiative recombination rate, $\left(\frac{dN}{dt}\right)_{NR}$ is the non-radiative recombination rate, τ^R is the radiative recombination life time, and τ^{NR} is the non-radiative recombination life time.

2.3.2. Free Carrier Generation

When a light of intensity I is incident on a sample of thickness z , the loss of intensity δI due to absorption within the slice can be calculated from Beer-Lambert's law,

$$\delta I = \alpha * I * dz \quad (2.8)$$

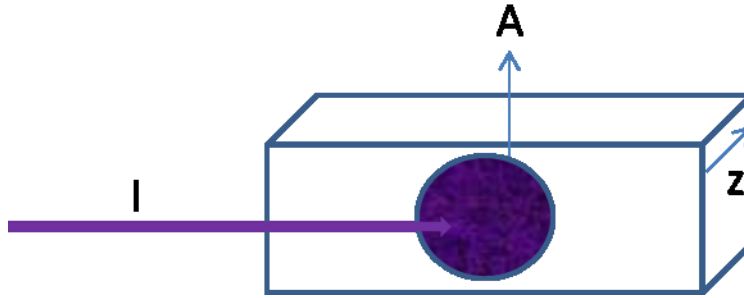


Fig. 2.3.1. Schematic of PL excitation.

In Fig. 2.3.1, UV light which is above the band gap of ZnO is incident on an area of A and thickness z . For ZnO, $\alpha = 2 \times 10^5 \text{ m}^{-1}$ for above bandgap excitation. We assume that each absorbed photon generates an electron hole pair. The number of electron hole pairs generated within the δz thickness slice per unit time is given by,

$$\frac{\text{Total Energy of the Photon}}{\text{Energy of Each photon}} = A * \frac{\delta I}{h\nu}$$

Here, ν is the frequency of the incident photon and h is the Planck's constant ($6.62607004 \times 10^{-34} \text{ m}^2 \text{ kg.s}^{-1}$). Now the carrier generation rate G per unit volume can be estimated as,

$$G = \frac{\text{Number of electron hole pair generated per unit time}}{\text{Volume}}$$

$$G = \frac{A\delta I/h\nu}{A\delta z} = \frac{\alpha I}{h\nu} \quad (2.9)$$

The rate equation for carrier density can be written as,

$$\frac{dN}{dt} = G - \frac{N}{\tau} = I * \frac{\alpha}{h\nu} - \frac{N}{\tau} \quad (2.10)$$

where τ is the recombination lifetime of electrons. For steady state condition, the rate of change of carrier density should be zero, $dN/dT = 0$. Hence,

$$N = \frac{I\alpha\tau}{h\nu} \quad (2.11)$$

When the excitation of the PL is performed with a CW laser, τ is the characteristic life time of the dominant free carrier recombination mechanism [39]. In ZnO, typically free electron hole populations decay in $\tau \gg 10$ ps, according to the time resolved PL measurements done by different research groups for the free exciton emission which was dominant in their PL spectrum [40, 41, 42]. In case of short pulse excitation like fs pulsed excitation the excitation pulse is shorter than all the recombination life time and $\tau = \tau_{excitation}$ [43].

Chapter 3

Experimental set up

Fabrication and characterization of thin film samples were done using different equipment and experimental methodologies in this thesis. This chapter provides an overview of the major equipment and experimental set ups used throughout the project.

3.1. Pulsed Laser Deposition System

The PLD system in this study is a combination of a vacuum chamber and a Krypton Fluoride Excimer laser emitting at 248 nm. A substrate heater was installed in the chamber for the heated growths.

3.1.1. Vacuum System

In this project, all thin film samples were deposited in an aluminum chamber of approximately 70 L in volume. It uses a diffusion pump (with the support of a rotary backing pump) to achieve a vacuum of 5×10^{-5} torr. The pressures are monitored by a Pirani gauge (for the range between atmospheres to 10^{-3} torr) and a cold cathode gauge (pressures down to 10^{-6} torr). A picture of the vacuum system is shown in Fig. 3.1.1.

In the initial stage of this work this vacuum system was rebuilt with some major replacements. The pneumatic gate valve was replaced by a manual gate valve and cold trap for liquid nitrogen was introduced in the middle of the gate valve and diffusion pump. The other major change was in one of the chamber windows which was next to the laser input window. For heated growths, a conductive substrate heater manufactured by NEOCERA (Part# PTC2) was installed in the chamber with an adapter to fit in the chamber window next to the laser incoming port so that the target can be at 45° angle to the incident laser beam and the substrates can be placed parallel to

the target at a distance of 3 cm. All these adapters were made by the ECE Machine shop employees. Some other vacuum parts were bought from Kurt. J. Lesker Company Ltd.

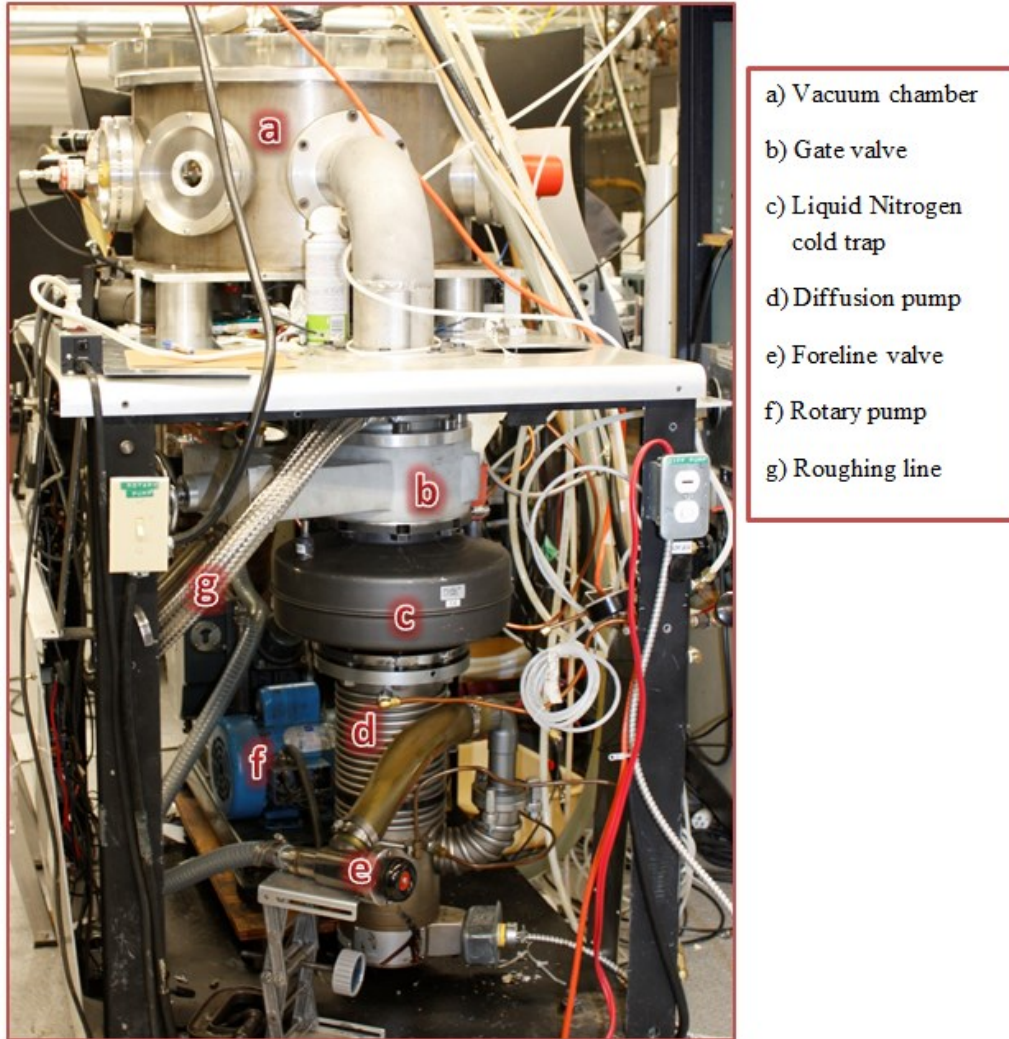


Fig. 3.1.1. Vacuum system for PLD.

3.1.2. Deposition Setup

A (99.99%) sintered ceramic ZnO disk was used as the target (Kurt J. Leskar Company Ltd.) for deposition. The target was rotated during deposition. Oxygen (99.99%) was used as an ambient background gas for the deposition of ZnO thin films and Nitrogen (99.99%) was used to vent the chamber after growth.

The experimental set up for depositions is shown in Fig. 3.1.2. Mirror 1 and Mirror 2 are dielectric mirrors with high reflectivity at 248 nm. These mirrors are used to fold the beam to the target so that the distance between target and substrate can be optimized according to the needs of the experimental setup. For ZnO growths we used the substrate to target distance 3 cm.

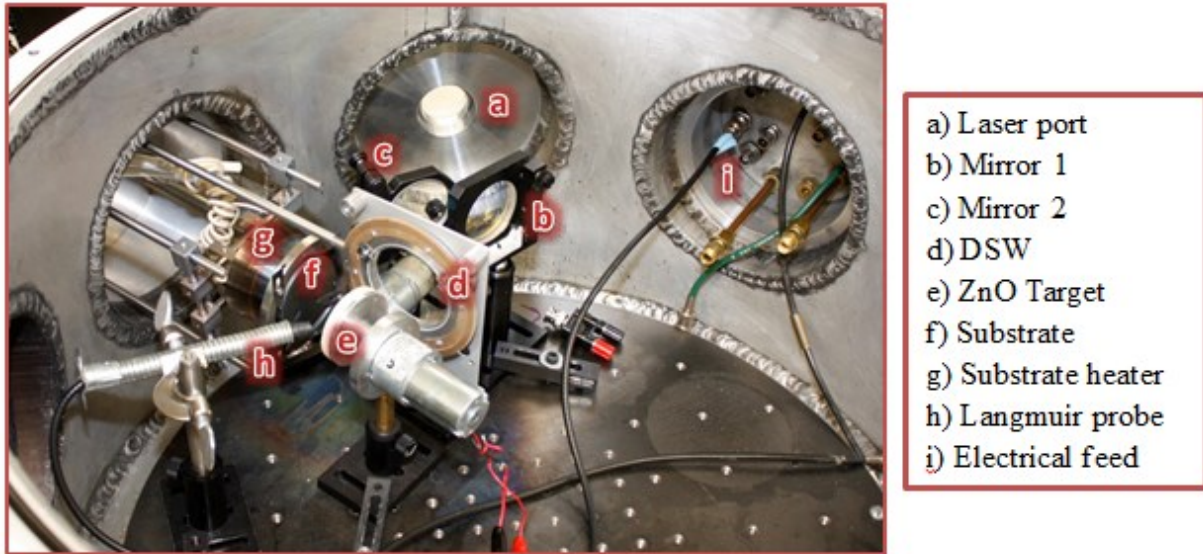


Fig. 3.1.2. Experimental set up for PLD.

The conductive ceramic heater used in this set up had a 2 inch circular area to mount the substrate. The main attractive feature of this heater is it can operate at maximum temperature (950 °C) from full vacuum to atmospheric oxygen. A K-Type thermocouple was used for temperature measurements. A temperature controller is used to maintain the substrate temperature within accuracy of $\pm 5\%$ of the set point. An important note here is the ceramic material from which the heater is manufactured will degrade if the temperature is more than 980 °C. So it is recommended from Neocera not to exceed the controller temperature more than 950 °C. The electrical feedthrough and the flange assembly to install it in the chamber were provided by the manufacturer.



Fig. 3.1.3. PLD heater manufactured by Neocera Inc. [44].

Fig 3.1.3 shows the PLD heater with the vacuum flange. To mount the substrate on the 2 inch ceramic heater surface Silver paint bought from Ted Pella Inc was employed. The surface of the heater was first cleaned by light sanding and wiping with methanol. Then a drop of paint was applied and the substrate was located in its position. In this method some paint residues were left on the other side of the deposited film of the substrate. This makes the surface uneven and difficult to mount for other characterizations.

To avoid this scenario a clamp was made using stainless steel to hold the substrate tightly in contact with the heater. The length of the legs of the clamps could be varied depending on the size of the sample. Fig. 3.1.4 is showing a schematic of the substrate mounting clamp. It was secured tightly with the heater neck with a setscrew.

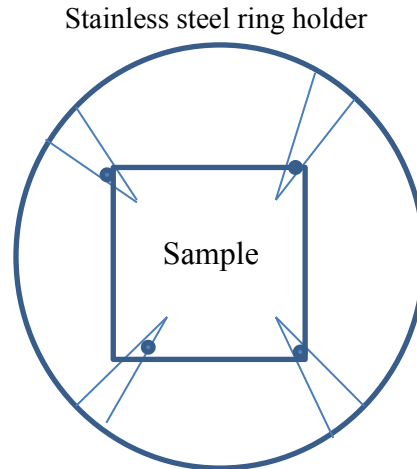


Fig. 3.1.4. Schematic diagram of the Clamp for substrate mounting on the heater.

3.1.3. Laser and Optics

The laser used for the deposition experiments was a Krypton Fluoride (KrF) laser (manufactured by Lambda Physik), emitting at 248 nm with a pulse duration of 25 ns and repetition rate of 20 Hz. UV mirrors were used to fold the laser into the chamber laser input port and a 50 cm focal length plano-convex (PCX) lens with adjustable position was used to focus the laser beam on the target. The lens positions were adjusted so that the target was located at a slightly defocused region to obtain appropriate spot size for the desired fluence.

A debris shield window (DSW) was placed in front of the chamber window to protect the chamber window from coating during deposition. The transmission of the DSW was measured after every run and it was found that after approximately 25000 laser pulses the transmission drops from 90% to 80%. The DSW was then cleaned with 13% Ammonia Bifluoride solution to restore the transmission back to 90%. Laser fluence (energy per unit area of the laser spot) is an important parameter for PLD deposited ZnO thin films. Laser energy was monitored using a calibrated photodiode during the growth and the laser beam spot was measured using a CCD camera in off-line experiments.

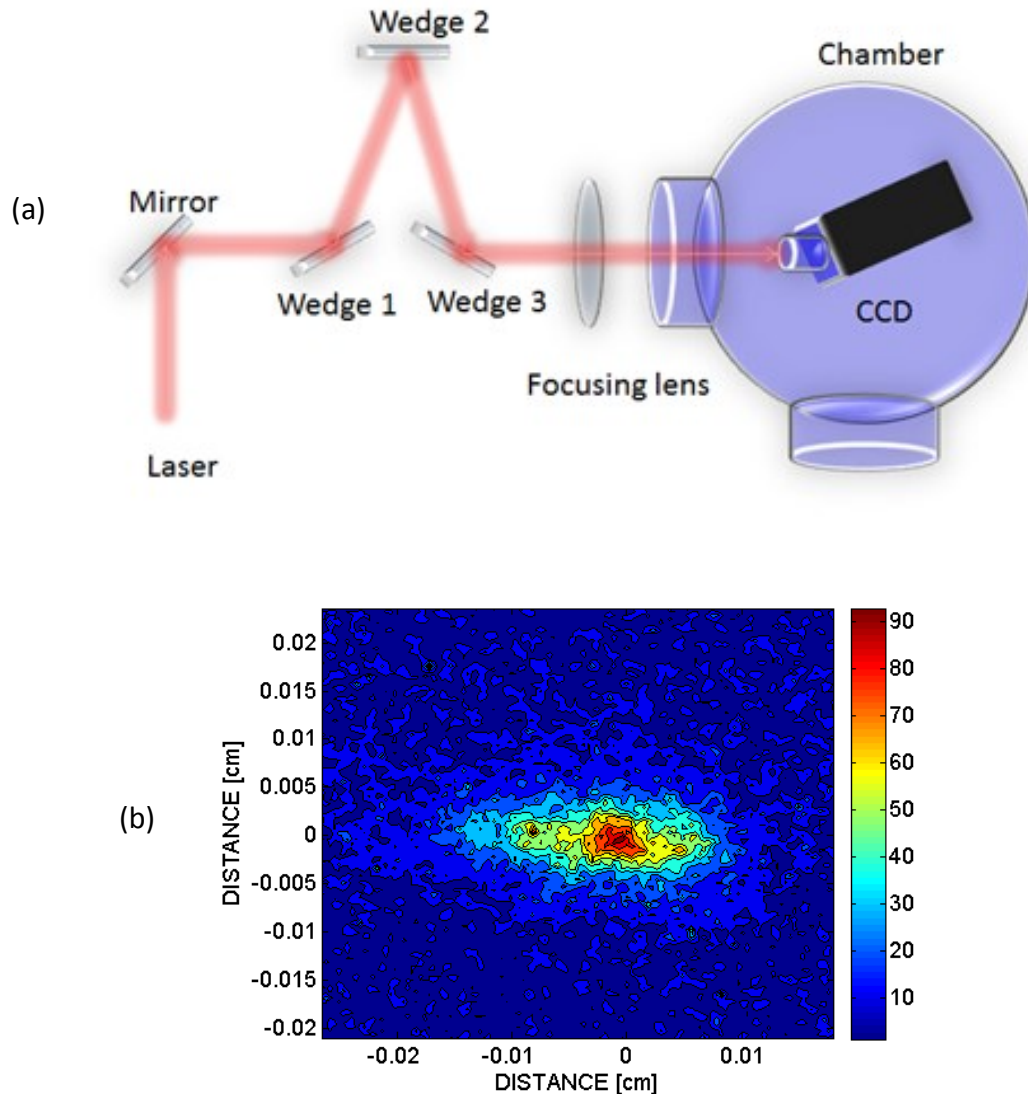


Fig. 3.1.5. (a) CCD measurement set up for the beam spot measurement and (b) a representative contour plot of the intensity profile.

Fig. 3.1.3(a) shows the laser spot measurements setup. The setup consists of three fused silica wedges and a CCD camera. Each wedge reflects 4% of the laser energy, to reduce the energy incident on the CCD to avoid any damage. The CCD camera is placed in approximately the same position as the target in the PLD set up. The focusing lens distance is varied to obtain laser spot size at various positions along the laser axis. The location of the best focal position in the chamber is taken to be the same as where the minimum spot size is. A representative contour plot of the intensity profile of the laser is also shown in Fig. 3.1.3(b). The image taken by the CCD is

analyzed using a Matlab script to obtain the 90% energy contour of the spot. This is then used to determine the spot size, which in turn gives us the fluence.

3.2. Calibrated Photodiode for Laser Energy Monitoring

The laser beam energy was monitored by a calibrated silicon photodiode (PD 20) using leakage light from mirror (M) as shown in Fig 3.2. The photodiode was calibrated by placing a wedge in front of the chamber window to reflect 4% of the energy of the laser beam onto a calorimeter (PY4). The PY4 calorimeter was also calibrated using a commercially calibrated calorimeter (Gentec). The KrF laser typically gives laser energy of ~ 70 mJ per pulse during the deposition. Fig. 3.2.1 shows the experimental set up for the Photodiode and calorimeter calibration.

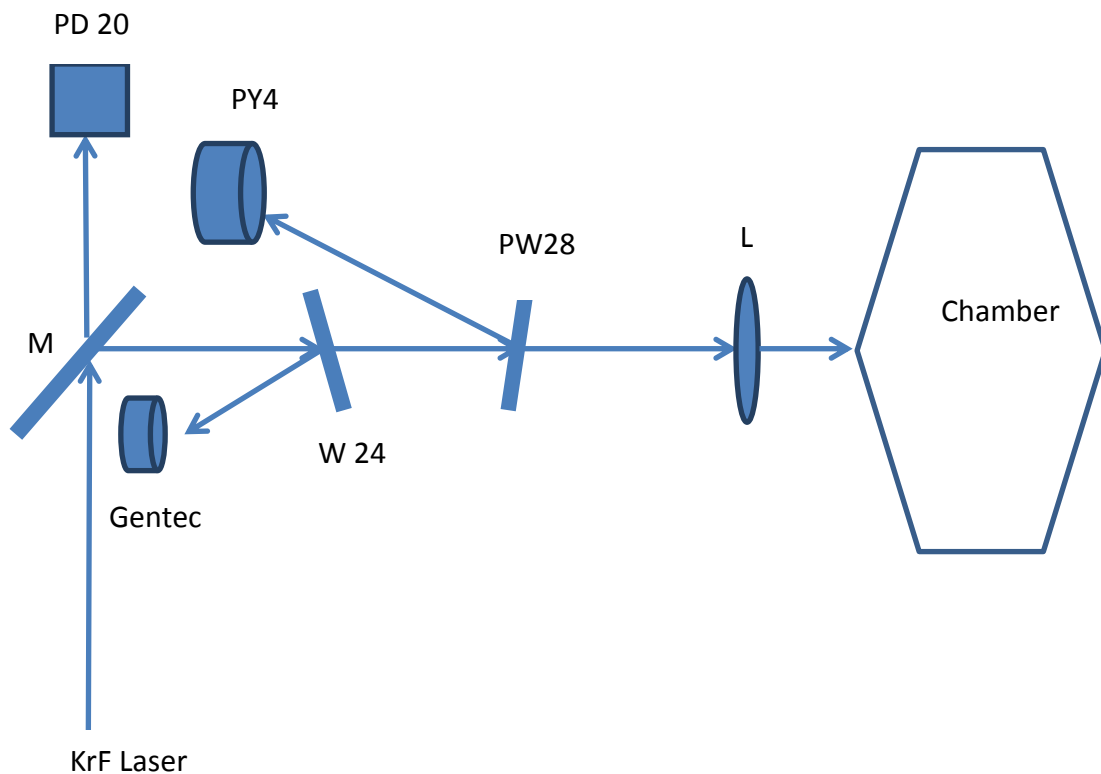


Fig. 3.2.1. Photodiode calibration and laser energy measurement set up.

3.3. Plasma Plume Monitoring with Langmuir Probe

Langmuir probes (LP) were used to study the energetic particles of the laser produced ZnO plasma. It is named after famous Nobel laureate Irving Langmuir. He had outstanding contributions in different fields of physics and also invented this probe to calculate plasma parameters [44] like electron temperature, ion velocity, ion kinetic energy etc.

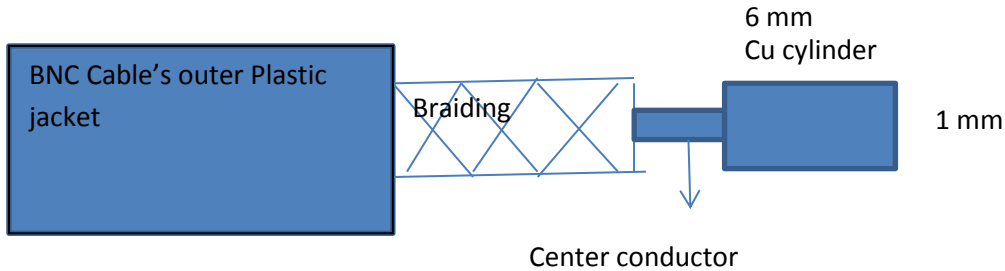


Figure 3.3.1. A simple Langmuir probe.

Figure 3.3.1 is a schematic diagram of a typical cylindrical Langmuir probe used for this work's plasma diagnosis. A copper cylinder of 6 mm height and 1 mm radius was soldered on top of the center conductor of a BNC cable to make a simple cylindrical probe for plasma monitoring.

Off-line experiments were done with two of these probes one placed at the same position where the substrates are usually placed during the growth to get the information about the energetic particles reaching the substrates and the other at 45° with respect to the target which was implemented permanently in the chamber during the actual thin film growths. This Probe was used to monitor the laser produced ZnO plasma before each run to ensure repeatability of the film quality.

In Figure 3.3.2 the experimental set up for the Langmuir probe experiment is shown along with the CKT diagram of the bias box.

The rotating ZnO target was at 45° incidence with the oncoming laser. It was rotating at 12 rotation per minute with one inch radius of rotation to ensure the laser is exposed to different spots at different time.

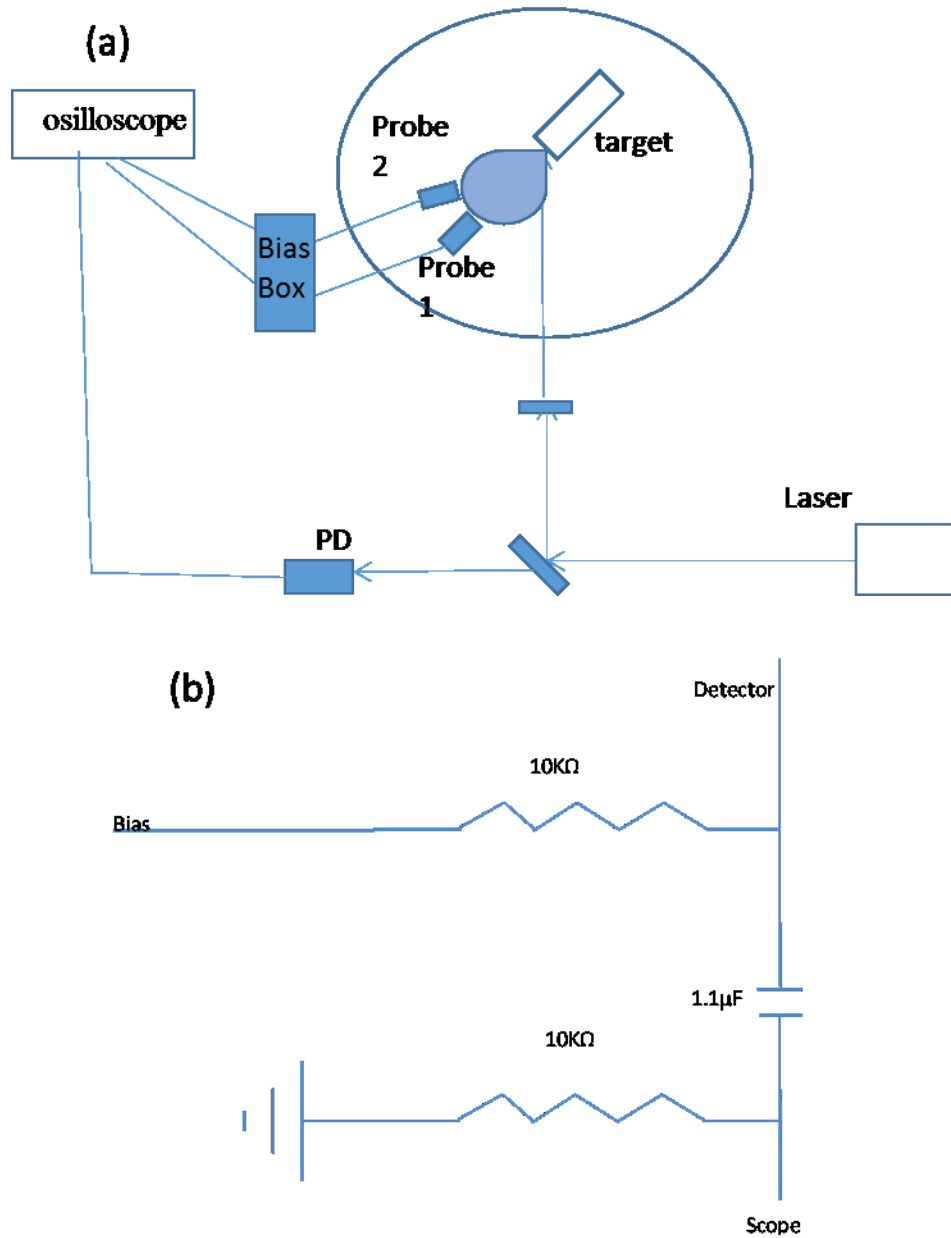


Figure 3.3.2. (a) Experimental set up and (b) Bias box CKT diagram for the Langmuir probe experiment.

Probe no. 1 was placed exactly at the substrate position for the thin film growths. i.e. normal to the target surface and at a distance of 3 cm from the target. Probe no. 2 was placed at 45° angle with respect to the target. Laser energy was monitored by the calibrated photo diode described in

section 3.2 of this chapter. The signals from the PD and both probes were collected using a Tektronix oscilloscope (1 M Ω internal impedance).

Ion probe signals are recorded for the pressure of 5×10^{-5} Torr. A negative bias of -40 V is used to attract ions. A 50 Ω terminator was used for impedance matching. Ion probe signals were recorded at different lens positions to change the fluence and observe the effect on the ion velocity and energy at different fluence. Also the number of ions calculated from the ion probe signal at different fluence gives an indication about the growth rate at different fluence.

Ion velocity and energy were calculated using this experiment at different fluence. Thin films grown by PLD have significant effect on their film properties due to higher ion energy [34]. Higher energy ions should play important role for low temperature crystalline film deposition.

3.4. Growth Characterization Techniques

3.4.1. X-Ray Diffraction

X-ray diffraction (XRD) is a widely used technique for structural investigation of bulk materials and thin films. It can provide information about different crystal orientation and their distribution, average crystal size and internal stress in a sample. When X-ray propagates through a sample material it interacts with the crystal lattice and is diffracted according to Bragg's law

$$2d \sin \theta = n\lambda \quad (3.1)$$

Where d is the atomic spacing, θ is the scattering angle, n is an integer, and λ is the X-ray wavelength. λ is in the range of Angstrom which is comparable to the interatomic spacing d in crystalline materials.

For bulk materials and powder samples, the conventional XRD method known as Bragg Brentano or θ - 2θ is popular but in case of thin film characterization Glancing Angle XRD (GLAD) is more appropriate. GLAD enhances the surface sensitivity of the measurement and eliminates any unwanted contribution from the substrate.

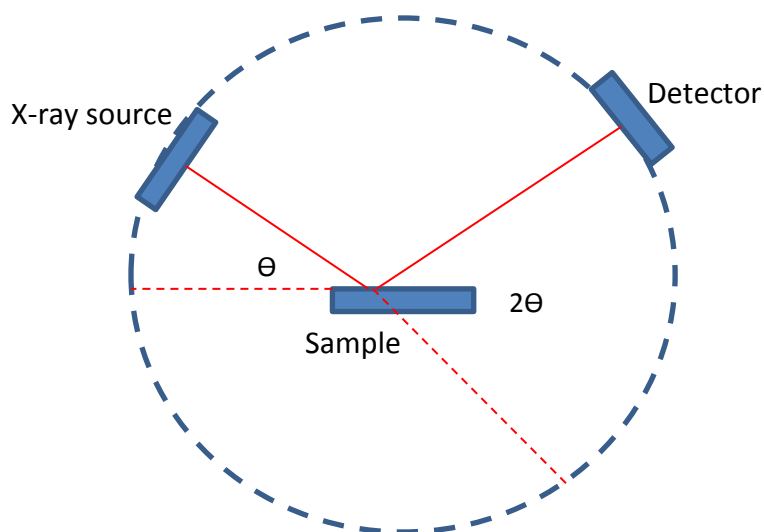


Fig. 3.4.1. A schematic diagram of XRD measurement set up.

In the Bragg Brentano scan, both the detector and X-ray sources shown in Fig. 3.4.1 are moved in a coupled manner to get the scan performed. On the other hand, for GLAD measurements, the X-ray source is fixed at a small angle and only the detector is scanned to get the surface information for thin films and multilayer structures.

In this work, GLAD X ray diffraction (XRD) of all the samples were measured using Rigaku X-ray diffractometer (Cu-K α radiation, $\lambda = 1.5405 \text{ \AA}$) to obtain their crystal structure. The commercial ZnO wafer (bought from MTI) was measured using the conventional method but all our thin film samples grown on different substrates were measured at 1 degree glancing angle.

3.4.2. Scanning Electron Microscopy

The morphology of a sample surface can be characterized using a scanning electron microscope (SEM). In this instrument, a beam of thermionically emitted electrons from a tungsten filament scanned repeatedly across the surface of a sample under vacuum. The backscattered electrons from the scanned area are detected and converted into an optical image which gives an unprocessed view of the sample surface created by the local variations of the electron emissivity of the surface. In this project, SEM of the samples was carried out using JAMP-9500F (JEOL) for grain size analysis and morphological understanding.

3.4.3. Atomic Force Microscopy

A second imaging technique, atomic force microscopy (AFM) was used to characterize samples. Using this imaging technique information about the structures is collected and roughness of the surface can also be measured. The AFM has different ways to analyze the surface of a sample. The main two modes are contact mode and tapping mode. In this work, tapping mode was mainly used to gather surface information using Veeco DI 3100. A sharp tip with a nominal tip radius of 5 nm was used for this purpose.

3.4.4. Film Thickness Measurement

Thickness of all the PLD samples were measured ex-situ with stylus profilometry using NanoFab's (at University of Alberta) Alpha step IQ. This machine can measure the thickness with an accuracy of ± 5 nm. To use this method the sample should be masked during deposition to get a nice sharp step to measure the thickness. Otherwise, lithographic etch after deposition can also make the step height. Room temperature samples were masked using two different methods. One was using carbon vacuum friendly tape and the other was using a sharpie pen to draw thick lines on them. Carbon tape was working fine but sometimes some tape residues made the measurements difficult where is the sharpie masking which were washed with iso-propyl alcohol (IPA) after deposition was a much cleaner process.

For high temperature deposition, Kapton tapes were used to mask the sample and thickness measurements. These tapes are made of Kapton polyamide film with Silicon adhesive. They are good for a wide range of temperature. In this case we used it for the growths where the substrate temperature were less than or equal to 250 °C.

Very high temperature depositions were measured using Filmetrics (F20), also in NanoFab. This does not need any kind of masking as the measurement is done by reflecting light on the sample over a range of wavelengths. Due to the wave nature of light, constructive and destructive interferences can occur when light reflects from the top or bottom surfaces of a film depending on the wavelength. A characteristic intensity oscillation can be obtained for a given range of wavelength (intensity vs. wavelength). This measured value is be fitted with a calculated value using the material optical parameters of the thin film and substrate structure. Optical parameters

for ZnO were in the material library of the device but parameters for the ZnO/SiO₂/Si structure was created using the edit structure option of the software using the nominal thicknesses of each layer.

3.4.5. Photo Luminescence Measurement Setup

In this project, we studied both time integrated and time resolved PL of thin film ZnO samples deposited by PLD and a commercially made ZnO wafer.

(a) Time integrated PL (TIPL) set up

For all PL measurements, the excitation lasers were incident on the sample surface at an angle of incidence of 10°. As shown in Fig. 3.4.2, a pair of 2.5 cm diameter lenses (5 cm and 10 cm focal lengths) was used to collect the PL emission normal to the sample surface. This lens combination was used to collect and focus the light into the entrance of the Ocean Optics spectrometer.

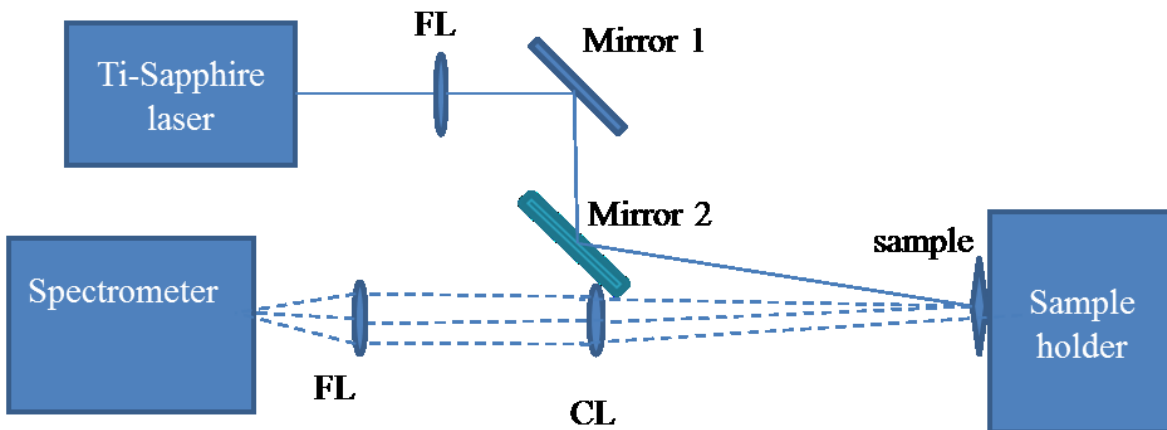


Fig 3.4.2. PL measurement set up for time integrated measurement.

A CW He-Cd laser with 15 mW average power and a beam diameter of 2 mm was used to perform the time integrated PL measurements for CW excitation. For nanosecond (ns) excitation, a frequency quadrupled Nd:YAG laser (Big Sky Ultra) at 266 nm (6 ns pulse duration) was used.

Laser energy was measured to be around 1.2 mJ using a calibrated calorimeter. A laser spot size of around 1 mm in diameter was used to excite the samples.

For femtosecond (fs) excitation, a Ti:Sapphire (Spectra-Physics Hurricane) laser was used to generate 180 fs (FWHM, measured by autocorrelation assuming a Gaussian pulse shape) pulses at 800 nm. Part of the main pulse was then frequency doubled by using a BiBO nonlinear crystal to 400 nm. A frequency tripled laser pulse of 266 nm was generated by the use of an additional BBO crystal through mixing both 800 nm and 400 nm under phase matched conditions. This was the excitation line for our femtosecond excited PL measurement for both time integrated and time resolved cases. The energy of the 266 nm line was measured to be 4 μ J using a commercial power meter (Spectra Physics 407A TC). The laser spot was slightly focused to obtain a 1 mm diameter spot on the sample.

(b) Time resolved PL (TRPL) measurement

266 nm wavelength laser pulses obtained from the Ti:Sapphire laser as used for the time integrated measurement was used for the TRPL measurement as an excitation source. For the time resolved (TR) measurement, a streak camera (Hamamatsu streak unit C979) combined with an intensified charge-coupled device (ICCD, Andor DH720-25U-03) was used. The streak speed was set to 15 mm/ns, and an entrance slit of 30 μ m was used to achieve the optimum resolution of 15 ps. In the actual measurement, multiple shot accumulations are needed because the single shot signal of the PL from our PLD deposited film cannot be well resolved from the background noise. However, the shot to shot jittering from the laser system and the streak camera can deteriorate the time resolution. The jittering from multiple shot accumulations led to a Gaussian instrument response with FWHM of \sim 50 ps. The TRPL signals from our samples were convoluted by the Gaussian instrument response function resulting in a near Gaussian distribution. The TRPL of the PLD film on SiO₂ has a FWHM of around 50 ps and hence is instrumentation limited.

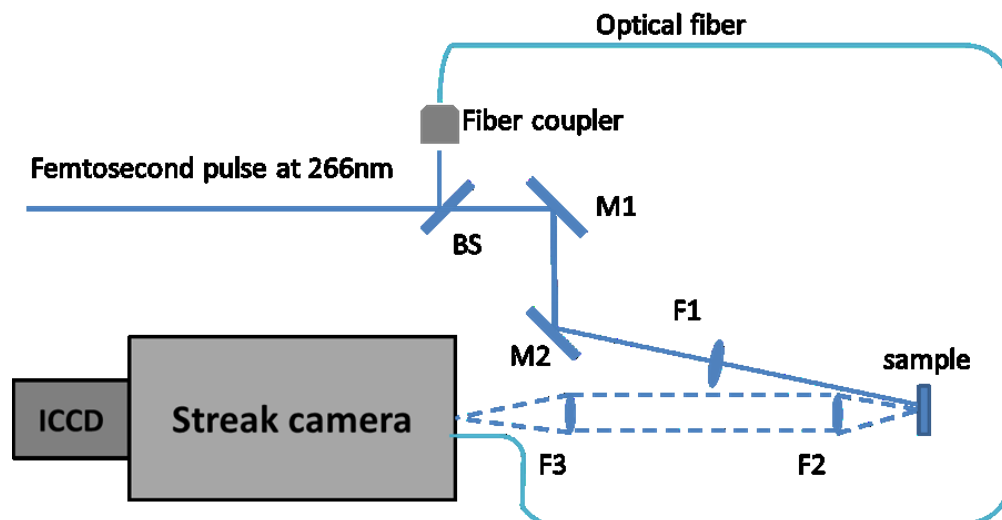


Fig. 3.4.3. Schematic diagram of TRPL setup with fiducial monitor. M1 and M2 are dielectric mirrors coated with high reflectivity coating at 266 nm. BS is beam splitter with 10% reflection and 90% transmission. F1, F2 and F3 are lenses of 2.5 cm diameter, whose focal distances are 10 cm, 5 cm and 10 cm respectively.

To improve the instrument response we introduced a fiducial monitor system [46] using an optical fiber on the streak camera which carries a portion (10%) of the excitation laser pulse as a time reference to correct the jittering effect. The details of the process are described in [46]. 100 and 1000 shots were accumulated for ZnO single crystal wafer and ZnO PLD thin film samples, respectively. The fiducial monitor or optical marker was present with every shot to provide the time reference and a Matlab script was used to align all the shots together depending on the markers position. The setup is shown in Fig. 3.4.3. After using this technique we were able to improve the detector response for multiple shot accumulations down to ~ 15 ps.

A streak camera can measure ultrafast light pulse and provide information about intensity as a function of time [46]. It is a two dimensional system but can be used in combination with a spectroscope to measure the time variation of the incident light intensity with respect to wavelength (time resolved spectroscopy). The working principle of streak camera consists of multiple steps. First the ultrafast light signals needed to be analyzed are incident through the entrance slit on a photocathode which instantaneously converts them to electrons. Then they pass through horizontal electrodes and accelerated by an electric field and finally hit the phosphor screen. The screen is then imaged on a highly sensitive camera (in this case an ICCD was used to

create the image). The temporal profile is transferred to the spatial profile by using two vertical sweep electrodes. High voltages are applied synchronously with the incidence of the electrons so when they hit the screen these electrons are swept by the electrodes and hit in different spatial points depending on their temporal position.

Chapter 4

Growth Parameter Optimization for ZnO Thin Films

Growth parameters of PLD have great influence on the deposited material properties. The four major PLD growth parameters for ZnO deposition are oxygen partial pressure, laser fluence, substrate temperature and post growth annealing conditions. These parameters for our deposition system needed to be explored and understood in order to achieve proper control to manipulate and reproducibly fabricate device quality thin films. The first part of this chapter is about growth parameter optimization of PLD for Thin Film Transistor (TFT) application and the second part describes the temperature dependence study of PLD grown ZnO thin films on both SiO₂/Si and sapphire substrate. As the very first step to achieve the goal of this thesis, these were varied to optimize the thin films mobility and carrier concentration for their potential TFT application. The mobility of the material is directly related to the drive current of the resulting thin film transistor. Depending on the combination of variable parameters the carrier concentration can be optimized and mobility can be improved. The structural, optical and electrical properties of ZnO under different growth and annealing conditions by PLD are investigated and discussed.

The results from the first part of this chapter (growth parameter optimization for TFT application) are reported in [48]. Fabrication of thin films using PLD with different growth conditions was done as the part of this project and other reported electrical measurements and characterization analysis were done by Prof. Manisha Gupta.

4.1. Calculating ion velocity, energy and the effect of laser fluence on them using Langmuir Probe

Langmuir probe measurements were done with different fluence by changing the beam spot size with different lense positions and the corresponding maximum ion flux velocities and densities were measured to see their effects on the film properties to optimize a suitable fluence for thin film ZnO using PLD.

Figure 4.1.1 is showing an example of the ion probe signal for ZnO target with -40 V bias when the probe is positioned at 3 cm from the target and normal to the target surface.

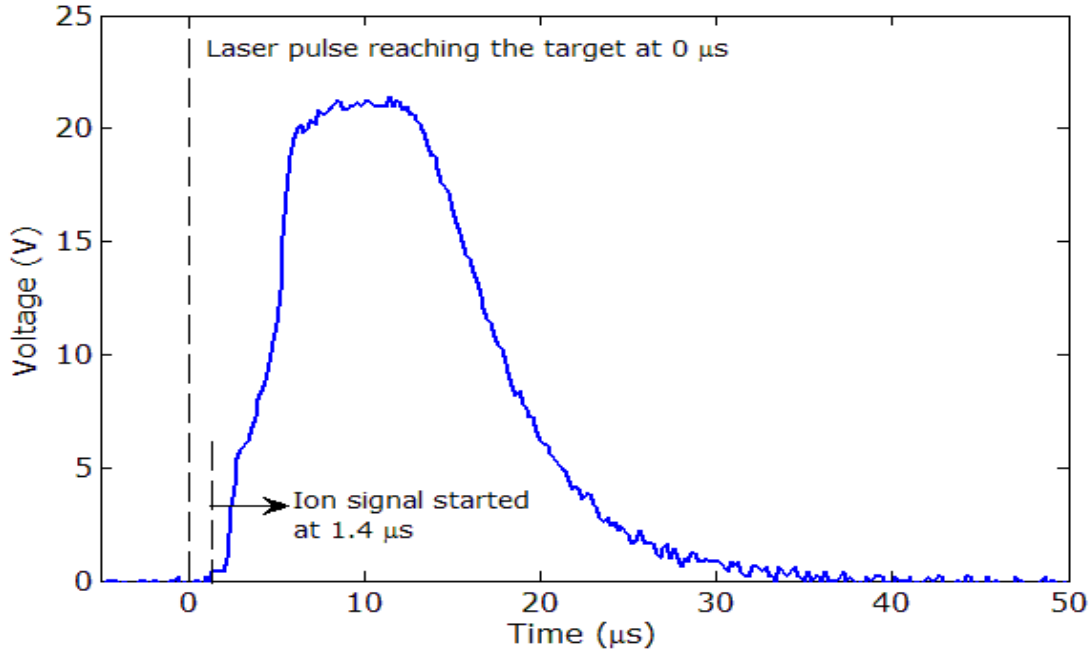


Fig. 4.1.1. The ion probe signal detected by the Langmuir probe for ZnO target.

The ion signal detected by the oscilloscope showed a delay of about 1.4 μs from the time when the laser hit the target. This indicates that the ion reached the probe well after the ns laser pulse was terminated. The highest ion density was reached after around 3.4 μs and after that the ion density decreased.

When an ion probe is facing a plasma flow and at negative voltages high enough to prevent the electrons with the highest thermal energies in the plasma from reaching the probe then the detected ionic density and plasma flow velocity has a relationship with the ion saturation current which can be written as [49],

$$I_{ion\ saturation} = eVAn_i \quad (4.1)$$

Where e is the electronic charge, V is plasma flow velocity, A is the surface area of the probe and n_i is the ion density. Integrating both sides with respect to time,

$$n_i = \frac{q_{ion}}{(A * e * d)} \quad (4.2)$$

Where q_{ion} is the total charge of the ions and d is the distance from the target to probe. Using the above equations, the ion density was calculated for different fluences.

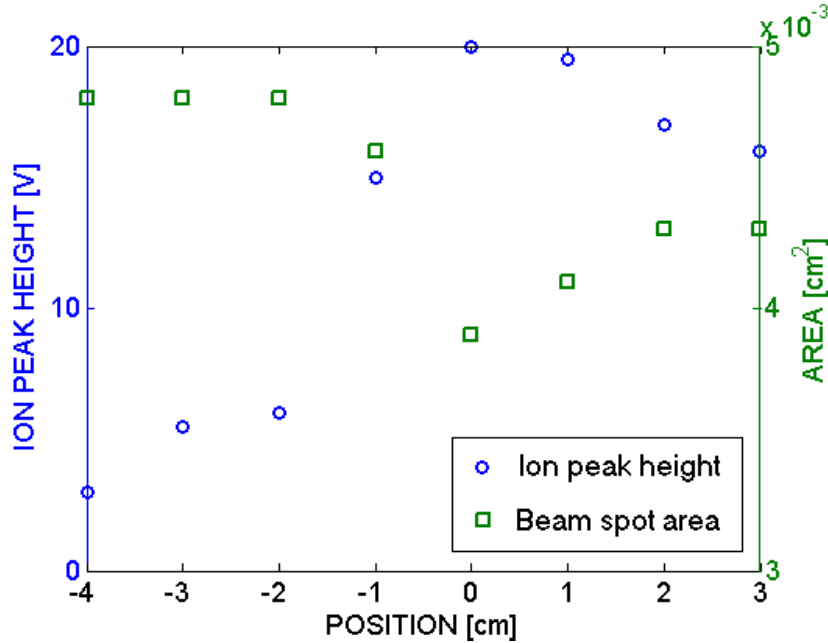


Fig. 4.1.2. The ion probe signals at different lens positions.

Fluence was varied from 1.5 J.cm^{-2} to 11.45 J.cm^{-2} using different lens positions to change the beam spot area measured by CCD according to Chapter 3. With higher fluence the intensity of the ion peak was increased.. Figure 4.1.2 is showing the variation of the ion peak height with different beam spot size.

For different fluence the velocity varied from 6 km.s^{-1} to 25 km.s^{-1} and the ion density varied from $2.7 \times 10^{17} \text{ m}^{-3}$ to $1.9 \times 10^{18} \text{ m}^{-3}$. The ion density value obtained at 2.25 J.cm^{-2} fluence is well in agreement with K. J Saji *et. al.* [50] PLD created ZnO plasma ion density ($7.2 \times 10^{17} \text{ m}^{-3}$) for a fluence of 2 J.cm^{-2} . B. Toftman *et. al.* [49] also reported the typical PLD created plasma ion density in the range of 10^{17} m^{-3} under similar fluence.

According to V. Craciun *et. al.* [51] the ablation threshold for ZnO is lower than 0.7 J.cm^{-2} for a KrF ($\lambda=248 \text{ nm}$) ns laser which is similar to our deposition laser wavelength and time period.

Even at that low fluence they observed that the ablated material was not enough to create dense plasma. In this range of low fluences the laser-matter interaction process is more similar to thermal evaporation than ablation. They reported that a range of fluence 1.5 -2.5 J.cm⁻² is better for ZnO deposition as fluence more than that may degrade the crystalline quality of the films due to superheating of the target which may create micro-explosions within the melted material. Their prediction of bulk micro-explosion with higher fluence using thermal simulation was also observed in the SEM of ZnO thin film deposited at more than 3 J.cm⁻²[51]. According to this study the working window for ZnO PLD thin film fluence chosen was 1.5 J.cm⁻² - less than 3 J.cm⁻².

Table 4.1. Fluence growth rate, ion density, ion velocity, and crystal orientation of PLD grown samples.

Fluence (J.cm⁻²)	Ion density (cm⁻³)	Ion velocity (km.s⁻¹)	Growth rate (nm/pulse)	Crystal orientation (002/100)
1.87	3.2x 10 ¹⁷	6	5.3x 10 ⁻³	0.53
2.5	6.8x 10 ¹⁷	11	7.3x 10 ⁻³	6.06
4.75	2.1x10 ¹⁸	25	8.7x10 ⁻³	0.93

Three different fluences were used to deposit ZnO thin films which were 1.8 J.cm⁻², 2.5 J.cm⁻² and one slightly higher than the reported value which is 4.75 J.cm⁻². Table 4.1 shows different fluence growth rate, ion density and ion velocity for our PLD grown samples with their crystal orientation using XRD. All these samples were grown with 100 mtorr oxygen pressure as good quality ZnO thin films need to be grown with oxygen partial pressure and annealed in air for 3 hours after growth.

It can be seen from table 4.1 that the growth rate increases when the ion density increases. For very high fluence with very high ion velocity the sample did not achieve a good crystal orientation which was reflected in the XRD measurements [48] of the samples. This fluence dependence study was the part of the work reported in [48]. The study reflects the deposition fluence window for our PLD deposited ZnO which is in agreement with the literature [51].

Usually higher energy ions are known for their added energy to grow crystalline films. It is obvious that there is an optimum fluence and ion velocity after which it degrades the film crystal orientation from (002) to other orientations like (100) and (110) due to superheating. Additionally, very high deposition rate can reduce the chance for the adatoms to reach a suitable site. For these PLD growths it was found that 2.5 J.cm^{-2} fluence has the most optimum ion velocity and deposition rate for mostly (002) oriented crystal.

4.2. Substrate Heater calibration for PLD growths

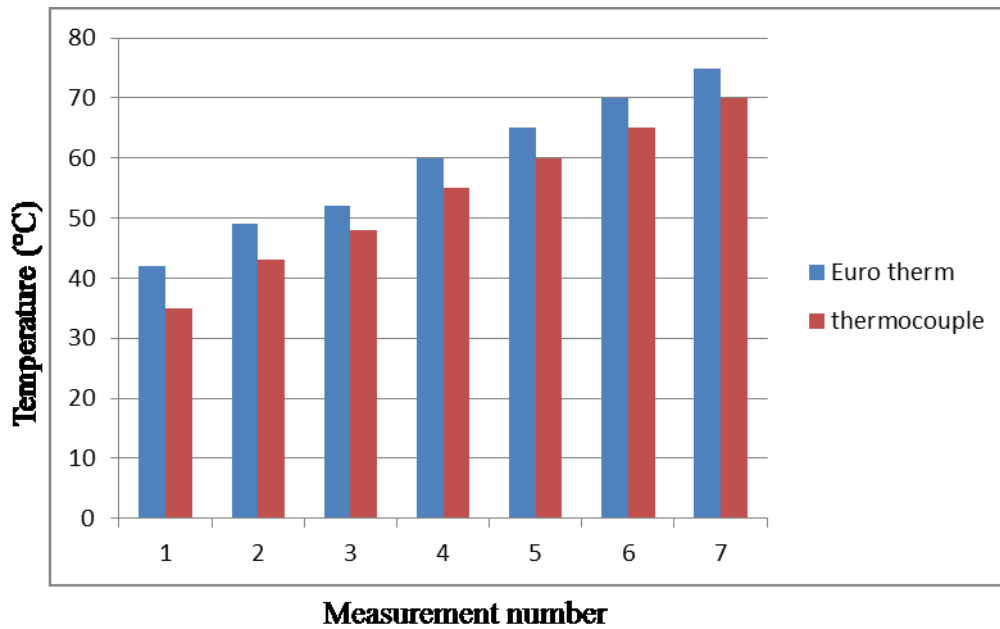


Fig 4.2.1. A bar graph to compare the Eurotherm temperature controller with the actual substrate temperature.

The substrate heater was calibrated using a calibrated K-type thermocouple connected with a multi-meter which gave the temperature in °C. Eurotherm was the built in temperature controller

which also used a K-type thermocouple to measure the heater temperature. A bar graph for different temperatures from room to 100 °C is shown in Figure 4.2.1.

It can be seen that from the graph that the Eurotherm temperature was almost 6 to 7 °C higher than the actual temperature measured using the calibrated thermocouple for lower temperature like 40 or 50 °C but as the temperature increases to 60 °C and upwards, the difference between two temperatures is almost always 5 °C (Eurotherm indicated 5 °C more than the actual temperature). So when we consider the substrate temperature we consider it as 5 °C lower than what the temperature controller is showing.

4.3. Growth Parameters Optimization for TFT Application

The main goal of this part of the work was to increase the mobility of thin film ZnO and optimize the carrier concentration so that it can be more suitable for TFT application. ZnO films of 50 ± 10 nm thickness were deposited on 200 nm thick SiO₂ film on Si substrates with various different conditions. Laser fluence was varied from 2.5 J.cm⁻² to 4.75 J.cm⁻² and oxygen partial pressure was varied from 10 to 300 mtorr. Multiple samples were grown with each set of growth parameters and each growth condition sets had one unannealed, one oxygen annealed, and one air annealed samples. The substrate - target distance for all the films was maintained at 3 cm for all the growths. After room temperature growths, some samples were annealed at 650 °C for 3 hours in Air or Oxygen environment. XRD pattern of the samples showed that samples grown at 2.75 J.cm⁻² fluence and 100 mtorr oxygen pressures were gave the maximum improvement in crystal orientation along (002) after air or oxygen annealing. These two conditions were used then for the heated growths. The deposition conditions are listed in Table 4.2.

Rate of deposition for the samples varied with oxygen partial pressure and laser fluence. For different oxygen partial pressure it varied from 6.6 pm/ pulse (10 mtorr) to 4.8 pm /pulse (300 mtorr) and at high fluence (4.75 J.cm⁻²) it was 8.3 pm/pulse.

Table 4.2. PLD growth conditions of the different ZnO 50 ± 10 nm thick samples along with the post-growth annealing conditions [48].

Experiment	Sample	O ₂ partial pressure (mTorr)	Fluence (J.cm ⁻²)	Growth temperature/ Annealing
1	1-A	10	2.75	Room temp, un annealed
	1-B	10	2.75	Room temp, Annealed in O ₂
	1-C	10	2.75	Room temperature Annealed in Air
2	2-A	50	2.75	Room temp, un annealed
	2-B	50	2.75	Room temp, Annealed in O ₂
	2-C	50	2.75	Room temperature Annealed in Air
3	3-A	100	2.75	Room temp, un annealed
	3-B			Room temp, Annealed in O ₂
	3-C			Room temperature Annealed in Air
4	4-A	150	2.75	Room temp, un annealed
	4-B			Room temp, Annealed in O ₂
	4-C			Room temperature Annealed in Air
5	5-A	300	2.75	Room temp, un annealed
	5-B			Room temp, Annealed in O ₂
	5-C			Room temperature Annealed in Air
6	6-A	100	2.5	Room temp, un annealed
	6-B			Room temp, Annealed in O ₂
	6-C			Room temperature Annealed in Air
7	7-A	100	4.75	Room temp, un annealed
	7-B			Room temp, Annealed in O ₂
	7-C			Room temperature Annealed in Air
8	8-A	100	2.75	250 °C substrate temperature

4.3.1. Structural and Morphological Study

X-ray diffraction (XRD) measurements at 1 degree glancing angle were made on all the samples to study the crystal structure of the ZnO thin films. Figure 4.3.1 is a summary plot for all the samples mentioned in Table 4.2. It shows the XRD plots of the three samples 3-A, 3-B and 8-A. It can be observed that the room temperature growth without annealing show very little (002) phase formation and the (110) phase is dominant. XRD plot for room temperature growths with oxygen and air annealing demonstrate multiple peaks at the (100), (002), (101), (102), and (110) planes, which are described as peaks for Wurzite ZnO nanoparticles in literature [52]. This may indicate that annealing the room temperature growths in air or O₂ atmosphere is leading to formation of ZnO nanoparticles. Also, it is observed that for sample 8-A (grown at 250 °C), the (002) is dominant though (110) is very weakly present. For all the room temperature growths, (110) was the dominant crystal orientation. The post-growth annealing and heated growth reduce defects and increase crystallinity as we can see the intensity of the (002) peak enhances after post growth annealing.

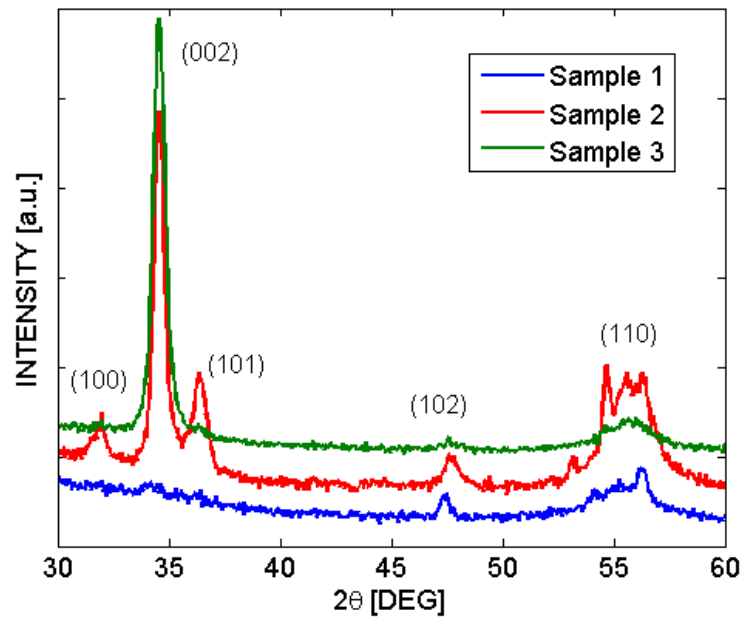


Fig 4.3.1. Glancing angle X-ray diffraction (XRD) plots for different PLD samples, sample 3-A was grown at room temperature, sample 3-B was grown at room temperature and post growth oxygen annealed and sample 8-A was grown at 250 °C substrate temperature.

It is found in the literature that films with higher (002) orientation has higher mobility.[53]. We observe that the (002) peak shifts to higher 2θ , 34.27° to 34.55° , from room temperature to 250°C growth, this is consistent with the results observed by other groups [53]. J.B. Franklin et al [53] observed the (002) peak shift to higher 2θ value for a substrate temperature range 50°C to 450°C for their PLD deposited ZnO thin films on ITO substrates. Also, the heated growth, 6U, (002) peak is at 34.55° , which is reported as the (002) peak position for single crystal ZnO [52]

The full-width half maximum (FWHM) of the (002) peak for the heated growth is 0.59 deg 2θ (sample 6U) as compared to the FWHM of room temperature samples with post-growth annealing at 0.473 deg 2θ (sample 3A) and 0.53 deg 2θ (sample3O). As compared to the other studies [53], the FWHM of the heated growth is larger at 0.59 deg 2θ as compared to 0.28 deg 2θ . This may be due to the different growth conditions (laser frequency 8 Hz, target substrate distance 5 cm and laser fluence 0.85 $\text{J}\cdot\text{cm}^{-2}$, oxygen pressure 5 - 50 mtorr, ITO substrate, and thicker films 120 - 250 nm) [53].

Analyzing XRD peak profile can also contribute to the knowledge about the crystal size. Using Debye-Scherrer formula which was published in 1918 the grain size can be analyzed from the XRD peak profiles [54],

$$B(2\theta) = \frac{K\lambda}{\beta\text{Cos}\theta} \quad (4.1)$$

where B is the crystal size, K is Sherr constant ~ 1 , λ is the wavelength of the X-Ray source (for the Cu-K α radiation, $\lambda=1.5405$ Å), and β is the FWHM of the peak.

Using the above equation the crystal sizes were calculated. All the samples had smaller crystal size compared to the grain size measured in SEM and AFM. For example, it was observed that, the 250°C substrate temperature sample had crystal sizes ranging from 80 - 140 nm using SEM an AFM but using Sherrer formula the crystal size was only 14.3 nm. From equation (4.1) we can see that the crystal size is inversely proportional to the FWHM of the peak. According to literature [50], there are multiple factors which can cause the broadening of the FWHM besides the crystal size. Peak broadening due to instrumental profile can have major contribution in the

broadening of FWHM. Every diffractometer has its own instrumental profile which can be measured using a standard known sample and then the contribution from the instrument can be determined. We should deconvolute the real FWHM from the instrumental profile [55],

$$\beta = \beta_s - \beta_{ins} \quad (4.2)$$

where, β_s is the total FWHM of the peak and β_{ins} is the broadening due to instrumental profile [55]. XRD measurements for thin film samples in this work were performed using a Rigaku X-Ray diffractometer as mentioned in Chapter 3 which belongs to the NanoFAB of University of Alberta. The instrumental profile was unknown during this work.

To compare with the existing literature a single crystal ZnO wafer hydrothermally grown by MTI was measured with the same X-Ray diffractometer. The crystal size of similar ZnO wafer manufactured by MTI was calculated around 1.8 microns according to the existing literature [56].

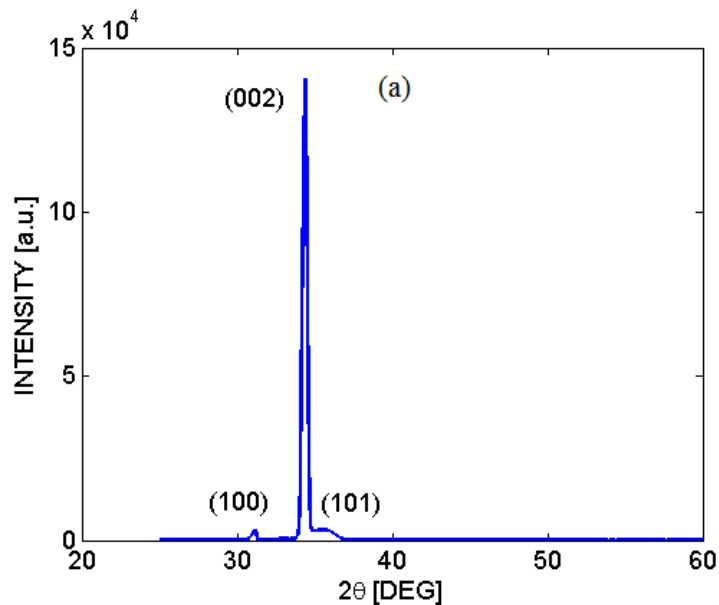


Fig 4.3.2. X-ray diffraction (XRD) plot for hydrothermally grown ZnO single crystal wafer by MTI.

Fig. 4.3.2 is showing the measured XRD plot of ZnO single crystal wafer bought from MTI. The FWHM of the (002) peak at 34.55 deg 2θ is around 0.05 deg. This gives us a crystal size around

0.18 microns. This calculated value is ten times smaller than the known value [53]. This XRD result cannot be compared with our thin film grain size analysis as the thin film XRD were done in GLAD method.. Considering this effect can make the grain size calculation more precise [55].

SEM of the samples was carried out using JAMP-9500F (JEOL) for grain size analysis and morphological assessments. SEM images of the samples grown at different growth conditions are shown in Fig. 4.3.3. All the SEM images are at 50,000x magnification with the scale bar of 100 nm. These samples have been grown at 100 mtorr oxygen pressure and at 2.75 J.cm^{-2} laser fluence either at room temperature or at $250 \text{ }^\circ\text{C}$. Fig. 4.3.2 (a), (b), and (c) show the SEM images of unannealed, air annealed and oxygen annealed room temperature growth ZnO sample.

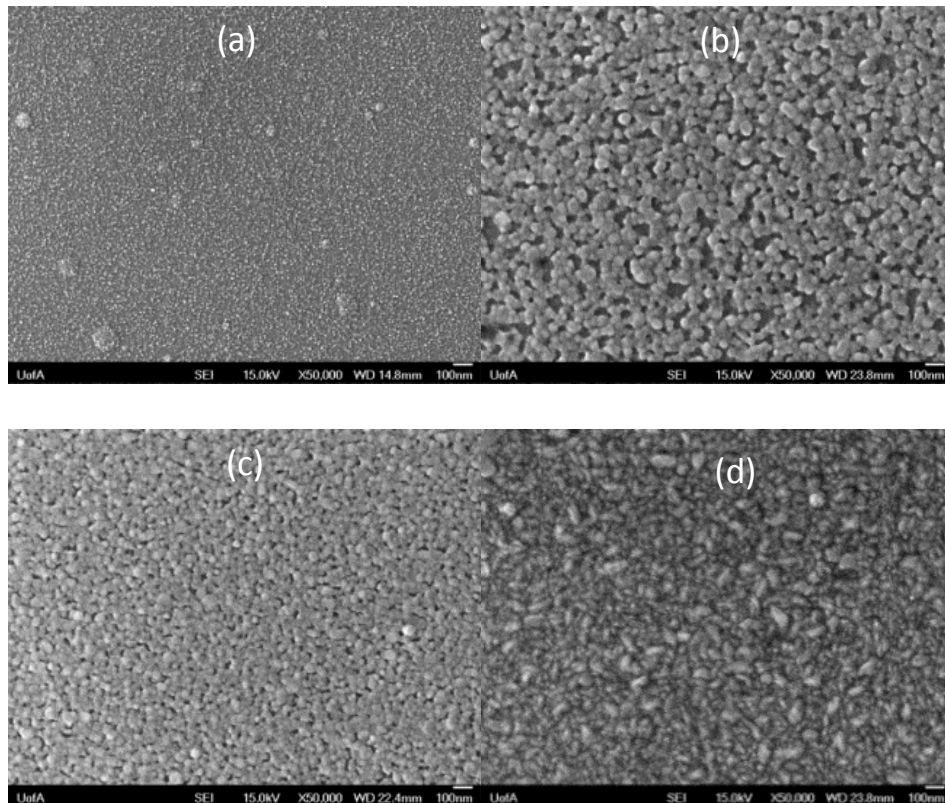


Fig 4.3.3. SEM images at 50,000x magnification with the scale bar of 100 nm. (a) SEM of unannealed 100 mtorr, 2.75 J.cm^{-2} , room temperature growth of ZnO, indicating small grain size of 3-4 nm. (b) and (c) SEM after annealing the sample in O_2 and air, it can be observed that the grains have grown, but there are spaces between the grains. (d) Unannealed grown at 100 mtorr, 2.75 J.cm^{-2} , $250 \text{ }^\circ\text{C}$ indicating larger grains and very dense film with no cracks.

It is observed that the grains are around 3 - 4 nm for the as grown sample and they grow larger with post-growth annealing. The grain size ranges between 20 - 55 nm for the air annealed sample and are circular in shape. For the oxygen annealed sample the grain size ranges between 20 - 70 nm in diameter. There is a large variation in the grain sizes in the annealed samples and also the presence of voids can be observed between the grains for both the air and oxygen annealed samples. The presence of voids is likely to reduce the electron mobility of the ZnO. The SEM image of the heated growth exhibits a very dense film with no voids. The grains in this sample exhibit irregular shape and are varying from 20 - 140 nm in length. This sample has a relatively high mobility of $8 \text{ cm}^2\text{V}^{-1}\text{s}^{-1}$. Mobility of this sample was measured by Hall measurement and reported in [48]. The high mobility is due to the dense film with no voids and good crystal structure. All the other samples demonstrate mobility in the range of $0.01 - 0.1 \text{ cm}^2\text{V}^{-1}\text{s}^{-1}$; this has been obtained from field effect transistor (FET) device measurements [9].

AFM was done using the Veeco DI 3100 instrument using tapping mode. The grain size and shapes observed from the SEM images correlates with those observed with the AFM also. A representative AFM picture is shown for the sample which was grown at $250 \text{ }^\circ\text{C}$. The surface roughness of these films was also measured using the AFM images. The roughness was in a range of 1.1 nm - 2 nm.

Fig. 4.3.4 shows a representative AFM image of the ZnO thin films grown on SiO_2/Si at $250 \text{ }^\circ\text{C}$ with oxygen partial pressure of 100 mtorr and 2.5 J.cm^{-2} laser fluence.

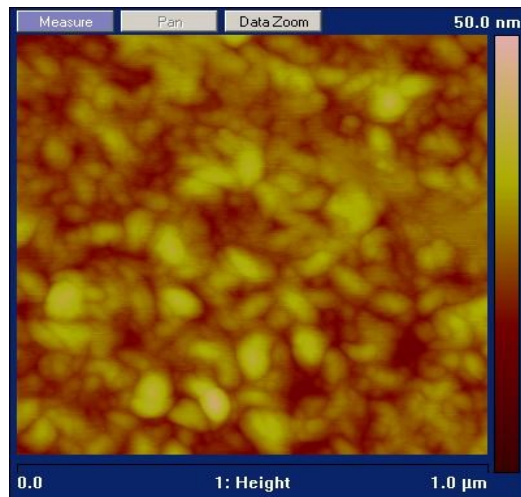


Fig. 4.3.4. AFM image of the un-annealed film grown at $250 \text{ }^\circ\text{C}$ on SiO_2/Si [46].

4.3.2. Electrical Measurements

Sheet resistivity and mobility were measured by Hall measurements on the sample. Mobility of the room temperature growths with post-growth annealing could not be measured using Hall setup. This was because their sheet resistance was very high and mobility was low. The resistivity of the room temperature growths with post-growth annealing (samples 1-5) indicated a very high resistivity in the range of 4 - 95 k Ω -cm and extremely low mobility in the range of 0.01 - 0.1 cm²V⁻¹. The sheet resistance of the heated growth sample 8-A were measured as 1857 Ω /square and the mobility was measured as 8 cm²V⁻¹s⁻¹. Using the Hall measurement the carrier concentration was measured as 5x10¹⁵ cm⁻³ and C-V measurements for carrier concentration was varied from 1.3 x10¹⁵ to 2.6x10¹⁵ cm⁻³. Despite the difference between the two measurements the order of the carrier concentration was in agreement with each other. This low carrier concentration indicates that there are less defects or traps present in the ZnO. Hall measurements were done by Dr. Manisha Gupta and results were reported in [48]. Figure 4.3.5 is showing the range of values for doping concentrations in different ZnO samples all grown at 250 °C on SiO₂/Si using the C-V measurements.

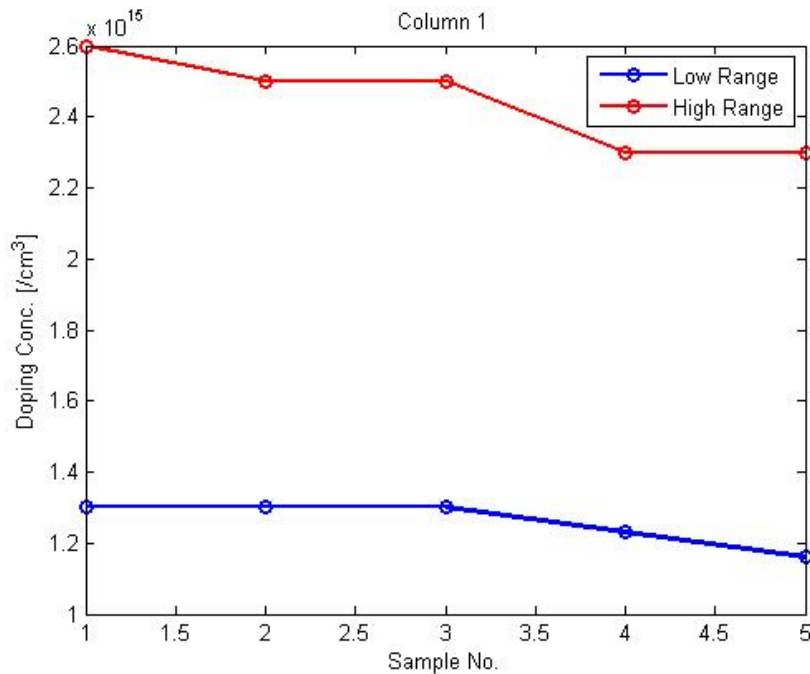


Fig. 4.3.5. Calculated doping concentration of 250 °C ZnO samples using C-V measurements.

4.4. Temperature Dependency

Substrate temperature is an important parameter for thin film growths. During deposition ad-atoms move in the surface to find a suitable place. It will stop when it finds the lowest energy nearby. To increase the surface mobility of ad-atoms to reach suitable positions substrate heating is important. In order to study the temperature effect, substrate temperatures were varied from 25 – 700 °C and sapphire (Al_2O_3) was used as a substrate.

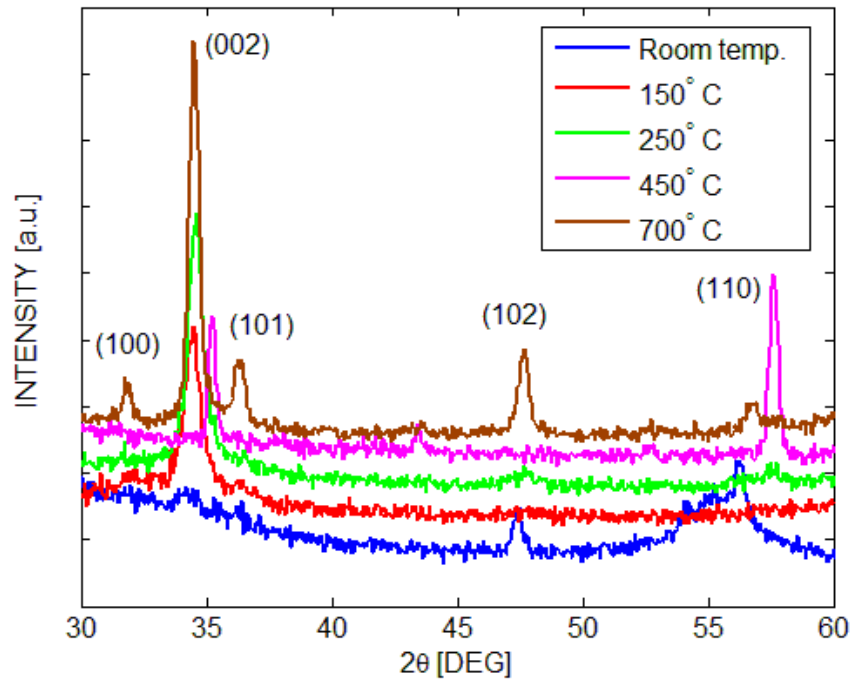


Fig. 4.4.1. XRD plot for different temperature growths on Sapphire substrate.

The XRD spectra of ZnO thin films grown on sapphire substrates at various growth temperature are shown in Fig. 4.4.1. It is observed that significant amount of crystal orientation along (002) started with low temperature (150 °C) growth also. The sample grown at 150 °C has dominant (002) crystal orientation with no other significant phase formation. The 250 °C grown sample has even higher intensity for the (002) peak compared to the 150 °C growth with no other phase formation. The sample grown at 450 °C showed multiple phase formation with (100), (002), and (102) major peaks which indicate the deterioration of the c-axis orientated growth. The very high temperature growth which was done at 700 °C also has the (002) dominant phase present

but it has the indication of multiple weak phases. According to previous reports, increasing the growth temperature of ZnO thin film on sapphire substrate improves its structural properties [53] however this result concerning the substrate temperature dependency of ZnO thin films on sapphire substrate indicates that there might be an intermediate growth temperature in between 250 °C to 450 °C for optimum growth of c-axis (001) oriented crystals which enhance the mobility.

Table 4.3. Summary table for temperature dependence study.

Substrate Temperature	Major Phases present	(002) peak position (DEG)	FWHM of (002) peak (DEG)
Room (25 °C)	(102),(110)	Very weak (002) peak	X
150 °C	(002)	34.45°	0.7
250 °C	(002)	34.55°	0.5
450 °C	(002),(110)	35.25°	0.3
700 °C	(002)	34.6°	0.45

Table 4.3 is a summary of the structural investigation of the films grown at different temperature using the XRD data. The best condition according to this study for the desired (002) oriented film is 250 °C substrate temperature growth condition. Which has the (002) peak positioned at the same position of single crystal ZnO. The smallest FWHM of (002) phase was achieved with 450 °C substrate temperature but this peak position shifted to 35.25 presence of multiple phases specially the dominant (110) phase made this sample inferior. In reported literature FWHM as small as 0.18 was also reported for PLD deposited ZnO on sapphire that might be due to higher film thickness and larger grain size [56].

Another set of samples were deposited under the same oxygen partial pressure (100 mtorr) and laser fluence (2.5 J.cm^{-2}) with two different substrate temperatures (250 °C and 700 °C). In this part of the study both sapphire and SiO_2/Si were chosen as substrates.

During the XRD measurement for structural information 2Θ were varied in a larger range from 20 to 70 degrees.

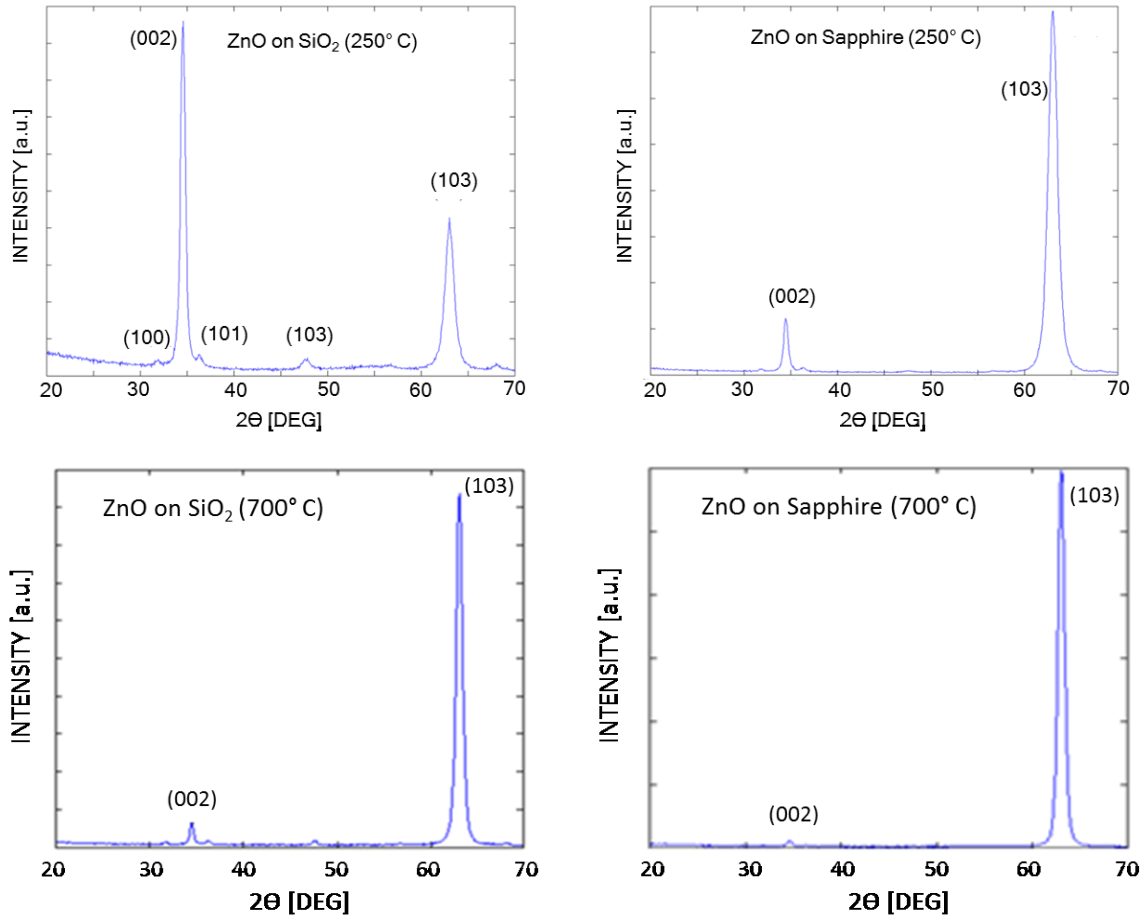


Fig. 4.4.2. XRD plot for different temperature growths on Sapphire and SiO_2/Si .

From Fig. 4.4.2 it is observed that ZnO samples deposited on sapphire and SiO_2/Si at 250 °C can be described using two peaks one at $2\Theta = 34.55^\circ$ and another at $2\Theta = 62.88^\circ$. These are respectively (002) and (103) crystal phases for hexagonal wurzite ZnO [58]. (002) was the dominant peak for ZnO on SiO_2/Si but for sapphire (103) became the dominant phase. With the higher substrate temperature (103) became the single dominant phase for both the substrates.

According to literatures (002) is easier to form because of its lowest surface free energy [59]. (103) is difficult to form but some groups reported this kind of growth mode change for sputtering deposited ZnO thin films [58] and PLD deposited ZnO thin films with different experimental parameters (oxygen partial pressure 1 Torr, laser repetition rate 10 Hz) [59]. In our case also a transition of growth mode from (002) vertical to (103) lateral was clearly observed for higher substrate temperature for both the substrates. Jang *et. al.* [54] reported this orientation change but with different oxygen partial pressures and (002) was still the dominant phase for their samples. Nandi *et. al.* [60] obtained (103) dominated ZnO films on Si using RF magnetron sputtering. Though (002) has the lowest formation energy the reason behind the (103) orientation majority can be due to release of excess energy of the adatoms in a form of formation energy. Ion assisted thin film growths have higher energy ions and if the substrate temperature is also very high they might use that energy to form an orientation which has a higher formation energy. Thus leading to the growth of (103) orientation.

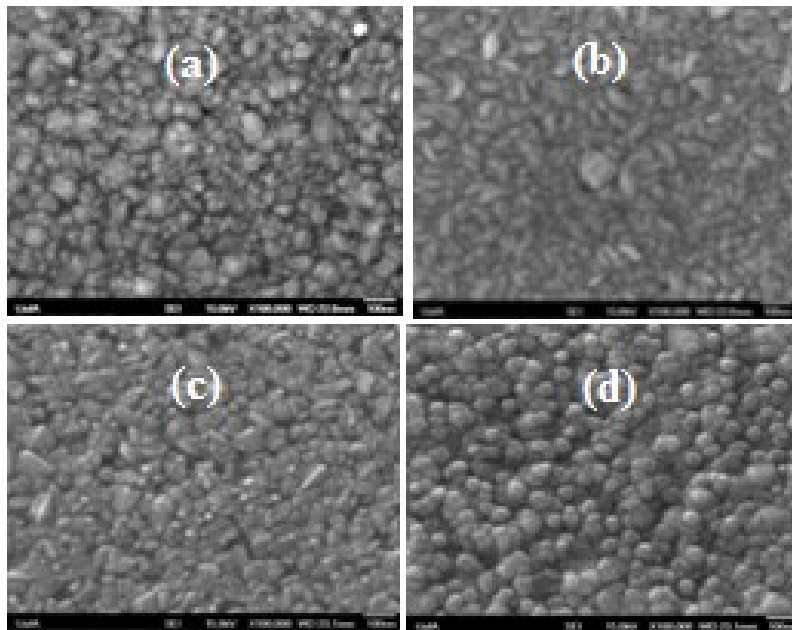


Fig. 4.4.3. SEM images of ZnO thin film on (a) SiO₂/Si at 250 °C, (b) Sapphire at 250 °C (c) SiO₂/Si at 700 °C and (d) sapphire at 700 °C.

Surface morphologies of these films were investigated using SEM images. Grains were clearly seen for all the samples. They varied in size from 60 to 150 nm for different samples. Image analysis were done using ImageJ software to measure the grain size. Irregularly sized grains

become more distinct in size and shape with higher temperature and growth mode change. Higher temperature makes the grains more tightly packed but the grain size did not increase significantly with the rise in substrate temperature beyond 250 °C. But grain size improved significantly from 25 °C to 250 °C growth. It appears that after a certain temperature, grain sizes do not increase significantly. L. Avril *et. al.* [58] also reported that after a certain substrate temperature (375 °C) the grain sizes of their ZnO thin films were not changing. 250 °C grown substrate temperature ZnO sample grown on sapphire substrate (Fig. 4.4.3 b) has irregularly shaped grains varied in size from 50 to 100 nm and 700 °C sapphire sample (4.4.3 d) had more distinct grain boundaries with mostly round shaped grains of 100 to 120 nm. For ZnO growths on both the SiO₂/Si substrates grains were irregularly shaped and varied in size from 50 to 120 nm.

A comparison between the grain sizes obtained by SEM and calculated using XRD FWHM for is given in table 4.4.

Sample	SEM grain size (nm)	RD grain size (nm)
ZnO on SiO ₂ at 250 °C	80-90	15.26
ZnO on Sapphire 250 °C	90-95	17.2
ZnO on SiO ₂ at 700 °C	100-120	18.66
ZnO on Sapphire at 700 °C	60-100	16.22

The mobility of the 250 °C ZnO samples were 16 cm²V⁻¹s⁻¹ and 8 cm²V⁻¹s⁻¹ respectively for sapphire and SiO₂/Si substrates. Hall measurements were done by Prof. Gupta. The sapphire substrate was c-axis cut which should facilitate the c-axis oriented growth mode for ZnO thin film and hence enhance the mobility.

4.5. In situ cooling in oxygen atmosphere

Some Thin film ZnO deposited on sapphire at higher temperature than the room were cooled inside the chamber after growth with an oxygen background pressure of 100 mtorr. These samples were also characterized using XRD and Hall measurements. It was found the in situ oxygen cooling made the mobility higher which was around $18 \text{ cm}^2\text{V}^{-1}\text{s}^{-1}$ according to Hall measurement but at the same time it increased the carrier concentration $\sim 10^{19} \text{ cm}^{-3}$. Thus oxygen may reduce oxygen vacancies which help to improve mobility but at the same time may generate other defects which contributes to the carrier concentration. This high carrier concentration may not be very suitable for TFT applications as carrier concentration is required to be in a certain range which is similar to semiconductors carrier concentration for devices using Schottky contacts. If the carrier concentration is in the range of 10^{19} the samples become very metallic and they start forming ohmic contacts instead of Schottky contacts. Samples with carrier concentration in the range of 10^{15} /cm^3 exhibited the potential to form good Schottky contacts with metals like gold.[9].

4.6. Summary

In the first part of this chapter, ZnO thin films with higher electron mobility and optimized carrier concentration in order to form Schottky contacts were main goal for the TFT application. Film thickness was kept 50 nm according to the TFT applications demand. and substrate choice was SiO_2/Si to match with the device requirement for TFT fabrication. A number of growth parameters like fluence, oxygen partial pressure, growth temperature, post growth annealing were varied to optimize the mobility, carrier concentration and crystal orientation.

For room temperature growths with a fluence of 2.5 J.cm^{-2} and 100 mtorr oxygen partial pressure exhibited improved grain size (around 70 nm) and more (002) crystal orientation after a post growth annealing at $675 \text{ }^\circ\text{C}$ in air and oxygen environment. These room temperature films had a carrier concentration in the range of 10^{17} - 10^{18} cm^{-3} but the presence of voids which was clearly seen in the SEM image decreased the electron mobility in the range of 0.01 - $0.1 \text{ cm}^2\text{V}^{-1}\text{s}^{-1}$.

The ZnO sample grown at $250 \text{ }^\circ\text{C}$ without post growth annealing had larger grain size (100-120 nm) and higher (002) crystal orientation ratio. These ZnO sample also had a lower carrier

concentration in the range of 10^{15} cm^{-3} and almost 100 times higher mobility ($8 \text{ cm}^2\text{V}^{-1}\text{s}^{-1}$) compared to the room temperature annealed sample. This lower carrier concentration indicated lower defect levels and the SEM image exhibited closely packed film with no voids. Both of these properties of the thin film grown at $250 \text{ }^\circ\text{C}$ contributed to the higher mobility which is the key performance for TFT application.

In the second part of the chapter sapphire was also included as a substrate choice to facilitate the epitaxial growth at higher temperature due to its more lattice matched property with ZnO compared to SiO_2/Si . At $250 \text{ }^\circ\text{C}$ substrate temperature thin films grown on sapphire had higher grain sizes and more than double mobility compared to the one grown on SiO_2/Si substrate. At much higher temperature like $700 \text{ }^\circ\text{C}$ the major crystal orientation changed from (002) to (103). The results indicated that there is a transition temperature between 250°C to 450°C for ZnO thin films grown by PLD after which the growth orientation changed from (002) to (103). More investigation in that temperature gap need to be conducted to find the transition temperature exactly. Grain sizes did not change in a significant amount with the higher growth temperature but more distinct grain boundaries with closely packed grains were observed for higher temperature growths.

Chapter 5

Photoluminescence of ZnO

Photoluminescence of ZnO has been studied for more than fifty years; still there are gaps in the fundamental understanding about its two primary emission bands. One is the near band edge UV emission which is exciton related and the other one is the broad visible spectrum contributed by different defects. This PL emission from ZnO samples can provide information about the quality of the films. This can be used as a characterization tool if the effect of excitation parameters like excitation wave length, pulse duration etc. on the PL spectrum is known. In this section, Time integrated and time resolved PL measurements of a Single crystal ZnO wafer manufactured by MTI by hydrothermal process and Thin Film ZnO samples grown at different growth conditions which are described in Chapter 4 will be discussed. Most of the literatures about ZnO PL use CW He-Cd Laser as an excitation source. In this work, the PL emission of single crystal ZnO wafer was measured with three different excitations sources (CW He-Cd, ns and fs pulsed laser) to compare with the published literature and also the PL emission from Thin film samples of ZnO. Two PLD ZnO samples with different qualities were also investigated using all three excitation sources. The aim of this PL study is to achieve information about the influence of excitation parameters on the radiative efficiency of both near band edge UV emission and visible emissions from defect related states of different quality thin films and single crystal. This information can then be used to study the quality of thin films using PL which is a non-destructive method and does not need any sample preparation. The ns excitation source was used to measure the PL emissions from other thin film samples which were grown in different growth conditions and substrates.

5.1 Time Integrated Photoluminescence (PL)

Time integrated Photoluminescence of ZnO single crystal and PLD samples were measured using a CW He-Cd laser (325 nm), ns pulsed Nd:Yag laser (266 nm) and fs pulsed Ti:Sapphire

laser (266 nm) which provided different numbers of photo generated carriers per unit volume in the samples and different excitation pulse duration for the PL measurements.

5.1.1. Photoluminescence from CW He-Cd Laser Excitation

A CW He-Cd laser was used for the room temperature continuous wave excitation of ZnO samples. This excitation source is the most reported one in the literature. The steady state PL spectrum showed in Fig. 5.1.1 has near band edge UV emission and broad visible emissions from the radiative defects present in the samples which may be bulk or surface related in nature. This shape of PL spectrum using CW excitation is consistent with literature [4, 42].

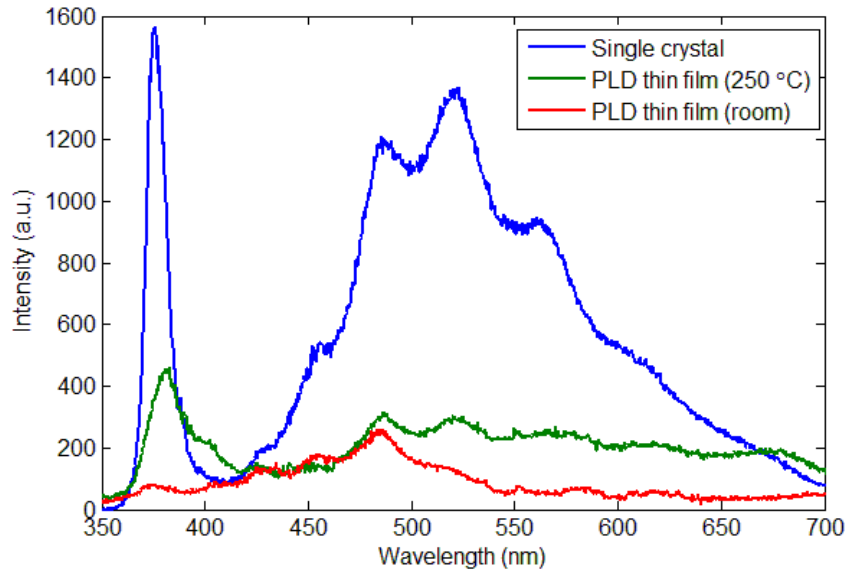


Fig. 5.1.1. CW laser excited PL spectrum of ZnO single crystal and PLD thin films.

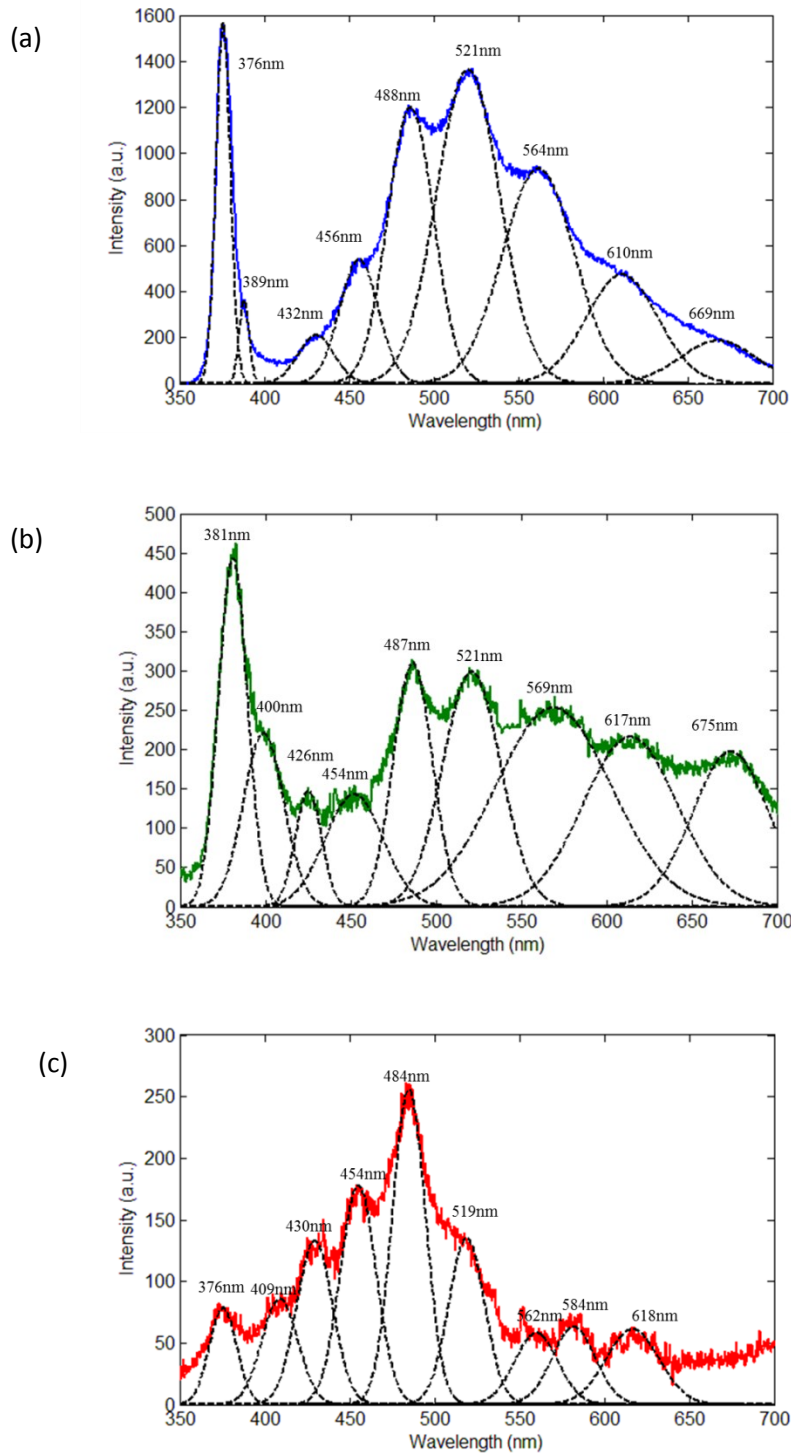


Fig. 5.1.2. CW laser excited PL spectrum of (a) ZnO single crystal, (b) 250 °C grown ZnO PLD and (c) room temperature grown ZnO PLD thin film with Gaussian fit for the PL peaks.

Figure 5.1.1 shows the time integrated PL spectrum of three different ZnO samples. All three samples are showing the near band edge UV emission along with the visible emission which are contributed by different defects [42]. The room temperature PLD sample had the lowest near band edge UV emission and highest visible/ UV emission compared to the other two samples. In order to study different radiative transitions from these samples nine peaks were de-convoluted from the time integrated PL signal using Gaussian fitting. These peaks are shown in Fig. 5.1.2 (a, b, c) for all three samples.

The origins of these visible transitions shown in Figure 5.1.2 are a matter of debate for last two decades. A comparison between the samples PL peaks are summarized in table 5.1.

Table.5.1. Comparison of possible transition and FWHM of the major peaks.

Sample	Peak (nm)	FWHM (nm)	Possible transition	Intensity (a.u)
Single crystal wafer	376	11.1	Free exciton	1564
	389	6.5	2LO phonon assisted	351.8
	432	27	Zn _i to V _{zn}	208.5
	456	28	Zn _i to VB	538
	488	33	CB to unknown acceptor	1193
	521	44	CB to O _i	1361
	564	38	CB to V _o	930
	610	45	Zn _i to O _i	489
	669	51	V _o to valence band	198

ZnO PLD room temperaturesample	376	20	Free exciton	78.5
	409	25	CB to V_{zn}	85.9
	430	23.5	Zn_i to V_{zn}	133
	454	24	Zn_i to VB	176
	484	23	CB to unknown acceptor	256
	519	27	CB to O_i	135
	562	28	CB to V_o	56
	584	30	unknown	61
	618	35	Zn_i to O_i	60
ZnO PLD 250 °C	381	18	Free exciton and LO phonon assisted	443
	400	29	CB to V_{zn}	221
	426	18	Zn_i to V_{zn}	146
	457	38	Zn_i to VB	141
	487	28	CB to unknown acceptor	308
	521	40	CB to O_i	299
	569	83	CB to V_o	267
	617	65	Zn_i to O_i	214
	675	64		196

From this table it is obvious that the room temperature thin film PL sample suffers from less radiative efficiency as compared to the other thin film sample which is grown at 250 °C and shows higher crystal quality and mobility shown in Chapter 4. It had the highest peak at around ~484 nm which is a defect related recombination the origin of which is discussed later in this

chapter. The other (higher temperature) PLD thin film had highest PL emission from the near band edge UV peak but it also exhibited the ~487 nm peak emission as a second highest peak. In the single crystal wafer this 487 nm peak is not as significant as it is in the PL deposited thin films which may indicate that it might be related to some surface defects. The possible origins of these defects are shown in Fig. 5.1.3 in an energy level diagram and discussed below.

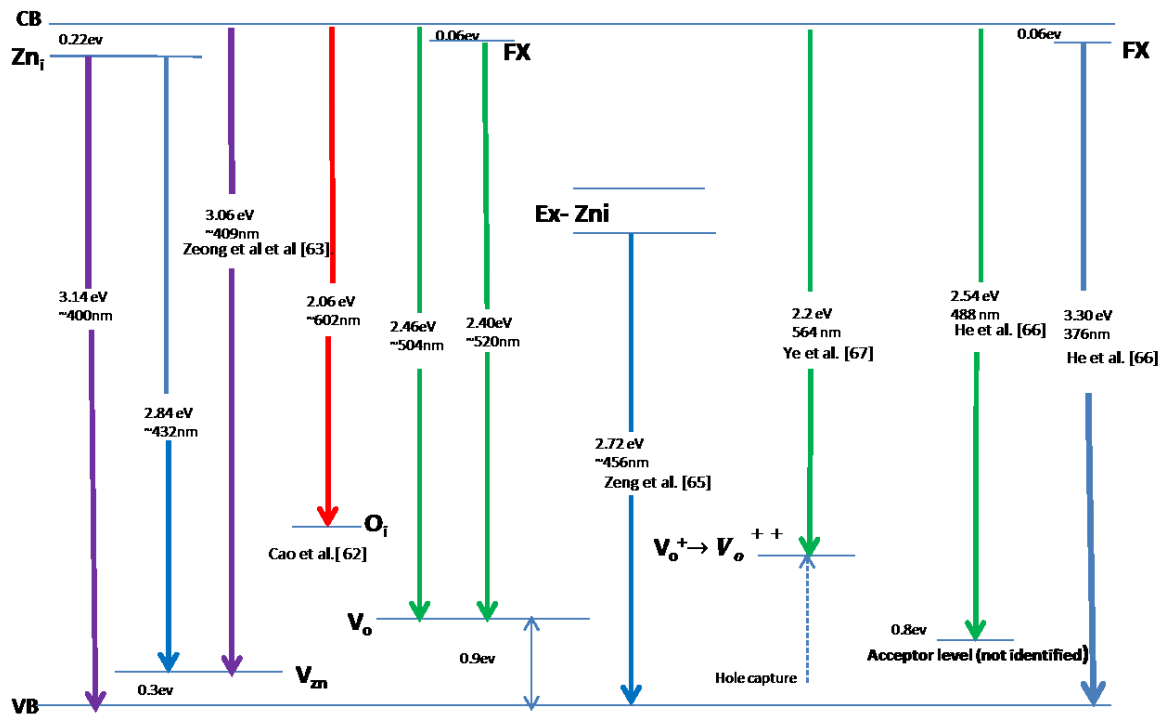


Fig. 5.1.3. Energy level diagram for all possible transitions for CW measurements of the three samples.

The discussion about the possible origins of these defects can be started with the less debatable UV emission. For the bulk ZnO wafer room temperature UV peak was observed at 3.3 eV which is in good agreement with the reported bulk ZnO band gap at 3.36 eV subtracted 0.06 eV for the temperature independent exciton. The UV emission is reported as the free exciton emission where the exciton binding energy is 60 meV. Thus near room temperature it is temperature independent [61]. The UV peak of the room temperature sample has the same peak position which is also 3.3 eV. But for the 250 °C growth temperature sample the peak position shifted to 381 nm which is 3.25 eV which is much closer to the one LO phonon assisted recombination of the free exciton. A composite line shape with a peak value displaced towards longer wavelength

was referred as a phonon assisted recombination by S. Mitra *et. al.* [62]. The UV peak of 250 °C substrate temperature can be well described by [62]. In case of the single crystal wafer there was another minor peak at around 389 nm which aligns well with the 2LO assisted recombination of free excitons.

The energy for LO phonon assisted recombination is equal to the free exciton emission energy minus the energy of the LO phonon (72 meV). Thus this room temperature UV peak can be free exciton emission (FX) or 1/2 LO phonon assisted recombination (FX-1LO, FX-2LO) [61]. The ratio of each recombination and the overall peak position was observed as a function of growth parameters by T. Voss *et. al.* [61] for ZnO nanowires. They also used the 325 nm He-Cd laser as the excitation source. The room temperature PLD sample had the lowest UV emission with a broad peak consisting of contributions from both free exciton and 1 LO phonon assisted recombination. 250 °C growth temperature sample has a much sharper UV peak which also has higher intensity compared to the visible emissions. This 250 °C sample mostly has the 1 LO phonon assisted emissions contribution in its UV peak. This is in agreement with literature where a shift of the UV peak to lower energy caused by the phonon assisted free exciton recombination can be possible due to some surface defects and traps which enhances the free exciton phonon coupling. The largest free exciton emission was observed from the single crystal ZnO wafer which can be compared as bulk sample, it demonstrates less surface defects compared to the thin film samples. This also is in agreement with the literature that surface defects play a major role to enhance the phonon assisted recombination [61].

After near band edge UV emissions the first visible transition which comes next is the violet emission which is centered at around 400 nm (3.14 eV) for the 250 °C sample and 409 nm (3.03eV) for the room temperature sample. The possible origins for the two violet emissions from the thin film samples can be due to a transition from the well accepted Zinc Interstitials (Zn_i) level which is just 0.22 eV below the Conduction Band (CB) to the Valence Band (VB) (400 nm) and from the Conduction Band (CB) to Vacancy of Zinc (V_{zn}) level which is around 0.3 eV above the Valence Band (VB) [63, 64]. The bulk sample did not have any of these violet emissions. This observation may indicate that these emissions get enhanced by the surface related defects which are less in the bulk samples.

After the violet emissions of the thin film samples next in line for discussion are the blue emissions. The 432 nm transition was present for all three samples which might be due to a transition between the Zn_i and V_{zn} states [65]. The common transition was located at around 456 nm for the single crystal wafer and at 454 nm and 457 nm for the room temperature and 250 °C growth temperature samples, respectively. According to existing literatures this blue emissions can be due to the transition between extended Zn_i states to the VB. These extended Zn_i states are slightly below the original Zn_i state and can be created during annealing process. Zeng *et. al.* [66] performed a comprehensive study on the origin of this blue emission in ZnO nanoscale samples. They observed an increase and then a decrease in intensity of this emission with annealing. According to the PL spectrum of the single crystal and thin film samples it was observed that thin film samples had almost same intensity of this emission for the inferior room temperature sample and better 250 °C sample. The single crystal sample had a bit higher intensity but the overall radiative efficiency of this sample is high. If we consider the UV to visible peak (blue) ratio it is quite obvious that as the overall quality of the sample gets better (better crystal structure and less defect density according to electrical measurement) as this ratio becomes bigger.

The green emission starts with the 488 nm emission which is present in all three samples. This emission line is well aligned with a transition from conduction band to He *et. al.* [67] proposed unidentified acceptor level which is 0.8 eV above the valence band. They observed a negative thermal quenching for both excitonic and green emission (near 2.5 eV which is around 488 nm) over a wide range of temperature in pleated ZnO nanosheets. They calculated the activation energies (21 and 32 meV respectively for excitonic and green emission) using the numerical fit of the PL intensity as a function of temperature. This might be due to thermal activation of electrons and their subsequent transition to a deep level acceptor which is at 0.8 eV above the valence band. This emission is higher for the room temperature sample which has inferior surface and very low grain boundaries compared to the other PLD sample grown at 250 °C and the single crystal wafer.

In many existing literatures oxygen vacancies are reported to be responsible for the green emission [3, 10]. The position of Oxygen vacancy is reported around 0.9 eV above the valence band in different literatures. The transition of a free electron from CB to this level can radiate the

504 nm line and free exciton recombination at this level can emit 520 nm. These are present in all three samples. The single crystal sample has the most exciton to V_0 transition as we can observe its superior quality enhances the free exciton emission also.

Due to the low formation enthalpy oxygen vacancies are the most available donors in undoped ZnO. These oxygen vacancies in ZnO can have three possible charge states. The first one is V_0^+ state which is neutral already by capturing two electrons. The single ionize V_0^+ state and V_0^{++} which is doubly positively charged with respect to the lattice. Ye *et. al.* [68] suggested that grain boundary induced depletion region lead to the formation of deeply trapped doubly charged oxygen vacancy (V_0^{++}) which undergoes radiative recombination with CB electron to yield PL of wavelength around 564 nm.

Finally, the red and orange emissions are the least described in literature. The two emissions at around 610 nm and 670 nm for the thin film samples and the wafer were observed. From the work of Studenkin *et. al.* [69] room temperature red PL generally has a relationship with excess oxygen. It was based on various annealing studies in oxygen atmosphere. According to [70, 71, 72] it might be due to the transition between Zn_i to O_i (1.09 eV). There is also another position of V_0 reported which is around 1.65 eV above the valence band. Transition from this band to V_B emits around 700 nm may also be the reason for the red emission from the two samples [72].

Analyzing the different intensities of various PL peaks from CW excited PL emission the surface related defects according to literature are more prominent in thin film samples. The sample with poor structural and electrical properties also exhibited more structural defect emissions (488 nm) /UV ratio compared to the superior thin film samples. PL measurement with CW excitation thus provide information about sample quality and different defect types that are present in different samples.

5.1.2. Photoluminescence from ns Pulsed Laser Excitation

The time integrated room temperature photoluminescence spectra with ns pulsed laser excitation (266 nm) of single crystal ZnO and PLD deposited ZnO thin film are shown in Fig 5.1.4. In this

figure, PL emission from ZnO wafer is integrated for 6 shots. For PLD samples grown at room temperature and under heated conditions, this integration was done over 100 shots.

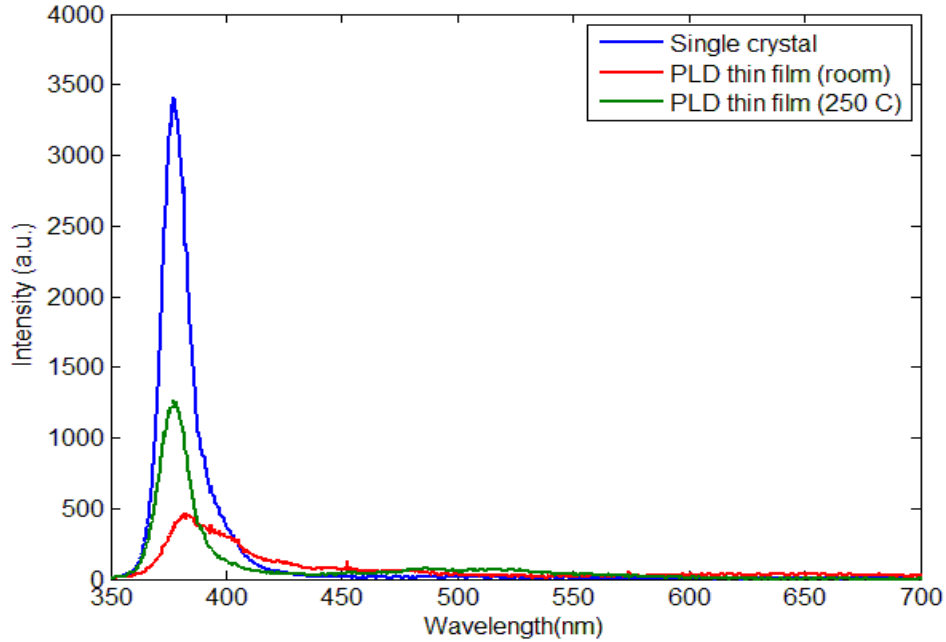


Fig. 5.1.4. Nano-second pulse laser excited PL spectrum of ZnO single crystal and PLD thin film.

The PL spectra from single crystal ZnO wafer and PLD thin film samples grown at room temperature and at 250 °C substrate temperature exhibit a strong dominant near band edge UV emission peak. This Peak was at 377.5 nm for the single crystal ZnO. For the PLD room temperature sample a broad near band edge UV peaks centred at around 380 nm and for the 250 °C substrate temperature sample the near band edge UV peak is at around 377.5 nm which is exactly same as the single crystal sample. This red shift of the UV peak of the room temperature sample may be caused by the strain induced by different defects and also due to the lattice mismatch of the substrate [72].

There are multiple peaks for the PLD samples which contributed in the PL spectrum. Fig. 5.1.5 is showing the peaks using Gaussian fit for all three samples.

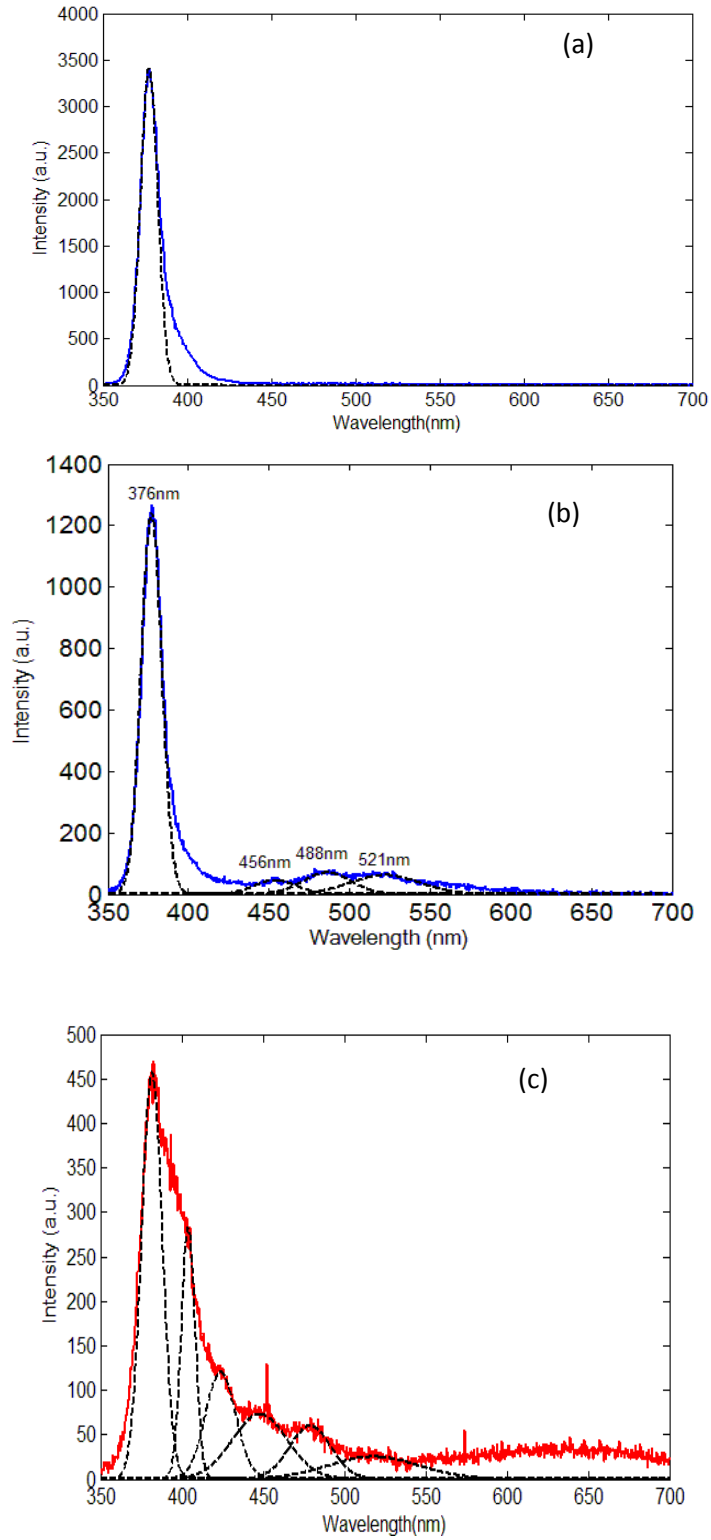


Fig. 5.1.5. Nano-second pulse laser excited PL spectrum of (a) ZnO single crystal, (b) PLD room temperature thin film, and (c) PLD 250 °C substrate temperature thin film.

The origin of these transitions is summarized in an energy level diagram in Figure 5.1.6.

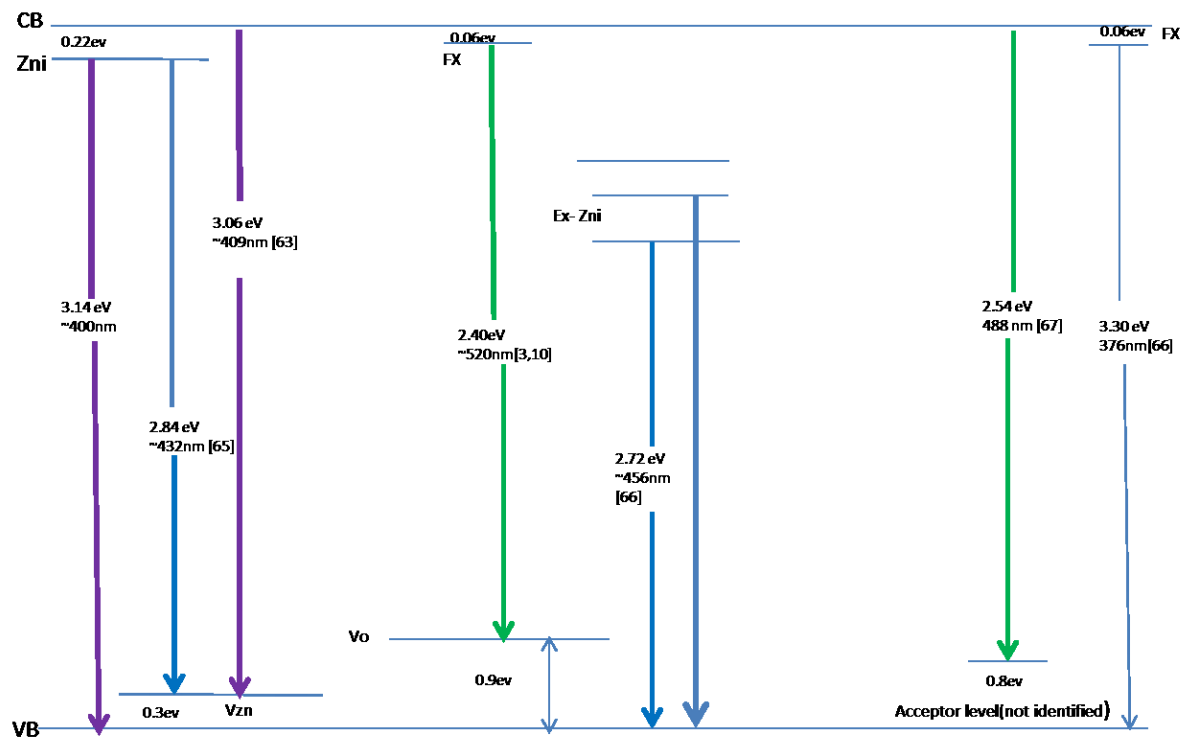


Fig. 5.1.6. Energy level diagram for all possible transitions for ns measurements of the three samples.

As we can observe the defect peaks are only visible for the PLD samples with ns excitations. PLD room temperature film exhibited more variety of defects starting from the violet to the green, In the other hand the 250 °C sample exhibited only 1 blue peak at around 456 nm which is more close to the green emission and mostly green peaks but of very lower intensity. According to the discussions in the previous section with CW excitation the origins are listed according to the existing literature. Oxygen vacancy and unknown acceptor level at 0.8 eV above the VB are might be responsible for the green emissions of the superior PLD sample grown at 250 °C.

The intensity of the UV peak is almost 100 times higher for the single crystal wafer compared to the room temperature sample (as room temperature PL is an accumulation of 100 shots and single crystal wafer is an accumulation of 6 shots). The intensity of the heated growth is also almost seven times more than the room temperature grown sample. In Chapter 4, Fig. 4.1.3 (a) and (d) are SEM images for room temperature PLD sample and heated PLD sample,

respectively. From these images we can observe that the grain size for room temperature sample was 2-4 nm and that the heated PLD sample has a much larger grain size of 20-140 nm. According to existing literature [60], these smaller grain boundaries can cause more non radiative relaxation process and decrease the overall PL efficiency. This may explain the lower radiative efficiency of the room temperature PLD sample and consequently the lower PL emission efficiency can indicate structurally inferior sample quality.

The excitation pulse duration was around 10 ns for the ns excitation. This may be shorter than the capture and relaxation time of many radiative defects present in the samples; thus the radiative efficiencies of those defects become saturated. The steady state PL excitation (CW) provided a more complete picture of the samples true optical properties.

With ns pulse excitation, near band edge UV emission dominated which also can be used to characterize sample quality (in terms of grain size and strain induced by defects and substrate). For UV emitting device application ns excitation may be a good option to enhance the UV emission. However, the weak visible emission makes it less suitable for detailed defect analysis.

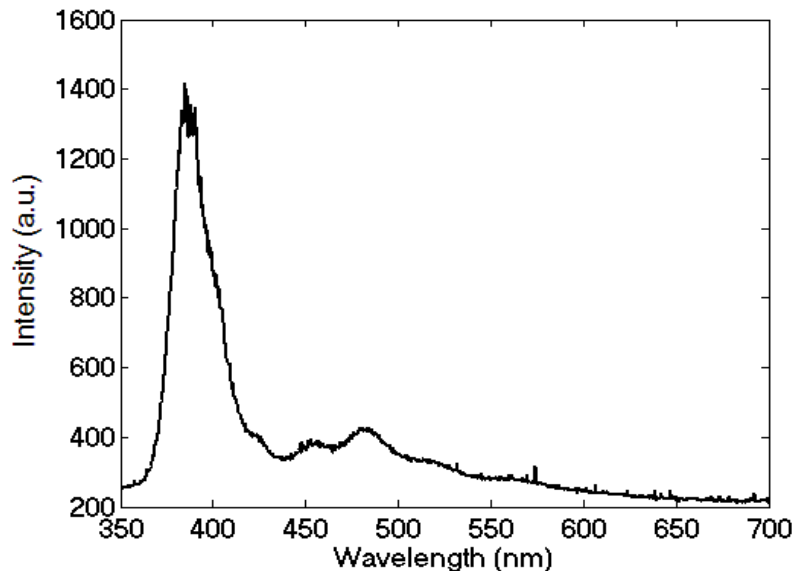


Fig. 5.1.7. Nano-second pulse laser excited PL spectrum of ZnO PLD target.

Figure 5.1.7 shows the PL spectrum of ZnO target used for PLD deposition using ns excitation. It has a UV peak at around 380 nm which is red shifted compared to the single crystal sample

and showing multiple peaks for visible defect emissions which are close to PLD thin film samples.

5.1.3. Photoluminescence from fs Pulsed Laser Excitation

A fs pulsed laser (266 nm) was used as an excitation source to measure the PL spectrums of the above mentioned samples. The time integrated PL spectrums of ZnO single crystal wafer and PLD deposited samples are shown in Fig. 5.1.8.

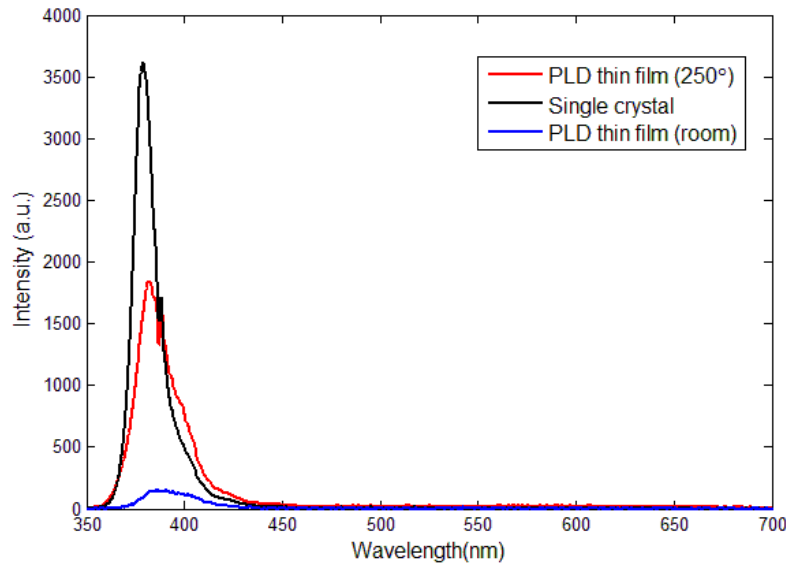


Fig. 5.1.8. Time integrated PL spectra of single crystal ZnO wafer and PLD thin film sample with femtosecond pulsed laser excitation.

The strong near band edge UV emission was observed for all three samples. The single crystal showed a composite UV peak which might be a combination of free exciton emission (377 nm) and a lower tail of phonon assisted emission at (387 nm). The PLD samples had broader UV near band edge emission for both samples which can be de-convoluted and identified as 1 (381nm) and 2 LO (387 nm) assisted emission.

Figure 5.1.9 shows the de-convoluted peaks from the PL emission of three samples using Gaussian fit.

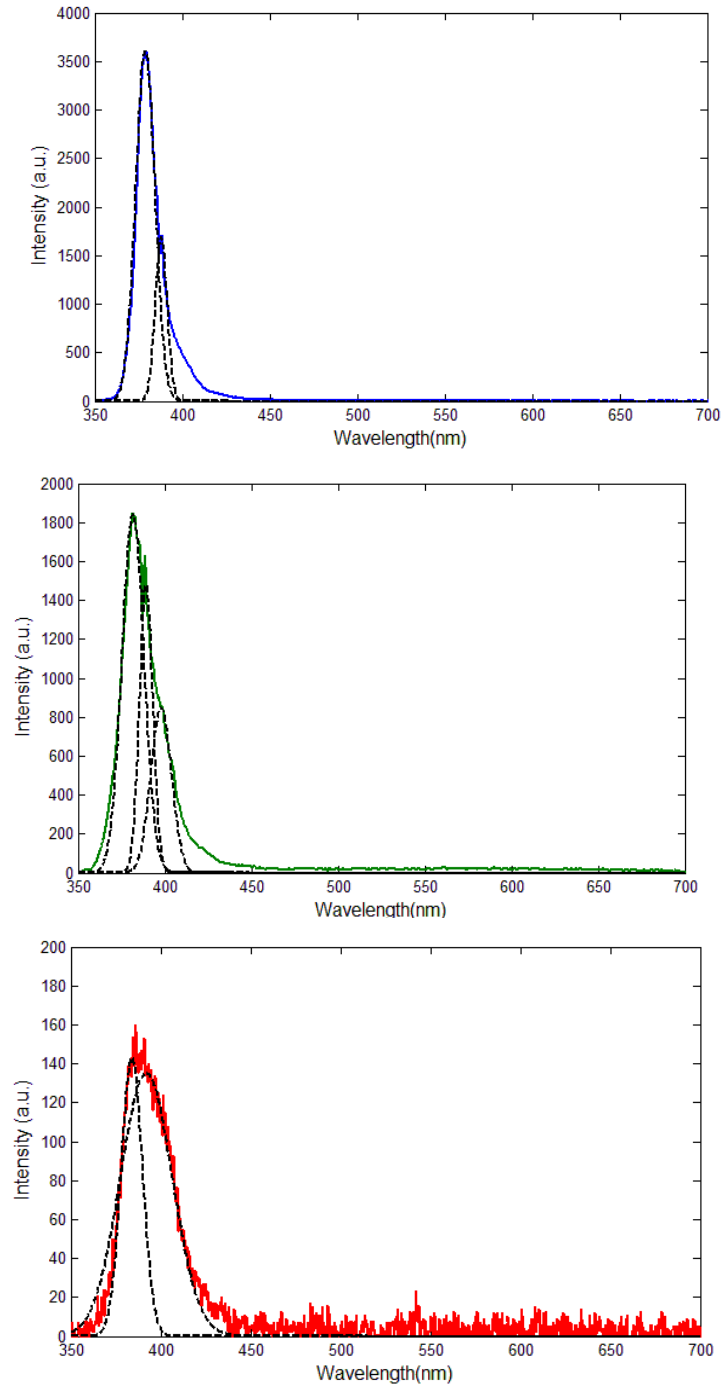


Fig. 5.1.9. Time integrated PL spectra of single crystal ZnO wafer and PLD thin film sample with femtosecond pulsed laser excitation with Gaussian fitted peaks

The three different time duration excitation for the PL emission of three different quality samples correlate with each other in terms of the optical efficiency of the samples. Shorter time scale

excitations may exclude some details of PL spectrum due to the saturation of different defect levels which reduce their emission efficiency. The saturation of a certain defect state with a certain excitation time also indicates the radiative life time of those particular defects. According to existing literature [42], as most of them has a radiative life time in the order of few micro second, ns and fs excitations will saturate most of them which we can also observe from the three different PL excitation plots. Therefore measuring PL with different excitation time can also provide information about the saturated defect states life time.

Using the fs PL measurement also the sample quality can be compared using the ratio of the free exciton emission and LO phonon assisted emission. As it can be observed from this work that higher quality samples have more free exciton emission and less phonon assisted emission which is in agreement with the existing literature [61,62]

5.2. Time-resolved Photoluminescence (TRPL) Measurement of ZnO Samples

Time resolved PL was measured at room temperature for ZnO single crystal wafer and the PLD deposited sample using the 266 nm fs laser described in the experimental techniques. From the time integrated measurements (see Fig. 4.2.3) with the same excitation source, a strong near band edge UV emission was observed. The strong narrow UV peak centered at ~ 380 nm is reported due to the free exciton recombination [68].

For the TRPL measurements, the laser pulse and single crystal signals were accumulated from 100 shots, while PLD film on SiO₂ was accumulated from 200 shots. The PL from single crystal was showing an exponential decay pattern with two different time constants. The values of the time constants are listed in Table 5.2. The TRPL signal from the PLD sample had a similar width as the laser pulse, which was instrumentation limited.

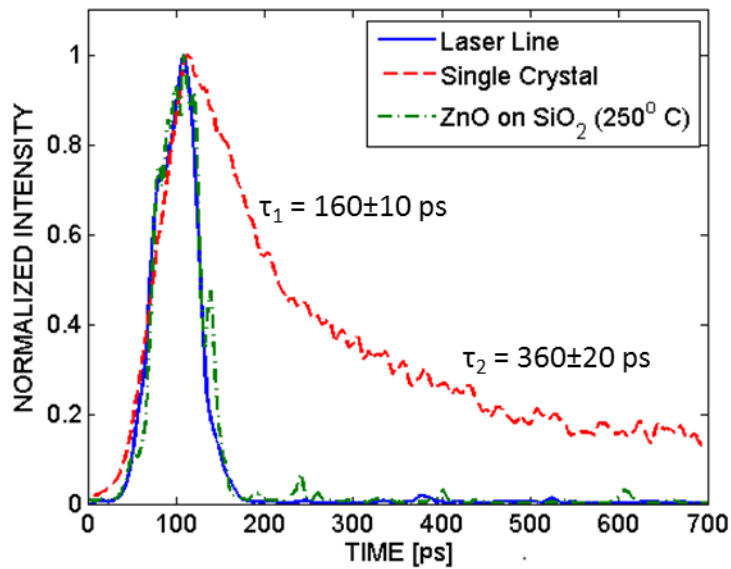


Fig. 5.2.1. Temporal response for the PL spectrums of ZnO single crystal and PLD deposited thin film on SiO₂ substrate.

Fig. 5.2.1 is showing the TRPL measurements of three samples along with the laser line without the fiducial monitor. The detailed experimental set up for the fiducial monitor assisted TRPL measurements is described in Chapter 3. After using the fiducial monitor better time resolution (~15 ps) and improved signal to noise ratio were achieved. TRPL measurements with the new setup are shown in Fig. 5.2.2. From the new measurements, the rise time for the single crystal ZnO wafer was shorter. All measured PL rise times are approximately equal to the temporal response of the system to the laser pulse.

Table 5.2. TRPL measurement Data from ZnO single crystal and PLD deposited thin film.

Sample	Decay time constant (ps) without Fiducial monitor	Decay time constant (ps) with Fiducial monitor
Single crystal (Full PL spectrum)	$\tau_1 = 160 \pm 10, \tau_2 = 360 \pm 20$	$\tau_1 = 140 \pm 10, \tau_2 = 340 \pm 20$
PLD sample	FWHM (ps)	FWHM (ps)
ZnO on sapphire 250 °C	$\cong 50$	$\cong 28$

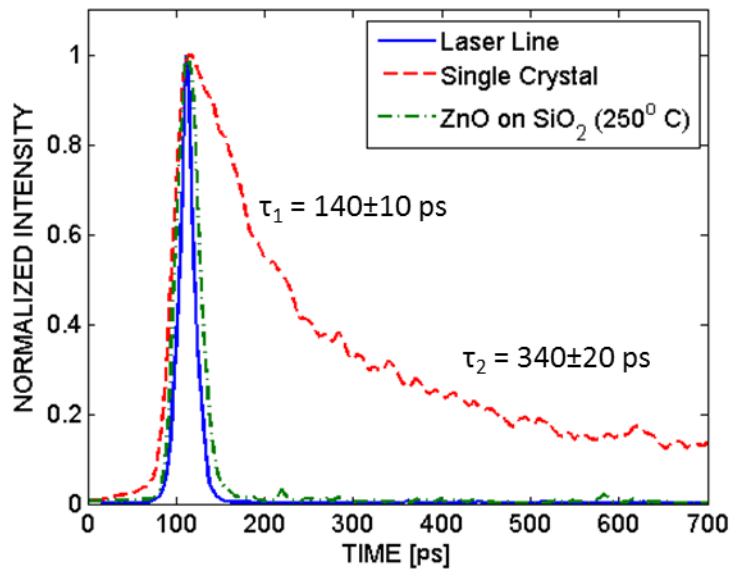


Fig. 5.2.2. Temporal response for the PL spectrums of ZnO single crystal and PLD deposited thin film on SiO₂ substrate with fiducial monitor.

The TRPL signal of the single crystal showed an exponential decay with two different time constants which is similar to the previous measurement (without the fiducial monitor). The decay time components are reasonably close for the measurements with and without fiducial, because they are significantly longer than 15 ps. Detailed calculations of these time constants are given in Appendix.

The double exponential behaviour (140±10 ps for the fast component and 340±20 ps for the slow component) suggests that two different decay processes are involved in the emission although the exact mechanism is not clear at this point.

Existing literature on the decay of TRPL signal of single crystal ZnO shows a bi-exponential decay pattern [59, 60, 76]. Among them, B. Guo *et al.* [76] observed two time constants with 30-50 ps for the fast decay time constant and 100 - 400 ps for the slow decay time constant in their room temperature TRPL study of single crystal ZnO thin films grown by MOCVD. Wilkinson *et al.* [72] measured the room temperature TRPL of a commercially available ZnO single crystal sample and found a fast decay time constant of around 410 ps and a slow decay time constant of around 3.8 ns. Teke *et al.* [77] measured the room temperature TPRL of a commercially available ZnO single crystal sample and found a fast decay time constant of 170 ps

and a slow component of 860 ps. All these different values indicate different qualities of single crystal ZnO grown by different methods. The measured decay time constants in this work lie within the large ranges of the two reported time decay constants. The large ranges reflect that single crystal ZnO samples can be very different from each other. The fast component of the radiative life time is attributed to the free exciton radiative lifetime and the slower component is associated with the free carrier trapping and relaxation process according to the existing literature [76].

The FWHM of the Gaussian signal of the PLD (250 °C) sample was around 30 ps which is still instrumentation limited. From our measurements we can conclude that the TRPL lifetimes for the ZnO thin film samples grown by PLD are much shorter than that of the single crystal ZnO wafer. This may be due to the fact that non-radiative recombination is the dominant one in case of thin film ZnO. There are different non-radiative processes in semiconductor like capture by deep centers, multi phonon emission, Auger effect etc. These processes give rise to a fast relaxation of the excited carriers to lower states from which they can either decay radiatively or relax non-radiatively [60]. Also surface defects, crystalline boundaries, chemical and mechanical defects can serve as scattering sources for excitons which enhance the non-radiative recombination [61]. These non-radiative recombinations reduce the measured lifetime of the radiative decay.

The radiative lifetime measurements for single crystal ZnO and PLD deposited ZnO thin films also clearly indicated the superior quality of the single crystal wafer with larger radiative lifetime. Comparison between PLD samples was not possible using this study due to the instrument resolution even though it was improved from 50 ps to 15 ps using the optical marker. The radiative lifetime of ZnO PLD samples are less than 15 ps which is low compared to the existing literature [59]. This may be due to small film thickness (100 nm) of our PLD samples with smaller grain boundaries which reduce the radiative efficiency.

5.3. Influence of Photoexcitation Density on PL spectrum of ZnO

Different excitation time durations have been used to explore the effect of the initial carrier density on the PL spectrum. The photo generated carrier density can be approximated as [42],

$$\eta_{\text{exc}} = \frac{(I * \alpha * \tau)}{(h * \nu)} \quad (5.1)$$

here, I is the absorbed excitation intensity (calculated using the incident laser power and beam spot area mentioned in chapter 3 for CW, ns and fs laser sources), α is the absorption coefficient of sample at the excitation wavelength ($2 \times 10^5 \text{ cm}^{-1}$), τ is the effective radiative lifetime of the sample (~ 100 ps for single crystal, ~ 10 ps for PLD thin films, and for fs approximation τ is the pulse duration), h is the Plank's constant, and ν is the excitation frequency. To determine the radiative recombination time, we used the streak camera measurements for time resolved photoluminescence measurement. Table 5.3 lists the calculated number of photo generated carriers using equation 5.1 and intrinsic carrier concentrations of the samples using electrical measurements [9, 46] for comparison. For the single crystal commercial sample the intrinsic carrier concentration was taken from the literature [54].

PL spectrums of ZnO samples provide an idea about the radiative defects in the sample. The visible emission of PL is known as defect emission (although the origins of these defects are matter of debate). However, one point to note here is that the PL emission efficiency of a sample depends on the ratio of radiative to non-radiative defects of that sample. If a sample has a higher concentration of non-radiative defects then the relaxation due to non-radiative transition will dominate as most of the free carriers generated by photo excitations will be captured by the non-radiative traps and radiative recombination will be significantly reduced. Electrical measurements give us a value for intrinsic carrier concentrations in the samples which are coming from the native defects of ZnO due to the growth process. Although the nature of these native defects (whether they are radiative or non-radiative) are unknown, they have a correlation with saturation of radiative defects at different photo excited carrier concentration.

A ZnO sample should possess finite densities of non-radiative surface traps and radiative visible emitting defects. If the photo excited carrier concentration is higher than the concentration of certain radiative defects then those defects will be saturated and their radiative efficiency will

drop. Also all these defects have different trapping time over which carriers are trapped and also a different recombination time over which the trapped carriers recombine [42, 60].

It is reported in the literature that defect life time can vary from hundreds of nanosecond to a few microseconds [42]. When a defect state is filled it will try to decay radiatively first before it gets filled again. When the excitation pulse is shorter than the defect radiative life time the efficiency of that particular defect also reduced because it does not get enough time to decay and capture again within that short period of time. In this work the ns (6 ns pulse) and fs (180 fs pulse) have excitation times much smaller than the reported life times of different defects. Therefore only CW excitation enables us to observe the PL emission in true equilibrium.

From our excitation sources parameters and the effective lifetime estimated with the streak camera measurements we calculated the photo generated carrier concentration in different samples with different excitation lasers using equation (5.1).

From Table 5.3 and different PL spectrums, we can see that when the photo generated carrier concentrations are lower or comparable to the intrinsic carrier concentration of the samples PL spectrum also show the defect emission clearly which is the visible part of the PL spectrum.

Table 5.3. Approximated photo carrier concentration and measured intrinsic carrier concentrations [9, 46] of different samples.

Excitation laser	Pulse duration	Sample name	Photo Injected carrier concentration (cm⁻³)	Intrinsic carrier concentration from electrical measurements (cm⁻³)
He-Cd	Continuous Wave	Single crystal ZnO wafer	1.44×10^{13}	4.09×10^{16}
		PLD 250 °C	3.12×10^{12}	5×10^{14}
		PLD room temperature	3.12×10^{12}	8×10^{17}

Nd:Yag	6 ns	Single crystal ZnO wafer	2.95×10^{18}	4.09×10^{16}
		PLD 250 °C	2.95×10^{17}	5×10^{14}
		PLD room temperature	2.95×10^{17}	8×10^{17}
Ti:Sapphire	180 fs	Single crystal ZnO wafer	1.2×10^{22}	4.09×10^{16}
		PLD 250 °C	1.2×10^{22}	5×10^{14}
		PLD room temperature	1.2×10^{22}	8×10^{17}

From the Table 5.3 and Figs. 5.1.1 to 5.1.2, we can observe that for lower photo carrier concentration (in case of CW He-Cd laser) the room temperature sample was mostly showing the defect emissions with a very weak near band edge UV emission. For this sample the intrinsic carrier concentration was in the order of 10^{17} cm^{-3} measured using the C-V measurement [10]. At this photo carrier concentration the radiative defects are not saturated and also the overall radiative efficiency of the film is poor compared to the other samples, which indicates higher non radiative defect concentrations in the sample. For the 250 °C PLD sample which has an intrinsic carrier concentration in the order of 10^{15} also showed defect emissions for the CW excitation. The single crystal ZnO wafer also had both strong UV and defect emissions for the CW excitations. This reflects the facts that its radiative defects are not saturated under this photo injected carrier density (10^{13} to 10^{12} cm^{-3}) and it has a lower non radiative defect concentrations compared to the thin film samples. For thin films samples the non-radiative defects like surface traps and lower grain boundaries are more common compared to a bulk sample like the wafer. Lower non radiative defects in the single crystal wafer were also confirmed from the longer life time measurement using the streak camera compared to the thin film samples.

For the ns excitations, the photo generated carrier concentration is comparable to the intrinsic carrier concentrations for the room temperature sample and higher for the 250 °C PLD sample and single crystal; ZnO wafer. We observed more UV emissions and less defect emissions for

the samples. This indicates the fact that at this photo generated carrier concentration most of the defects are getting saturated depending on their total concentrations.

For fs excitation with a very high photo generated carrier concentration compared to the intrinsic carrier concentration, we observed the near band edge UV emission for all the samples. For the thin film samples the FWHM of the near band edge peak is larger may be due to some defect contribution near the band edge emission.

5.4. Summary

In this study PL excitation of ZnO samples were performed using different excitation density and pulse duration to understand their effect on the PL spectrum. Also the differences between samples PL spectra can provide information about the sample quality so that it can be used as a diagnostic tool for sample quality monitoring.

ZnO samples typically possess n type conductivity with a carrier concentration of $10^{16} - 10^{19} \text{ cm}^{-3}$. When a sample is excited with a carrier density lower than its inherent carrier density the distribution of free carriers will follow the equilibrium distribution of the carriers. Therefore in case of lower excitation density the initial carrier distribution largely influences the optical response of the sample. In this work, the CW excitation was the only excitation method where the excitation density was significantly lower than the inherent carrier concentration of all the samples measured electronically. So CW excitation can provide the PL measurement in a true equilibrium. Thus most defect emissions are visible with this excitation. For determining the defect densities of a sample various excitation densities can be used and the excitation density at which different defects are saturated can indicate that defect density in the sample.

The fs and ns excitations had higher excitation densities compared to the inherited defect densities of our samples thus free exciton related emissions dominated the PL spectrum in these cases mostly.

In a ZnO sample there should be finite densities of non-radiative surface traps, non-radiative bulk traps, and radiative defects for green or blue emissions. All these have different trapping times over which carriers are trapped and also distinct recombination times over which the trapped carriers recombine. If the excitation condition provides a higher carrier photo generation

rate than the trapping and recombination rate of these traps, then the corresponding recombination efficiency reduces. This also plays an important role for lower defect emission efficiency in the case of ns and fs excitation. Though in fs excitation we observed violet emission from the room temperature sample.

All these results contribute to the understanding that (i) All three excitation methods showed the difference between sample qualities. So PL can be used as a diagnostic tool for thin film quality monitoring, (ii) at a particular photo carrier concentration, some radiative defect (especially green emissions) states get saturated and their radiative efficiency decreases, (ii) the photo carrier concentration can thus indicate the particular defect concentration of the sample, (iii) assessment of the radiative efficiency of different samples must be done under similar photo-carrier concentrations in the linear absorption region (iv) lower excitation densities in longer time scale will provide a true picture of the optical response of a sample and (v) to improve the UV emission efficiency of a sample, we need to excite it with higher excitation density in a shorter time scale.

Chapter 6

GaAs Nano crystalline thin films

6.1. Motivation

Si and GaAs are both important semiconductors used extensively in electronic devices. While Si is the backbone material of the present electronic industry, GaAs, a direct band gap III-V semiconductor, is a well-established candidate for photovoltaic devices, laser diodes, light emitting diodes and many other optical and electrical devices. Researchers have been trying to integrate these two materials together for the last three decades. The established method for growing epitaxial GaAs thin films are molecular beam epitaxy (MBE) and metal organic chemical vapour deposition (MOCVD). High quality materials are needed for device application. In order to get good quality GaAs thin films grown on Si, these epitaxial growth methods need to overcome several major challenges. First of all a very high density of dislocations are introduced in the interface as a result of the high lattice mismatch (4% for Si), stress and cracking problems originate from the large mismatch in thermal expansion coefficient. Finally as Si is a non polar semiconductor and GaAs is a polar semiconductor, the growth of GaAs on Si leads to high density antiphase domain formations [78]. The GaAs films on Si achieved by these techniques typically have high density of defects [78, 79] but the very high operation cost of these epitaxial growth methods limit the number of extensive studies for optimizing the growth parameters. Other common methods such as sputtering and thermal evaporation are also used to deposit GaAs on Si [80, 81]. Films deposited by sputtering and evaporation are generally polycrystalline or amorphous [80, 81]. Epitaxial lift-off is a multi-step method for depositing GaAs on Si [82]. In epitaxial lift-off, GaAs single crystal thin films are grown on a lattice matched substrate (e.g. GaAs wafer) with a buffer layer of Aluminium Arsenide (AlAs). The buffer layer is then etched off and the film can be transferred to the Si substrate [82].

PLD is being considered to be an attractive method for depositing compound structures for the last three decades [83]. In PLD, high energy ions are produced by laser-target interaction which leads to many advantages commonly found in ion assisted deposition [83]. The presence of high energy ions in PLD is reported to help achieving epitaxial growth of GaAs on NaCl at relative low substrate temperature [84]. The relatively low substrate temperature is particularly required for deposition on substrate materials which have a different thermal expansion from the target material.

PLD has been investigated for the deposition of III-V semiconductors on a variety of substrates by many research groups for the last three decades. According to our knowledge, the first successful heteroepitaxial growth of GaAs on NaCl using PLD was reported by Sheftal *et. al.* [84] in 1981. The epitaxial growth of several III-V semiconductors on a variety of substrates using PLD was reported by Budyanu *et. al.* [85] in 1985. Several studies of amorphous GaAs thin films on Si substrate deposited by PLD were recently reported by Ulrich *et. al.* [86-89] and the focus of these studies were to demonstrate that these films can be used for device application.

GaAs is different than other compound semiconductors for a preferential evaporation of Arsenic. In more conventional growth process like MBE a higher Arsenic flux is used at higher temperature. So far most of the reported PLD GaAs thin films are nearly 1:1 in ratio for Ga and As. Though a variety of PLD process parameters make it difficult to conclude from the reported literature.

In order to investigate the film composition, structural and morphological properties of GaAs thin films on Si substrate, growth temperatures were varied from room (25 °C) to 600 °C. Si was the substrate choice for optimization of growth parameters for its availability and also the potential electronic device application of GaAs/Si heterojunction.

6.2. Experimental Setup

The PLD setup used for this study is same as described in chapter 3. A rotating n-type single crystal GaAs target was used. The target was at 45 degrees with respect to the laser beam and the substrates were placed parallel to the target for the depositions. The pressure of the chamber was 2×10^{-5} Torr during the deposition and the substrate-to-target distance was 5 cm for all the growths. The laser fluence on the surface of the GaAs target was in a range of 2-3 J.cm⁻².

All the substrates were first etched with $\text{H}_2\text{SO}_4:\text{H}_2\text{O}_2 = 3:1$ to remove organic residues and were then wet etched with $\text{HF}:\text{H}_2\text{O} = 1:10$ to remove the native oxide. The typical thickness of the GaAs thin films deposited was 200 nm. The substrate temperature was varied from room temperature (25 °C) to 600 °C using the conductive substrate heater described in Chapter 3.

XRD patterns of all the thin films were measured using Rigaku X-ray diffractometer (Cu-K α radiation, $\lambda = 1.5405 \text{ \AA}$) to get information about the crystal structure of the films. The XRD measurements were done at a 0.3° glancing angle. The XRD peak positions gave information about crystal orientations. The increase in the x-ray peak heights reflected the improvement of the crystalline quality of the deposited films. AFM was done using Veeco DI 3100 using contact mode. SEM of the samples was carried out using JOEL JAMP-9500F. From both AFM and SEM measurements the crystal sizes were determined and from AFM measurement the roughness of the films were obtained.

6.3. Results

6.3.1. Structural Properties of GaAs Thin Films on Si

The crystalline quality of thin film GaAs on Si deposited by PLD at various substrate temperatures was studied using glancing angle XRD, Fig. 6.3.1 shows the plots of XRD spectra for samples grown at different substrate temperatures ($T_s = 25 \text{ °C}$, 285 °C , 500 °C and 600 °C). It can be observed that nanocrystalline films were achieved even in room temperature deposition. The main peak is positioned at about 27.5° corresponding to the diffraction from the GaAs (111) plane with other two weak peaks at 45.25° and 53.65° which correspond to (220) and (311) planes respectively. There are also five other very weak peaks from other crystal planes of GaAs for all the samples. The intensity of the main peak which corresponds to GaAs (111) is the highest for all the samples which reflects the fact that majority of the crystals are oriented in this direction. This indicates that GaAs thin films with (111) preferred orientation can be obtained on Si using PLD from room temperature to 600 °C. Near $T_s = 285 \text{ °C}$, enhanced intensity and reduced FWHM (from 7° to 1.45°) of XRD peaks were observed which indicate better crystalline quality of the films. Existing literature shows that amorphous GaAs films grown by other methods also tend to crystallize around this temperature [92, 93] during thermal annealing process. At higher growth temperatures ($T_s \geq 500 \text{ °C}$) the FWHM reduced significantly to a

value of 0.8° for $T_s = 500^\circ\text{C}$ and to an even smaller value of 0.05° for $T_s = 600^\circ\text{C}$. At $T_s = 600^\circ\text{C}$, increased intensity of the (111) peak and decreased intensity of other peaks were observed simultaneously.

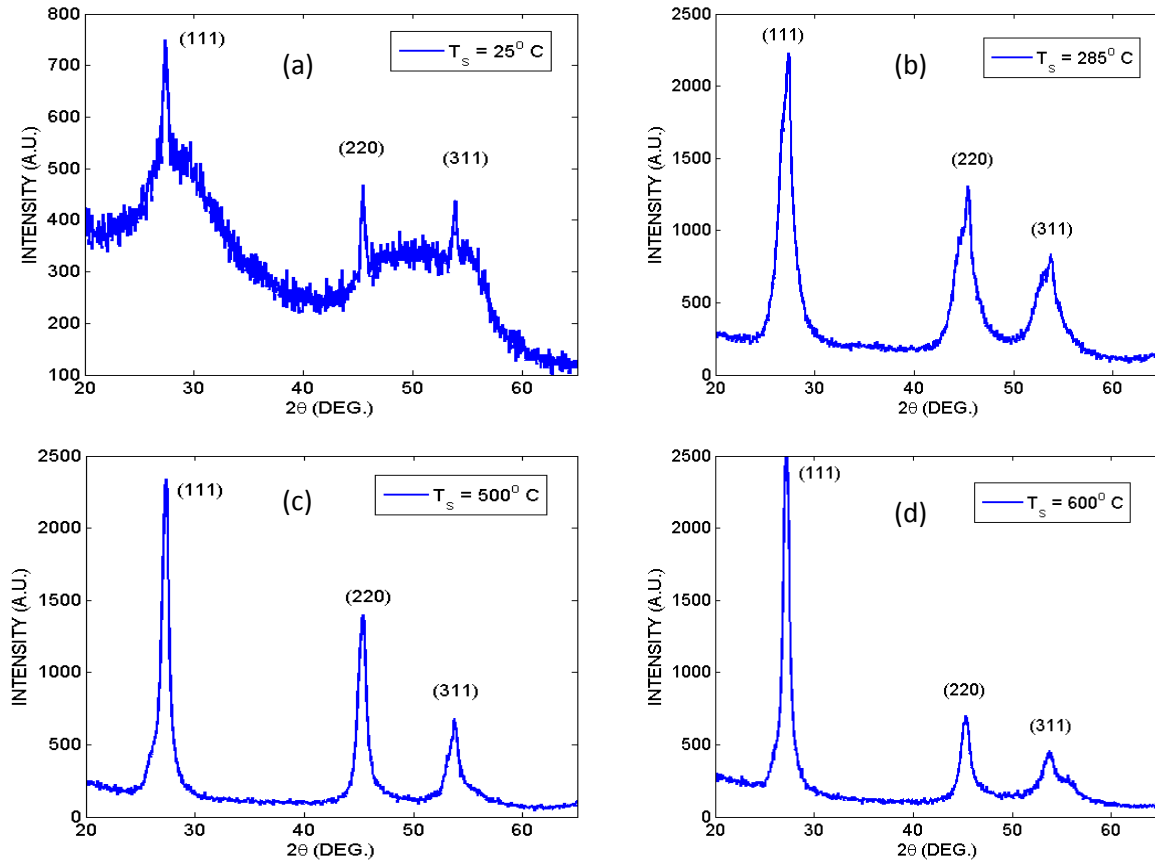


Figure 6.3.1. XRD spectra of GaAs thin films grown at (a) room temperature, (b) 285°C , (c) 500°C , and (d) 600°C .

Fig. 6.3.2 shows the increased intensity of (111) oriented peak as compared to the other two weak peaks for higher substrate temperature indicating films deposited at higher substrate temperatures (above 500°C) are more (111) plane oriented compared to those deposited at the lower substrate temperatures.

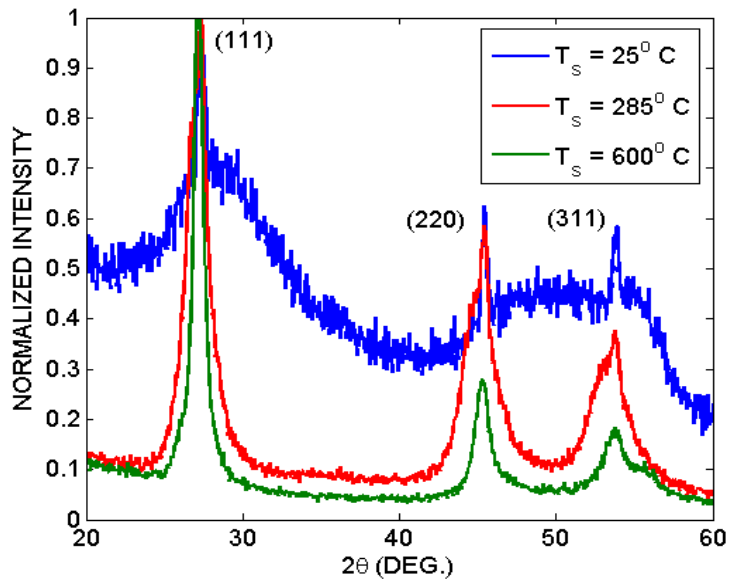


Figure 6.3.2. XRD spectrum shows that at higher temperature ($T_s \geq 500^\circ\text{C}$), the relative intensity of (111) peak increased significantly compared to other peaks.

Figure 6.3.3 shows AFM images of GaAs thin films on Si deposited at $T_s = 285^\circ\text{C}$ and at $T_s = 600^\circ\text{C}$. Uniform distribution of crystal grains with no pinholes or cracks can be observed from the images.

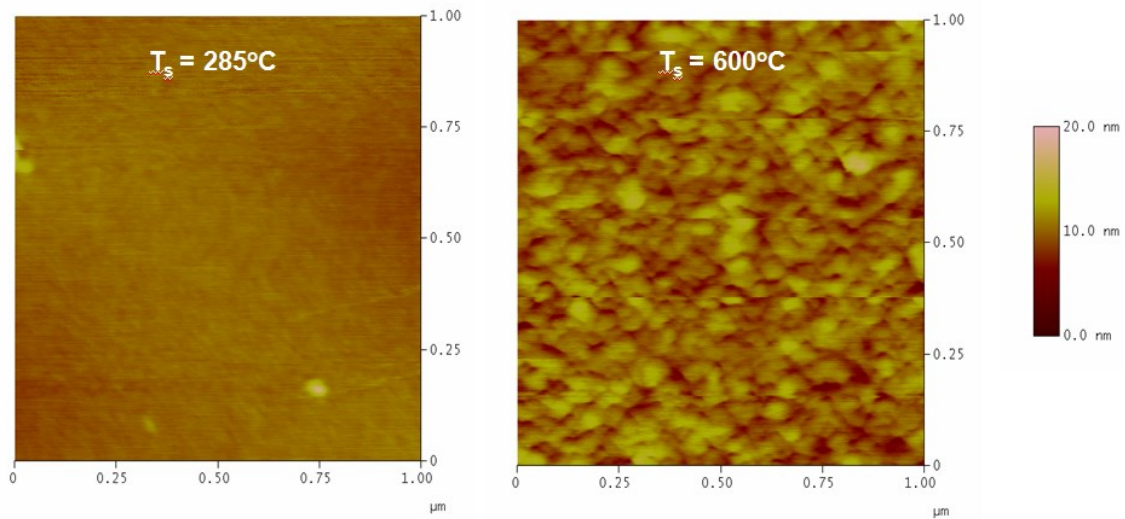


Figure 6.3.3. AFM images of GaAs thin films.

The crystal grain size and roughness of the films were measured from these AFM images. When the substrate was not heated ($T_S \approx 25\text{ }^\circ\text{C}$) the nanocrystalline nature of the film was revealed by XRD but the crystal grain size was too small to be measured by AFM. At a higher substrate temperature of $285\text{ }^\circ\text{C}$ crystal grain size was measured to be 17 nm and at an even higher substrate temperature of $600\text{ }^\circ\text{C}$, the crystal grain size was measured to be 68 nm . The increment in crystal grain size did not lead to significant increment in film roughness. For room temperature growth, the root-mean-square (rms) roughness was measured to be 0.9 nm . At a higher substrate temperature of $285\text{ }^\circ\text{C}$, a slightly increases rms roughness of 1.1 nm was measured and at an even higher substrate temperature of $600\text{ }^\circ\text{C}$, an rms roughness of 1.5 nm was measured. The increment in rms roughness may be related to the increment in crystal grain size at higher temperatures. Surface roughness and crystal grain sizes are summarized in Table 6.1.

Table 6.1. The crystal grain size and surface roughness measurements of GaAs thin films from AFM for different growth temperatures.

Growth temperature ($^\circ\text{C}$)	Grain Size (nm)	Roughness (nm)
Room (25)	Could not be measured	0.9
285	17	1.1
500	38	1.4
600	70	1.5

SEM images were also taken of these films and crystal grain sizes deduced from SEM and AFM images corroborated with each other giving confidence of both results. For example, SEM and AFM images of GaAs thin film deposited at $T_S=500\text{ }^\circ\text{C}$ is shown in Fig 6.3.4. As indicated in Table 6.1, the crystal grain size for the film grown at $500\text{ }^\circ\text{C}$ was deduced to be 38 nm from the AFM measurement while the crystal grain size for the film was deduced to have a similar value of 40 nm from the SEM measurement.

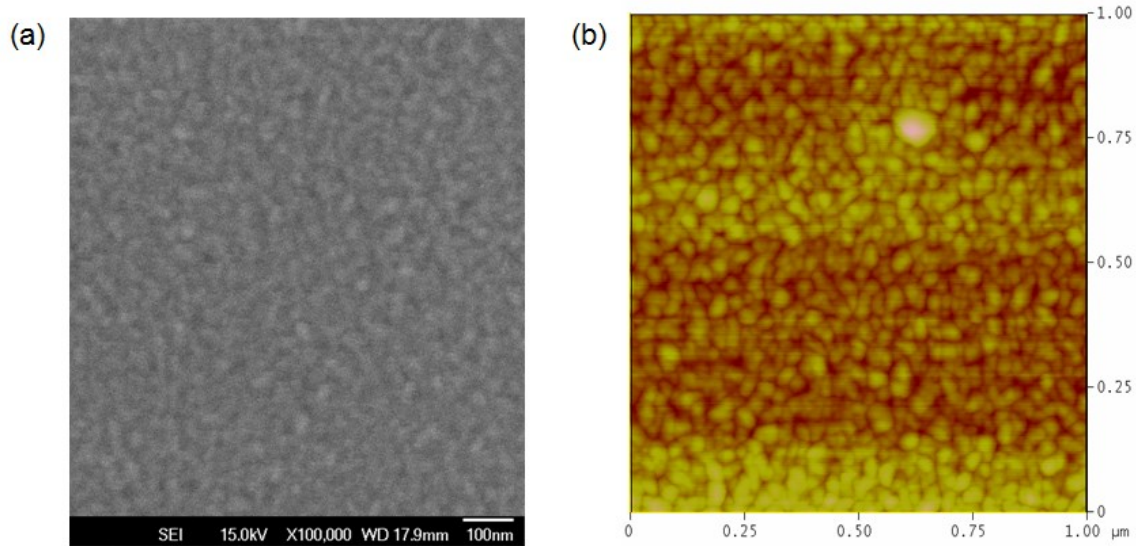


Figure 6.3.4. (a) SEM and (b) AFM images of GaAs thin films on Si at $T_S = 500\text{ }^\circ\text{C}$

The plot of crystal grain size versus substrate temperature is shown in Fig 6.3.5. The crystal grain size data plotted was deduced from AFM images. The crystal grain size increases as a slower rate with temperature for substrate temperatures below $500\text{ }^\circ\text{C}$ but the rate picks up sharply above $500\text{ }^\circ\text{C}$. No saturation in grain size was observed for substrate temperatures up to $600\text{ }^\circ\text{C}$.

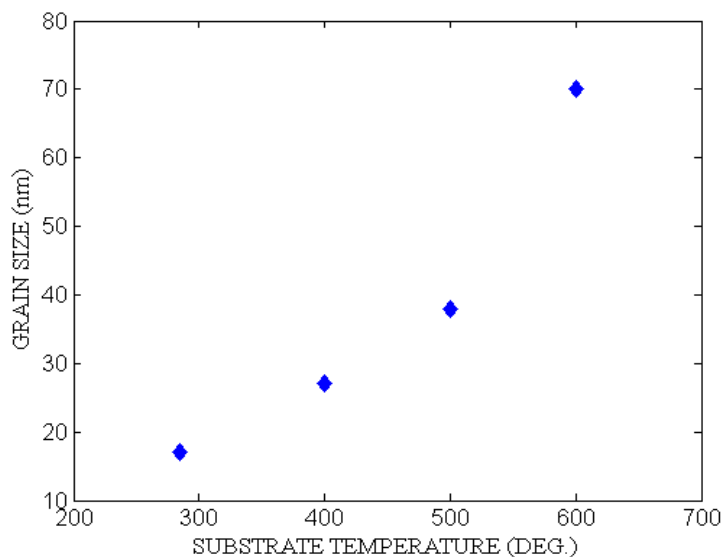


Figure 6.3.5. Change in Grain size with growth temperature

EDS study of the films indicated that at room temperature the Ga and As ratio was almost 1:1 but at higher temperatures the films became slightly Arsenic deficient (1:0.9).

6.3.2. Photoluminescence Measurement

Photoluminescence measurement were attempted both at room temperature and at liquid nitrogen temperature (-195.79 °C or 77 K) using a 20 mW CW diode laser (790.5 nm or 1.57 eV) which is well above the energy gap of bulk GaAs (1.424 eV at 300 K). The PL set up was similar to Fig. 3.4.2 of Chapter 3 only the excitation laser was switched to this diode laser and it was focused to a circular spot of around 2 mm diameter.

Unfortunately no emission was observed from the thin film samples both at room temperature and liquid nitrogen temperature. A commercial wafer of GaAs had its emission line at 870 nm.

The absence of the PL emission indicates a high density of defects present in the films due to compositional or structural issues. The EDS data showed lower Arsenic ratio which may contribute to the poor optical performances of the films at higher temperature on the other hand films produced at room temperature had smaller grains and may contained more structural defects. PL measurement was also tried with a 800 nm femtosecond laser in Prof. Hegman's lab (Department of Physics, University of Alberta) but no emission was observed as well.

6.4. Summary

The structural and morphological properties of GaAs thin films grown on Si substrate over a wide range of substrate temperature from 25 °C to 600 °C by PLD using a KrF laser delivered a range of fluences of 2–3 J.cm⁻² were investigated. In spite of the large lattice mismatch of 4% between GaAs and Si, nanocrystalline GaAs thin films on Si were successfully deposited. From the results we conclude that PLD deposited GaAs thin films are nanocrystalline even when the Si substrate is kept at room temperature. The nanocrystals in the GaAs films are oriented mainly along (111) direction. The intensity of the (111) peak observed in XRD analysis increases and its FWHM decreases with increasing substrate temperature. The crystalline quality improves at a substrate temperature of 285 °C and above. For substrate temperatures greater than 285 °C, uniformly distributed crystal grains form with no pinholes or cracks. For an order of magnitude

increase in crystal grain size, the increase in surface roughness is marginal (from 1 nm to 1.5 nm).

As my main objective was making optical quality thin films Arsenic deficiency at higher growth temperature reduces the motivation to continue this project. Using an Arsenic flux during the growth may reduce this problem but then the simple vacuum chamber should be replaced with a load locked system where growth the chamber will be isolated due to the presence of extra Arsenic.

Chapter 7

Conclusion

7.1. Summary of Present Work

Optical and electrical properties of ZnO thin films need to be optimized for electronic and optical device applications. Electronic device like thin film transistor application requires high mobility and carrier concentration in a range to create desired Schottky contacts with metals. Optical device requires higher radiative efficiency which requires lower non radiative defect concentration. Both of these devices requirement can be fulfilled with high quality crystalline ZnO with lower growth defects. Pulsed laser deposition was used to deposit highly c-axis oriented ZnO thin films of 50 - 200 nm thickness. In order to optimize the required device properties growth parameters like oxygen partial pressure, Laser fluence, substrate temperature, post growth annealing temperature were varied to study their effect on the PLD ZnO thin film mobility, carrier concentration and UV emission properties. Photo luminescence measurements with different quality samples were also performed to compare the optical emission properties and the effect of excitation parameters on the emitted spectrum (both visible defect and near band edge UV) were investigated to understand their effect.

7.1.1. Growth Parameter optimization

In order to be a suitable candidate for TFT application mobility and carrier concentration were optimized for 50 nm thin films deposited by PLD by varying growth parameters. Chapter 4 has described in detail the growth parameter optimization.

Room temperature PLD grown thin films had very small grains and poor crystal orientation. After the annealing (600 °C) the grain size improved almost 10 times and the crystal orientation

was also improved by the high thermal energy but voids and defects due to growth conditions still kept the mobility in the very low range $0.1 \text{ cm}^2\text{V}^{-1}\text{s}^{-1}$. At $250 \text{ }^\circ\text{C}$ substrate temperature the thin films had mostly (002) orientation which is also known as C-axis orientation and grain size improved to 100 nm . Mobility improved almost 100 times and the carrier concentration were reduced from 10^{18} cm^{-3} to 10^{15} cm^{-3} . The low carrier concentration indicates low defect/trap concentration which is a significant advantage for TFT's. Using these films successful TFTs were fabricated by our collaborators from the Nano electronics lab of U of A [10].

Good crystal quality and less structural defects can improve the mobility. In order to improve the grain size and more crystal orientation along the (002) crystal orientation substrate temperatures were varied from room to $700 \text{ }^\circ\text{C}$ and sapphire was used as a substrate along with SiO_2/Si substrate. At growth temperature higher than $250 \text{ }^\circ\text{C}$ it was observed that the growth mode changed and more (103) orientation were present as the substrate temperature was increased to $450 \text{ }^\circ\text{C}$. As discussed in Chapter 4 this growth mode change might be a way to consume the excess energy of the ad atoms gained from the laser generated ions and high substrate temperature. This growth mode has higher formation energy than the c-axis oriented growth.

Sapphire substrate grown films had larger grain size and more distinct grain boundaries compared to the SiO_2/Si substrate. This also indicate that the more close lattice matching substrate sapphire facilitate the larger grain boundaries which might contribute to enhance the higher mobility. The Sapphire substrate grown samples exhibited higher mobility ($16 \text{ cm}^2\text{V}^{-1}\text{s}^{-1}$) compared to the ones grown on SiO_2/Si substrate with the same growth parameters ($8 \text{ cm}^2\text{V}^{-1}\text{s}^{-1}$) in Hall measurements.

7.1.2. Photo Luminescence measurement

Photoluminescence study can provide a lot of information not only about the optical emission efficiency but also the presence of different defect states between the valence and conduction bands of ZnO samples. The excitation time of the PL measurement plays an important role on the emission spectrum. Depending on the initial carrier concentration, the emission efficiency of different defects and free excitons can vary. Depending on the device requirements, initial carrier concentration can be controlled for higher UV or green band luminescence. CW excitation with excitation density lower than the native defect density (measured by electrical measurements) of

the samples can provide a true optical response of the sample. The ns and fs excitations provided high to very high excitation density for the ZnO samples so the free excitons generated due to photo-injection played a major role part in the PL emission. Also shorter excitation time compared to the trapping and recombination time of different defects can cause saturation of those defects. Therefore, in order to obtain detailed information about different defect emissions of ZnO, one has to use an excitation density lower than the native defects with a longer time duration (in the order of microsecond), preferably using a CW source. A comprehensive study of the excitation time effect on PL emission has been performed and summarized in Chapter 5.

Using electrical measurements, one can obtain overall determination of the native defect concentration of a thin film sample but PL measurements can be used to obtain the information about defect types more specifically using the emission wave length and their corresponding energy state values. Different quality samples exhibited different emission intensity or absence of some defect level emissions. Single crystal ZnO wafer which was used as a reference for bulk ZnO showed superior exciton emission efficiency compared to the thin film samples which is expected. Among the thin film samples, the 250 °C substrate temperature thin film showed more near band edge UV emission compared to the room temperature sample in all three types of excitation (CW, ns, fs) measurements. Also the room temperature samples exhibit more visible emission compared to the superior crystalline quality and less defect concentration thin film with all three types of measurement. Thus with any excitation type the difference between the poor and superior quality thin films can be observed using the PL measurement.

With different excitation time (CW, ns and fs) photo generated carrier concentration were varied. Radiative defects of different energy levels were saturated at different photo carrier concentrations for different quality samples. For CW excitation the photo generated carrier concentration was in the low regime (10^{12} cm^{-3}). With this excitation more defect emissions were observed from all three samples. This measurement can provide a complete picture of the samples optical response. Also comparing the intensity of different emissions of the same sample can provide an idea about which radiative defect is higher in that sample. For example, 488 nm transitions might be related to surface defects according to literature which is present in both thin film samples but not in the bulk wafer. Also room temperature sample has higher intensity for

488 nm emission indicating higher surface defects which is possible with lower grain boundaries present in the room temperature samples observed by SEM..

For ns measurements the photo generated carrier concentration was 10^{18} cm^{-3} . In this regime the exciton emission efficiency were increased for all the samples. But room temperature samples the UV emission peak were red shifted compared to the higher quality 250 °C substrate temperature samples. This red shift is described as phonon assisted recombination and indicate poor film quality. Also the room temperature sample had shown more defect states than the 250 °C sample.

For fs measurements the photo generated carrier concentrations, were 10^{22} cm^{-3} . In this regime near band edge UV emission was accompanied by a violet emission for all three samples. But the ratio between UV to Violet is almost 1 for the room temperature sample where as 250 °C has a higher UV to violet ratio and Single crystal ZnO has even higher UV to violet ratio.

With different photo generated carrier concentrations it was also observed for all three samples that with higher photo generated carrier concentration some defect states get saturated and their radiation efficiency decreased. So there can be a saturation threshold for particular defect which can give an indication of the defect concentration in the sample without electrical measurements. To compare sample quality, we should excite all the samples at the same photo carrier concentrations which make it difficult to compare results between groups who are using different excitation sources with different photo generated carrier concentrations. Also radiative efficiency of different defects can be decreased if the excitation source has time duration less than the life time of those defects.

Photoluminescence lifetimes of different PL components were measured in the picosecond range by TRPL measurements. Instrument resolution was improved from 50 ps to 15 ps by using the excitation laser as an optical marker. For multiple shot accumulations, this technique can be used to get better time resolution by reducing the electrical jitter. However, the decay lifetimes of the PLD thin films are still close to instrument resolutions. It is reported that the presence of various defects makes the PL lifetime shorter. The measured PLD grown samples were fabricated on SiO₂/Si substrate at 25 °C and 250 °C. They showed FWHM of ~ 30 ps for its Gaussian pulse shape. This short decay time may be due to the smaller grain size of the thin film

sample and also due to the presence of more defects in it which can contribute as non-radiative traps. This is consistent with the time integrated ns and fs PL measurements where we observed lower PL intensity from the thin film sample as the non-radiative recombination's can reduce the PL intensity. The single crystal ZnO wafer had bi exponential decay behaviour of the life time. The double exponential behaviour (140 ps for the fast component and 340 ps for the slow component) suggests that two different decay processes are involved in the emission which are consistent with others observations. B. Guo et al [76] also observed the bi exponential decay from their TRPL measurement of ZnO single crystal which they suggested as the free exciton emission (fast decay) and defect assisted emission (slower decay). The slower decay component of TRPL measurement done in this project can be due to the phonon assisted recombination's described in Chapter 5.

7.2. Proposed Future Work

A natural extension of this work would be an optimization study on the substrate materials for different application demand. Lowest substrate temperature study can be done by optimizing fluence and oxygen partial pressure to achieve excellent ZnO films on flexible substrates. A two layer growth method with a buffer layer deposition of ZnO can enhance the film properties. This can also be considered for amorphous or large lattice mismatched substrates.

Effect of thickness of the film on its properties can be investigated to obtain information whether there is a critical thickness for preferred orientation of ZnO by PLD or not. Also, how the grain sizes change with film thickness and their effect on mobility or carrier lifetime can indicate optimum thickness for different applications.

Preliminary measurements were conducted using the Raman set up described in Chapter 3 for the single crystal ZnO wafer manufactured by MTI.

Fig. 7.2.1 shows the Raman spectrum of the single crystal ZnO wafer measured with a 532 nm diode laser excitation. According to the existing literatures the peak at 436.5 cm^{-1} can be assigned as the vibrational mode of E_2 and 580.5 cm^{-1} can be assigned as the vibrational mode of E_1 (longitudinal) which are typical ones for ZnO Raman active branches [93, 94, 95]. The E_1 (LO) peak is reported as defect state peak [96]. The presence of this peak was reported by several groups as an indication of oxygen deficiency of ZnO thin films and nanostructures [93, 94, 95].

Gregory J. Exarhos *et. al.* [97] have done annealing study on their ZnO thin films deposited by RF sputtering. They observed that the intensity of the 579 cm^{-1} E_1 (LO) mode was higher compared to the 437 cm^{-1} E_2 mode for their sputtered samples. After a post growth annealing treatment the intensity of the E_1 (LO) peak significantly lowered. Also from the Auger electron spectroscopy of their samples it was found that the ratio of Zinc and Oxygen decreased after post growth annealing treatment in oxygen.

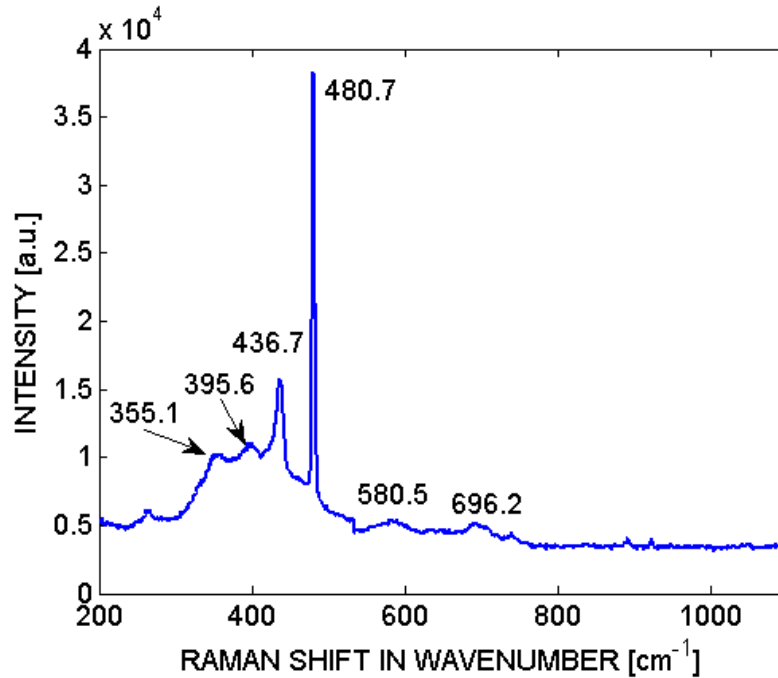


Fig. 7.2.1. Raman spectra of ZnO single crystal wafer

More measurements of Raman spectroscopy can be done with PLD deposited thin film ZnO which can be correlated with the PL measurements to get the complete picture for the defects present in each samples.

TRPL and TIPL studies can be carried out for films deposited by various processes like PLD, ALD, Sol-gel with the optimum excitation parameters achieved from this study.

All these measurements can provide information about different transitions in each sample which can indicate different defects present due to different growth processes. All these study can provide information about an optimum growth method for ZnO samples for specific applications where certain types of defects can improve the device performance or vice versa.

Absolute Photoluminescence measurements can be done for these samples. These can be very useful for identifying different growth process related native defects and TRPL measurements of these samples with required filters for different radiative defects can provide information about their radiative life times.

Ultrafast pump and probe technique measuring the time resolved optical conductivity of ZnO thin films can be developed. The 100 fs Ti:Sapphire laser system with wavelengths of 266 nm, 400 nm and 800 nm can be used. Transmission and reflectance of the probe can be measured before and after the photo excitation of the samples using the pump pulse. These measurements can provide information about the relaxation dynamics of the photo excited carriers.

The long term goal of this project would be achieving a comprehensive understanding of ZnO material properties that will enable us to engineer the material properties for different applications. Using all of these above different growth and characterization technique may help achieve the goal in future.

References

1. E. M. Kaidashev, M. Lorenz, H. von Wenckstern, A. Rahm, H.-C. Semmelhack, K.-H. Han, G. Benndorf, C. Bundesmann, H. Hochmuth, and M. Grundmann, *Applied Physics Letters*, 82, 3901 (2003).
2. B.Guo, Z. Ye, K.S. Wong, *Journal of Crystal Growth*, 253, 252 (2003).
3. D. C. Reynolds, C. W. Litton, and T. C. Collins, *Physical Review Letters*, 140, A1726 (1965).
4. S. D. Sharma and S. C. Kashyap, *Journal of Applied Physics*, 42, 5302 (1971).
5. M. T. Taschuk, Y.W. Sun, Y. Y. Tsui, *Applied Physics. A*, 90, 141 (2008).
6. B. Bayraktaroglu, K. Leedy, and R. Neidhard, *IEEE Electron Device Letter*, 29, 9, 1024 (2008).
7. R. A. Laudise and A. A. Ballman, *Journal of Physical Chemistry*. 64, 688 (1960).
8. P. Onufrijevs, T. Serevicius, P. Scajev, G. Manolis, A. Medvids, L. Chernyak, E. Kuokstis, C.C. Yang and K. Jarasiunas, *Acta Physica Polonica*, A 119, 174 (2011).
9. G. Brauer, W. Anwand, and W. Skorupa, *Physical Review B*, 74, 045208 (2006).
10. A. M. Ma, M. Gupta, F. R. Chowdhury, M. Shen, K. Bothe, K. Shankar, Y. Tsui, and D. W. Barlage, *Solid State Electronics*. 79, 104 (2012).
11. Naveed ul Hassan Alvi, Ph.D Thesis, Linkoping University,2011.
12. S.J.Lim, Soonju Kwon, H.Kim, *Thin solid Films*.516-7,1523 (2008).
13. Zinc Oxide Bulk, Thin Films and Nanostructures by Chennupati Jagadish and Stephen J. Pearton,EI SEVIER.
14. Zinc Oxide materials for electronic and optoelectronic device applications by Cole W. Litton, Donald C. Reynolds Thomas C. Collins, Willy and sons
15. D.G. Thomas, *Journal of Physics and Chemistry of Solids*. *Phys. Chem*, 15, 86 (1960)
16. D.H Zhang, Q. P. Wang, Z.Y. Xue, *Applied Surface Science*, 207, 20 (2003).
17. X. Fa-Qiang, S.Y. Ming,S.C. Shu,X.F.Qian, P.H. Bin, *Chinese Physics Letter*, Vol 18, No 9, (2001).

18. X. W. Sun, B. Ling, J. L. Zhao, S. T. Tan, Y. Yang, Y. Q. Shen, Z. L. Dong, and X. C. Li, *Applied Physics Letter*. 95, 133124 (2009).
19. A. Tsukazaki, T. Onuma, M. Ohtani, T. Makino, M. Sumiya, K. Ohtani, S.F. Chichibu, S. Fuke, Y. Segawa, H. Ohno, H. Koinuma, and M. Kawasaki, *Japanese Journal of Applied Physics*, 44, 2, (20-23) (2005).
20. H. S. Kim, F. Lugo, S. J. Pearton, D. P. Norton, Y. L. Wang, and F. Ren, *Applied Physics Letter*, 92, 112108 (2008).
21. U. Ozgur, Ya. I. Alivov, C. Liu, A. Take, M. A. Reshchikov, S. Dogan, V. Avrutin, S. J. Cho, and H. Morkoc, *Journal of Applied Physics*, 98, 041301 (2005).
22. D. C. Look and B. Claflin, *Physica Status Solidi (B)*, 241, 624 (2004).
23. D.B. Bagnall, Y.F. Chen, Z. Zhu, T. Yao, S. Koyama, M.Y. Shen, T. Goto, *Applied Physics Letter*, 70, 17, 2230 (1997).
24. M.H. Huang, S. Mao, H. Feick, H. Yan, Y. Wu, H. Kind, E. Weber, R. Russo, R. Yang, *Science*, 292,189 (2001).
25. Y. W. Heo, D. P. Norton, and S. J. Pearton, *Journal of Applied Physics*. 98, 073502 (2005).
26. Venkatesan T, Green Steven M, *The industrial physicist*, 2-3,22 (1996)
27. Van de Riet E, Nillesen C.J.CM, Dieleman J: *Journal of Applied Physics letter* 74-3,2008(1993).
28. Craciun V, Elders J, Gardeniers J.G.E., Boyd I.W, *Applied Physics letter*, 65-23,2963(1994).
29. Vick D, Tsui Y.Y, Brett M.J, Fedosejevs R, *Thin Solid Films*, 350-1,49(1999).
30. Tsui Y.Y., Sun Y,W, *Optical Materials*, 29-8 1111 (2007).
31. Foltyn S.R, Muenchausen R.E, Dye R.C, Wu X,D, Luo L,,Cooke D.W, Taber R.C,: *Applied Physics Letter*, 59-11,1374 (1991).
32. H.Sankur, W.J. Gnning, J. DeNatale, J.F.Flintoff, *Journal of Applied Physics* 65,2475(1989).
33. Pulsed Laser Deposition of Thin films by Douglas B. Chrisey and Graham K.Hubler, John Wiley and Sons.inc (1994)
34. Y.Y.Tsui, H.Minami, D.Vick, R. Fedosejevs: *J.Vacuum Science Technol Part A Vacuum Surface Films*, 20-3,744(2002).
35. P.K. Dwivedi, Y.W.Sun, Y.Y. Tsui, D.Tonchev, M.Munzar, K.Koughia, C.J. Haugen, R.G. Decorby, J.N. McMullin, S.O. Kasap: *Applied Surface Science*, 248-1,376 (2005).
36. O'Haire R. J., PhD Thesis, Dublin City University, 2009

37. T. H. Gfroerer, Encyclopedia of Analytical Chemistry (John Wiley & sons Ltd, Chichester 2000).
38. Y. W. Heo, D. P. Norton, and S. J. Pearton: Journal Applied Physics. 98, 073502 (2005).
39. Optical Properties of Solids by Mark Fox: Oxford University Press (2010)
40. S. A. Bukesov and D. Y. Jeon, Applied Physics Letter. 81,2184 (2002).
41. E. Hendry, M. Koeberg, and M. Bonn, Physical Review B 76, 045214 (2007).
42. C.-K. Sun, S.-Z. Sun, K.-H. Lin, K. Y.-J. Zhang, H.-L. Liu, S.-C. Liu, and J.-J. Wu, Applied. Physics Letter. 87,023106 (2005).
43. John Vincent Foreman, Ph.D Thesis, Duke University (2009).
44. Neocera user's manual <http://www.neocera.com/PDF/PLD%20components.pdf>
45. Mini-Course on Plasma Diagnostics, IEEE-ICOPS meeting, Jeju, Korea, June 5, 2003 by Francis F. Chen.
46. R. Popil, R. Fedosejeves, A. A. Offenberger, Review of Scientific Instrument. Ins. 57, 1049 (1986).
47. Springer Handbook of Laser and Optics edited by Frnak Trgaer: Springer, Newyork (2007)
48. M. Gupta, F. R. Chowdhury, D. Barlage, Y. Y. Tsui, Applied. Physics. A, 110, 793 (2013) .
49. B. Toftmann and J. Schou, Physical Review Letters, 84, 17 (2000).
50. K. J. Saji, R. Manoj, R.S. Ajimsha and M. K. Jayaraj, Proceedings of SPIE 6286, 62860D (2006)
51. V. Craciun, S. Amirhaghghi, D. CRaciun, J. Elders, J.G.E Gardenies, Ian W Boyd, Applied Surface Science 86, 99-106 (1996).
52. Rajeswari Yogamalar, Ramasamy Srinivasan, Ajayan Vinu, Katsuhiko Ariga, Arumugam Chandra Bose, Solid State Communications 149, 1919 (2009).
53. J. B. Franklin, B. Zou, P. Petrov, D. W. McComb, M. P. Ryan and M. A. McLachlan, Journal of Material. Chemistry, 21, 8178 (2011).
54. J.I. Langford and A.J.C. Wilson, Journal of Applied Crystal, 11, 102 (1978).
55. A.R. Bushroa, R.G. Rahbari, H.H. Masjuki, M.R. Muhamad, Vacuum 86, 1107 (2012).
56. Wenwen Lin, Dagui Chen, Jiye Zhang, Zhang Lin, Jiakui Huang, Wei Li, Yonghao Wang, and Feng Huang, Crystal Growth and Design, 9, 4378 (2009).
57. L. Avril, Ph. Guaino, F. Maseri, K. Muthukaruppasamy, J.-J. Pireaux: Journal of Physics, Conference Series 417, 012011 (2013).

58. Young Rae Jang, Keon-Ho Yoo and Seung Min Park, *Journal of Material Science and Technol*, 26(11), 973-976 (2010).
59. S. K. Nandi, S. Chakrabarty, M. K. Bera and C. K. Maiti, *Buletin of Materials Science*, 30(3), 247 (2007).
60. T. Voss, C. Bekeny, L. Wischmeier, H. Gafsi, S. Boner, W. Schade, A.C. Mofor, A. Bakin, A. Waag, *Applied Physics Letter*,89,182107 (2006).
61. S. Vempati, J. Mitra, P. Dawson, *Nanoscale Research Letters*, 7, 470 (2012).
62. B. Cao, W. Cai, H. Zeng, *Applied Physics Letter*,88,161101 (2006).
63. S.H. Jeong, B.S. Kim, B. T. Lee, *Applied Physics Letter*, 82,2625 (2003).
64. E.G Bylander, *Journal of Applied Physics*, 49,1188 (1978).
65. H. Zeng, G. Duan, Y. Li, S.Yang, X. Xu, W.Cai, *Advanced Functional Materials*, 20,561(2010).
66. H. He, Y. Wang, J. Wang, Z.Ye, *Physical Chemistry Chemical Physics*, 13,14902, (2011).
67. J.D Ye, S.L Gu, F.Qin, S.M Zhu, S.M. Liu, X. Zhou, W. Liu, L.Q. Hu, R. Zhang, Y.Shi, Y.D. Zheng, *Applied Physics A*,81,759 (2005).
68. B. Lin, Z. Fu, Y. Jia, *Applied Physics Letter*, 79,943 (2001).
69. S.A. Studenikin, N. Golego, M. Cocivera, *Journal of Applied Physics*,84,2287 (1998).
70. P.S Xu, Y.M Sun, C.S Shi, F.Q Xu, H.B Pan; *Nucliar Instrument and Methods in Physics Research B*, 199, 286(2003).
71. D. Li, Y.H Leung, A.B Djurišić, Z. T Liu, M,H Xie, S.L Shi, S.J Xu, W,K Chan, *Applied Physics Letter*, 85,1601 (2004).
72. J. H. Wilkinson: Ph. D thesis, Wake Forest University (2003).
73. D.H Zhang, Q. P. Wang, Z.Y. Xue: *Applied Surface Science*. 207, 20 (2003).
74. W. I. Park, G.-C. Yi: *Journal of. Electronic Material*.30, L32 (2001).
75. T. Matsumoto, H. Kato, K. Miyamoto, M. Sano, E. A. Zhukov, *Applied Physics Letter*, 81, 1231 (2002).
76. B.Guo, Z. Ye, K.S. Wong, *Journal of Crystal Growth* 253, 252 (2003).
77. A. Teke, U. Ozgur, S. Dogan, X. Gu, H. Morkoc, B. Nemeth, J. Nause, H. O. Everitt, *Physical Review B* 70, 195207-1 (2004).
78. Y. Bolkhovityanov, O. Pchelyakov, *Physics_Uspeki*. 51 (5), 437 (2008).
79. B. Ullrich, A. Erlacher, *Journal of Physics. D: Applied Physics*,38 , 4048 (2005).

80. N. I. Aly, A. A. Akl, A. Ibrahim, S. A. Riad, *Egyptian Journal of Solid*, 24 (2), 245(2001).
81. S. Tsuji, and E. Iri, *Japanese Journal of Applied Physics* 25 (11), L896-L898 (1986).
82. M. M. A. J. J. Schermer, A. T. J. Niftrik, G. J. Bauhuis, P. Mulde, P. K. Larsen, , T. P. J. Peters, B. Bruin, A. Klaassen, J. J. Kelly, *Journal of The Electrochemical Society* 151 (5), G347 (2004).
83. R. K. Singh, D. Kumar, *Material Science and Engineering*, R22, 113 (1998).
84. R. N. Sheftali, V. Cherbakov, *Crystal Research and Technology* 16 (8), 887 (1981).
85. V. A. Budyanus, N. Chechuyi, A. Damaskisn, A. Fedoseev, A. A. Nasakins, L. Pyshkinm, M. I. Valkovskaya, V. P. Zenchenko, *Physics Status Solidi (a)* 91, 737 (1985).
86. B. Ullrich, A. Erlacher, S. Yano, R. Schroeder, , T. G. Gerasimov, H. J. Haugan, *Proceedings of SPIE* 4977, 180 (2003).
87. A. Erlacher, M. Ambrico, V. Capozzi, V. Augelli, H. Jaeger, B. Ullrich, *Semiconductor Science and Technology* 19 (2004).
88. B. Ullrich, A. Erlacher, H. Jaeger, *Proceedings of SPIE*, 5359, 23 (2004).
89. B. Ullrich, A. Erlacher, H. Jaeger, *Proceedings of SPIE*, 5339, 365-373, (2004).
90. M. Gupta, F. R. Chowdhury, V. Sauer, S. S. Yap, T. W. Reenaas, Y. Y. Tsui, *Proceedings of SPIE*, 80070J, (2011).
91. R. R. Campomanes, J. Ugucione, J. H. Dias da Silva, *Journal of Non-Crystalline Solids* 304, 259 (2002).
92. F. A. Abdel-Wahab, M. F. Kotkata, *Physica B: Condensed Matter* 368, 209–214 (2005).
93. T. C. Damen, S. P. S. Pqrtq, B. Tell, *Physical Review*. 142 (2), 570 (1966).
94. X. Wang, Q. Li, Z. Liu, J. Zhang, Z. Liu : *Applied Physics Letter*. 84, 4941 (2004).
95. X. L. Xu, S. P. Lau, J. S. Chen, G. Y. Che, and B. K. Tay, *Journal of Crystal Growth*, 223, 201 (2001).
96. X. L. Xu, S. P. Lau, J. S. Chen, G. Y. Che, and B. K. Tay, *Journal of Crystal Growth*, 223, 201 (2001).
97. G. J. Exarhos, S. K. Sharma, *Thin Solid Films* 270, 27 (1995).
98. T. Ho, M. Gupta, F. R. Chowdhury, Z. Chen, Y. Y. Tsui, *Applied Physics B*, 113-3, 429 (2013).
99. T. W. Reenaas, Y. S. Lee, F. R. Chowdhury, M. Gupta, Y. Y. Tsui, T. Y. Tou, S. L. Yap, S. Y. Kok, S. S. Yap, *Applied Surface Science*, 354(A), 206 (2015).

Appendix A

Photoluminescence data processing

The original Photoluminescence data might have some contribution from the ambient light. To get rid of these effects the following steps were taken.

- First measurements were taken using the sample of interest. Most of the cases we measured ZnO thin film samples on SiO₂ /Si substrates. In Fig. A1 a sample data of PL measurement for ZnO PLD thin film (250 °C) on SiO₂/Si substrate is shown. This is the measurement with ambient light effects. In this case ns ND:YAG laser was used to excite the PL emission from the samples and PL signal was integrated for 10 seconds which is an accumulation of 200 shots.

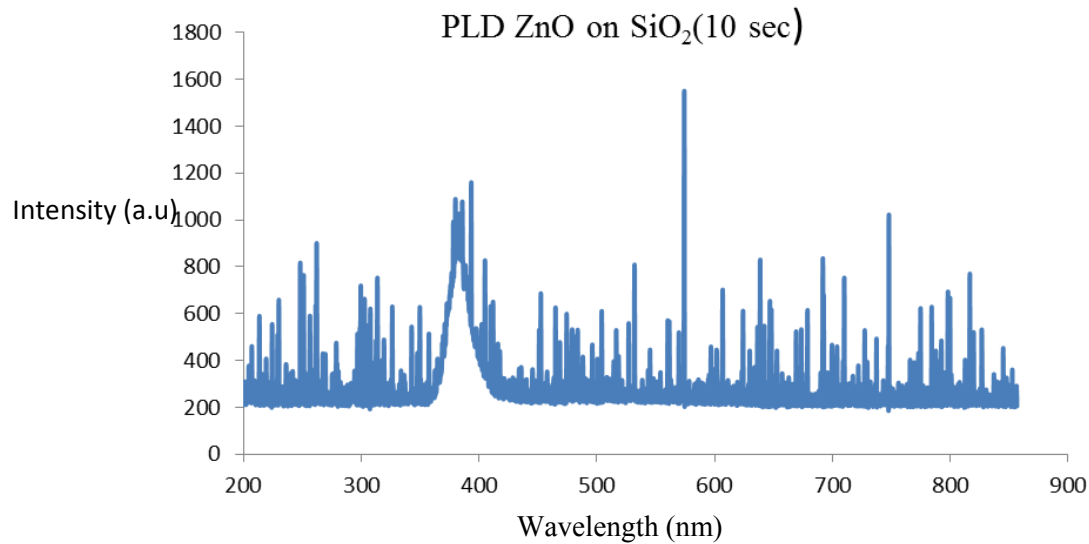


Fig. A1. Photoluminescence spectrum of ZnO thin film on SiO₂/Si substrate before background subtraction.

- The room light contribution should be considered for long integration times like 10 seconds. During the measurements all the main room lights were turned off to make the PL signal less contaminated but still there were some ambient lights which can have significant contribution especially when the PL signal is coming from a thin film with 50 nm thickness. A measurement were taken for 10 sec without the excitation laser so that there will be only room light detected by the spectrometer.

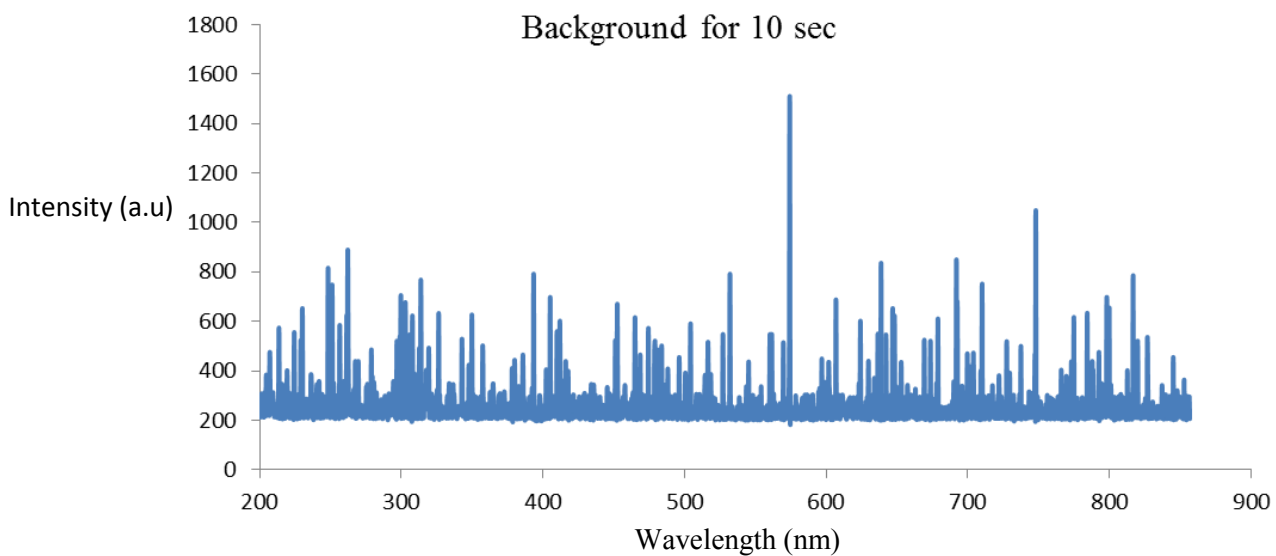


Fig. A2. Back ground light contribution for 10 second integration time.

Fig. A2 is showing the room light contribution accumulated for 10 second integration time using the same ocean optics spectrometer.

- After subtracting the background from the real measurement the true contribution from the thin film PL become more clearly visible. Figure A3 is showing the Photoluminescence spectrum of ZnO thin film deposited on SiO₂/Si substrate after background subtraction.

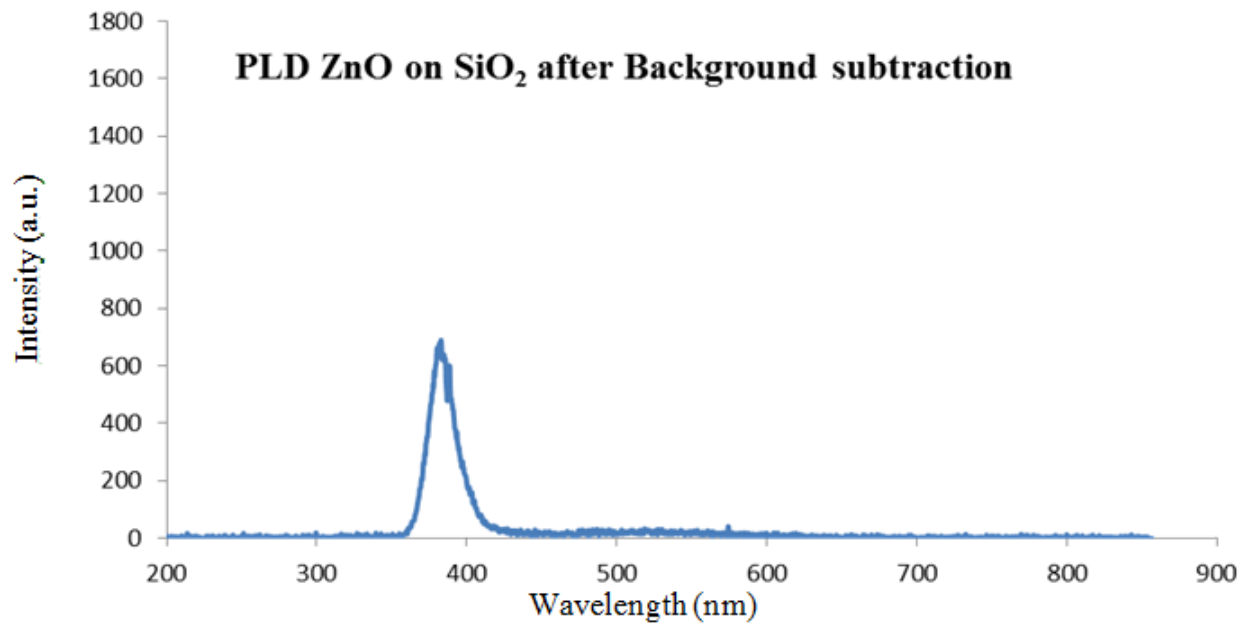


Fig. A3. Time integrated PL emission from ZnO thin film deposited by PLD after background subtraction

Appendix B

Error calculation for measured PL data

In order to calculate the errors of the Photoluminescence measurements six set of data were used to calculate the slandered deviation and standard errors measured using the Single crystal ZnO wafer manufactured by MTI.

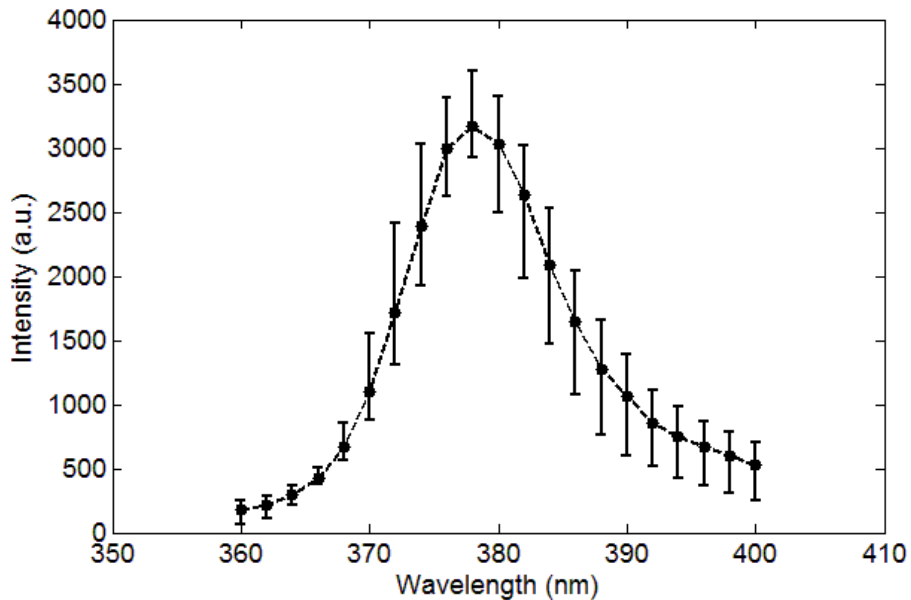


Fig. B1. UV Photoluminescence from ZnO single crystal wafer with ns excitation

Fig. B1 is showing the UV emission peak of the PL measured from the Single crystal ZnO wafer. Each data point is an average and standard deviation of six data points. Using these data sets standard deviation and standard error were calculated for the peak position intensity. The values are given in table B1.

Table B1. Error calculation for PL measurements of ZnO

Sample	Peak position(nm)	Average Intensity(AU)	Standard deviation	Standard error
ZnO wafer	378.23	3378.213	228.4403	72.23917

Appendix C

Carrier life time calculation from time resolved PL measurement

The time resolved PL measurements of ZnO single crystal showed bi-exponential decay behaviour. Using the normalized intensity plot best fit for the fast and slow decay components were measured.

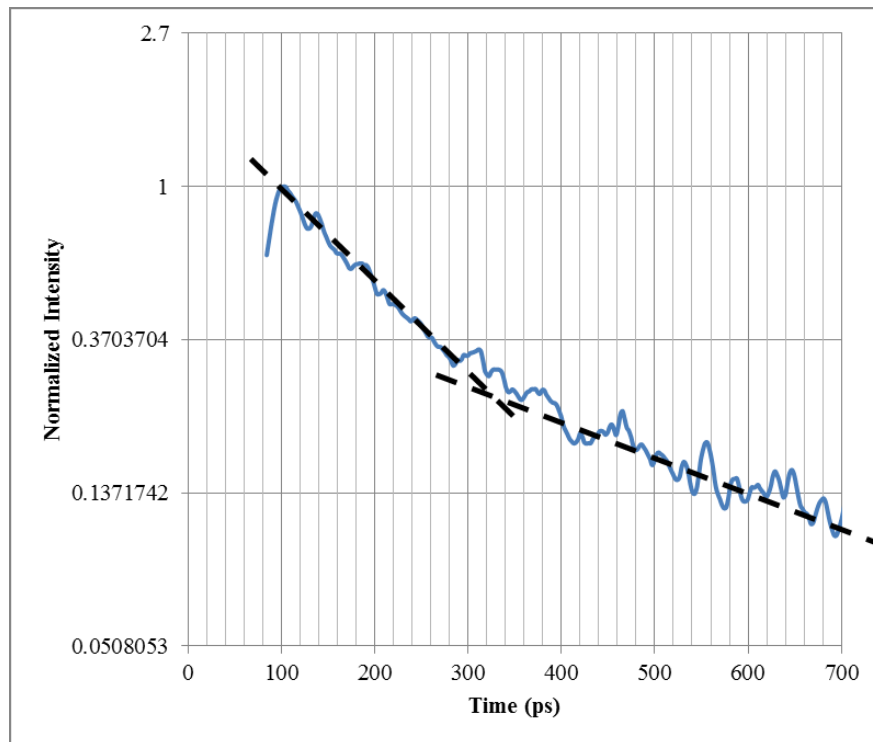


Fig. C1. Time resolved PL measurement of ZnO for carrier life time estimation

Fig. C1 is a sample graph where the best fit for fast and slow components are 160 ps and 350ps.

Appendix D

Additional Materials Deposited Using PLD during This Work

The versatility of PLD is one of its unique features. During the work period of this thesis, several other materials beside ZnO were deposited using PLD. These works are not part of this thesis. However, a brief summary of these material depositions are summarized below.

(i) Fabrication of free standing DLC thin Films for high energy laser target application

PLD is well known for fabricating diamond like carbon (DLC) thin films. Both dense and porous DLC thin films were deposited previously by our group [29]. Later we deposited ultra-thin free standing DLC thin films to be used as a target for high intensity laser applications [98]. These free standing DLC thin films were deposited on soap covered Sodium substrates using a carbon tape as a target. The PLD set up used for these depositions are described in Chapter 3. The laser fluence was varied between $8.5\text{-}14\text{ J}\cdot\text{cm}^{-2}$ and the target to substrate distance was kept at 10 cm. 20 -200 nm thick films were then released to get the free standing targets of up to 1 inch square area.

A dummy film was deposited on Si with all the free standing DLC growths to perform some characterizations like thickness measurements and roughness comparisons. A 100 nm thick free standing film was used to investigate the film properties using AFM, XPS and nano indentations. The free standing film had a surface roughness of about 9 nm when released where as DLC on Si had a surface roughness of around 0.5 nm. Damage threshold properties of the DLC foils were studied using a Nd:YAG Laser (1064 nm, 6ns) and $7\times 10^{10}\text{ W}/\text{cm}^2$ peak intensity was obtained for our best ultra-thin film. All these characterization part was done by another graduate student Timothy Ho of our research group. These results are reported in [98].

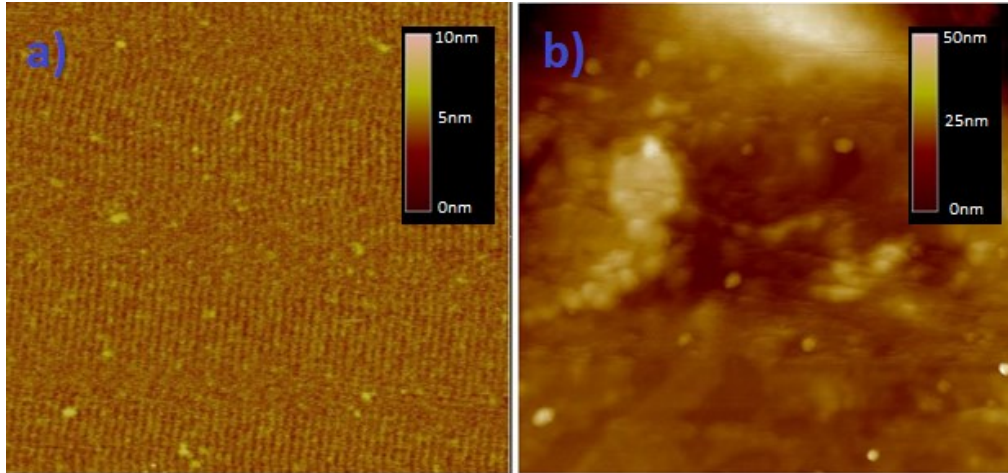


Fig. D1. AFM image of $2 \times 2 \mu\text{m}$ area of the DLC film deposited on (a) Si substrate with an rms roughness of 0.6 nm (b) DLC film grown on soap film (rms roughness 8-12 nm) and lifted-off on to a metal plate demonstrating an rms roughness of 9 nm [98].

Fig.D1 is showing the AFM images of DLC thin films deposited on (a)Si Substrate and (b) Soap film and lifted off on a metal plate. The rms roughness of the Si substrate film was measured using AFM was 0 nm and the free standing film on a metal plate was measured 9 nm.

(ii) Nano second (ns) and femtosecond (fs) PLD of Si nanodots

PLD is widely used to fabricate nano dots and nanostructures [32, 33]. Generally, ns lasers are used in PLD but fs lasers are also used and recent researches are showing that fs laser generated plasma plume has different contribution in film properties [99].

Si nano-dots were deposited using both KrF (ns) laser and Ti:Sapphire (fs) laser on GaAs substrates. Ablation threshold for the deposition methods were investigated using a Langmuir probe which was placed in the substrate position. The same experimental setup described in chapter 3 was used for the ns growths. For fs growths, a Ti:Sapphire laser (150 fs, 1 kHz) was used instead of the KrF laser (25 ns, 12 Hz). Laser fluence was varied from 3 - 32 J/cm² for KrF laser and most of the growths were done at 1 - 2.75 J/cm² for the Ti:Sapphire laser. The Langmuir probe was biased at -40 V to repel the electrons and to attract the ions from the laser produced plasma.

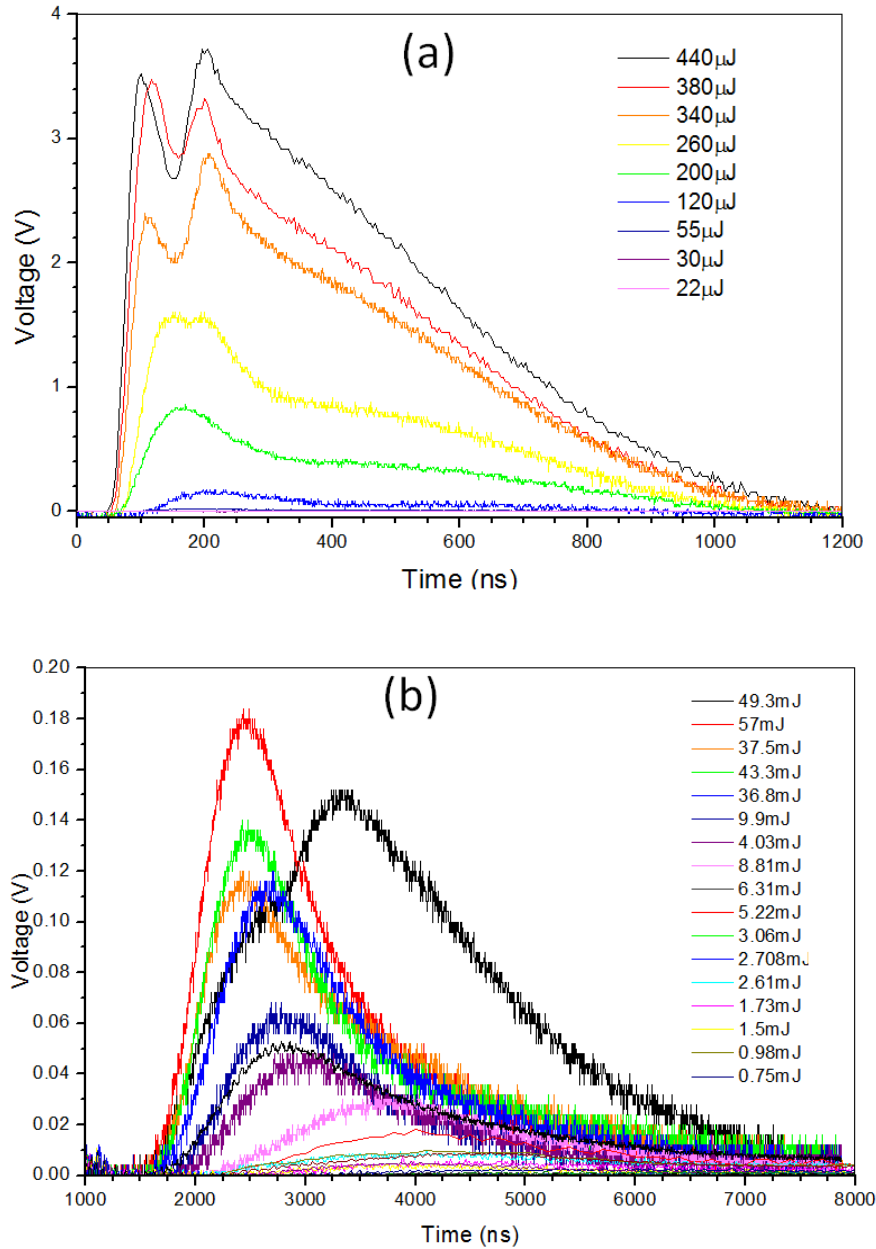


Fig. D2. Plot for ion current versus time for the (a) fs Ti:Sapphire laser and (b) ns KrF laser, to determine the ablation threshold for poly-Si target, measured at several different laser energies [99].

Fig. D2 shows the Ion signals generated by fs and ns lasers. Fs laser generated ions are faster than ns laser generated ions because of the higher intensity of fs laser. It is assumed that the ablation threshold and this ion generation threshold is almost the same.

In the case of ns growths, at high laser fluence (32 J.cm^{-2}) lots of small nanodots (ranging from 80 nm onwards) were observed. These nanodots were accompanied with large micron size debris which is a signature disadvantage of PLD. A fluence close to the ablation threshold resulted in a thin film growth with several debris. SEM images of ns grown Si nanodots at 32 J.cm^{-2} fluence are shown in Fig. D3.

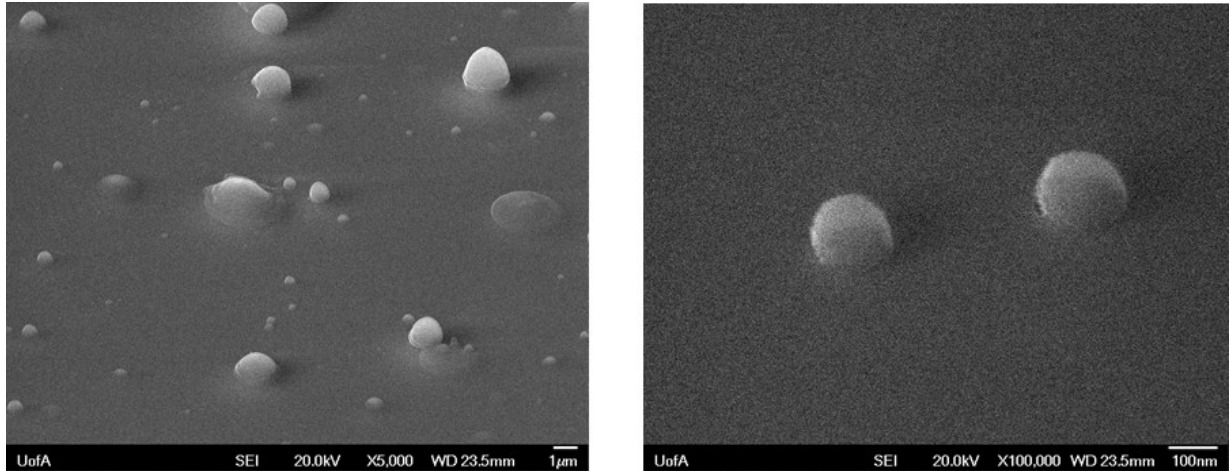


Fig. D3. SEM of Si nanodots on GaAs substrate using the ns KrF laser at 5000x showing a large size distribution from 100 nm to $3\mu\text{m}$ droplets and 100000x magnification showing two 100 nm nano dots grown by PLD at 32 J.cm^{-2} fluence [100].

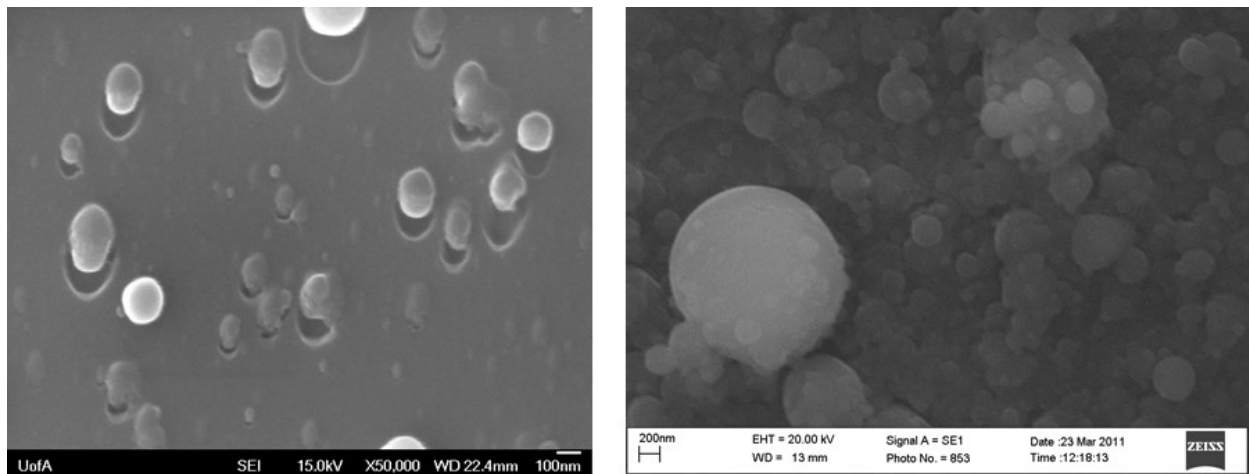


Fig. D4. SEM image of Si Nano dots grown on GaAs substrate using the fs Ti:Sapphire for PLD at 1.5 J.cm^{-2} fluence. Fast growth rate with lots of cluster formations were observed [100].

Several growths were conducted using fs Ti:Sapphire laser. Fig. D4 shows the SEM images of Si Nano dots grown by fs laser PLD. A thick film of nanoparticles ranging from 20 nm to micron size droplets were observed in case of fs deposition. At a lower fluence which was close to the ablation threshold the number of large clusters was reduced but also the Nano dots were very fewer in number.

A mask created by E-beam lithography which contained the array of 100 nm diameter holes with 300 nm spacing were used to fabricate uniform array of Nano dots with few defects. Only ns KrF laser was used to study this mask technique.

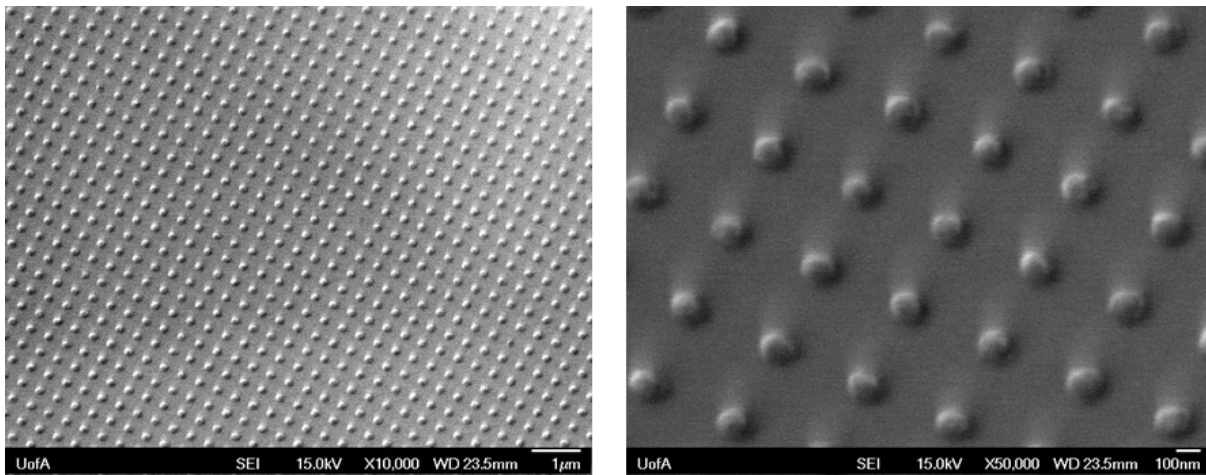


Fig. D5. SEM of patterned Si nanodots at 10,000x and 50,000x magnification on GaAs substrate using EBL mask using ns KrF laser at 5 J.cm^{-2} [100].

It was observed that fluence closer to the ablation threshold was more appropriate for growing Nano dots with this technique. Fig. D5 shows the SEM images of Si nanodots obtained using this mask technique. This part of the study was primarily done by Prof. Manisha Gupta and another graduate student Vincent Saur. More details of the results obtained from the above study were reported in [90].

Several growths of Germanium were also performed with both ns and fs lasers with the same experimental conditions. The ablation threshold study was done for this material as well. Raman study of both Si and Ge samples revealed the fact that fs PLD samples were crystalline in nature which is completely different than the amorphous ns PLD grown samples. These works were

jointly done with Collaborators from NTNU (Trondheim, Norway) and detailed results are published in [99].

Appendix E

Photo generated carrier density calculation for different excitation source

Using equation (2.1.1) from chapter 2 all the Photo generated carrier densities were calculated for three sources.

$$N = \frac{I\alpha\tau}{hv} \dots\dots\dots(2.1.1)$$

Here,

Absorption co-efficient of ZnO at UV (266 to 325nm) $\alpha = 2 \times 10^5 \text{ cm}^{-1}$

T= 100fs for single crystal wafer from the time resolved measurement.

(i) CW He-Cd (325 nm) Laser generated carrier density

Average power of He-Cd Laser =15mW

Beam diameter= 2 mm

$$Intensity = \frac{Power}{Area}$$

$$=0.477\text{W/cm}^2$$

Therefore, using (2.1.1) the absorbed photon density or photo generated carrier density

$$=1.4416 \times 10^{13} /\text{cm}^3$$

(ii) ns (266 nm) Laser generated carrier density

Energy of each pulse=0.1 mJ

Area of the beam spot=0.15 cm²

Pulse duration= 6ns

$$\begin{aligned} \text{Peak Intensity} &= \frac{\text{Energy}}{\text{Pulse duration} * \text{Area}} \\ &= 0.11 \times 10^6 \text{ W/cm}^2 \end{aligned}$$

Using equation (2.1.1) the carrier density = $2.95 \times 10^{18} \text{ cm}^{-3}$

(iii) fs (266 nm) Laser generated carrier density

As the pulse duration is 180 fs which is smaller than any kind of recombination the τ of equation 2.1.1 is replaced by 180 fs for this part of calculation [43]

Pulse energy=4 μ Jule

Beam spot radius=1 mm

Using (2.1.1) the carrier density is = $1.36 \times 10^{23} \text{ cm}^{-3}$